NASA Contractor Report 4532

Navier–Stokes Flowfield Computation of Wing/Rotor Interaction for a Tilt Rotor Aircraft in Hover

Ian G. Fejtek

CONTRACT NCC2-55
July 1993

National Aeronautics and Space Administration

NASA Contractor Report 4532

Navier–Stokes Flowfield Computation of Wing/Rotor Interaction for a Tilt Rotor Aircraft in Hover

Ian G. Fejtek

Stanford University
Department of Aeronautics and Astronautics
Stanford, CA 94305

Prepared for
Ames Research Center
CONTRACT NCC2-55
July 1993

National Aeronautics and
Space Administration

Ames Research Center
Moffett Field, California 94035-1000

Contents

Abstract

The download on the wing produced by the rotor-induced downwash of a tilt rotor aircraft in hover is of major concern because of its severe impact on payload-carrying capability. A method has been developed to help gain a better understanding of the fundamental fluid dynamics that causes this download, and to help find ways to reduce it. In particular, the method is employed in this work to analyze the effect of a tangential leading edge circulation-control jet on download reduction. Because of the complexities associated with modeling the complete configuration, this work focuses specifically on the wing/rotor interaction of a tilt rotor aircraft in hover. The three-dimensional, unsteady, thin-layer compressible Navier-Stokes equations are solved using a time-accurate, implicit, finite difference scheme that employs LU-ADI factorization. The rotor is modeled as an actuator disk which imparts both a radial and an azimuthal distribution of pressure rise and swirl to the flowfield. A momentum theory/blade element analysis of the rotor is incorporated into the Navier-Stokes solution method. Solution blanking at interior points of the mesh has been shown here to be an effective technique in introducing the effects of the rotor and tangential leading edge jet. Results are presented both for a rotor alone and for wing/rotor interaction. The overall mean characteristics of the rotor flowfield are computed including the flow acceleration through the rotor disk, the axial and swirl velocities in the rotor downwash, and the slipstream contraction. Many of the complex tilt rotor flow features are captured including the highly three-dimensional flow over the wing, the recirculation fountain at the plane of symmetry, wing leading and trailing edge separation, and the large region of separated flow beneath the wing. Mean wing

surface pressures compare fairly well with available experimental data, but the time-averaged download/thrust ratio is twenty to thirty percent higher than the measured value. This discrepancy is due to a combination of factors that are discussed. Leading edge tangential blowing, of constant strength along the wing span, is shown to be effective in reducing download. The jet serves primarily to reduce the pressure on the wing upper surface. The computation clearly shows that, because of the three-dimensionality of the flowfield, optimum blowing would involve a spanwise variation in blowing strength.

List of Figures

List of Symbols

a	speed of sound
A	flux Jacobian matrix in the ξ-direction; rotor disk area
b	wing span; distance normal to surface where $V = V_{max}/2$ in a wall jet
B	flux Jacobian matrix in the η-direction; number of rotor blades
c	wing chord; local rotor blade chord
c_p	specific heat at constant pressure
C	flux Jacobian matrix in the ζ-direction
C_d	2-D drag coefficient
C_l	2-D lift coefficient
C_T	rotor thrust coefficient
C_μ	blowing momentum coefficient
D	drag on rotor blade segment
D_E, D_I	explicit and implicit artificial dissipation terms, respectively
D_A, D_B, D_C	diagonal matrices associated with the LU-ADI algorithm
DL	download force
e	total energy per unit volume
e_i	internal energy per unit mass
$\hat{E}$	inviscid flux vector in the ξ-direction
$\hat{F}$	inviscid flux vector in the η-direction
$\hat{G}$	inviscid flux vector in the ζ-direction
$\hat{G}_v$	viscous flux vector in the ζ-direction
h	time step size; height of tangential jet exit
i_b	integer equal to one or zero used for blanking the implicit solution

	at selected grid points
I	identity matrix
J	transformation Jacobian
k	coefficient of thermal conductivity
K_E, K_I	user-specified input constants for explicit and implicit artificial dissipation
l	turbulent mixing length scale
L	lift on rotor blade segment
L_A, L_B, L_C	lower bidiagonal matrices associated with the LU-ADI algorithm
M	viscous flux Jacobian matrix in the ζ-direction; Mach number
M_∞	freestream Mach number
n	normal direction coordinate
p	pressure
P, Q	source terms of the Poisson equations defined to provide elliptic grid control
Pr	Prandtl number
Q	rotor torque
$\hat{Q}$	vector of conserved quantities
r	rotor radial location
R	rotor radius; radius of curvature; gas constant
Re	Reynolds number
t	time
T	rotor thrust; temperature
T_ξ, T_η, T_ζ	similarity transformation matrices
u, v, w	Cartesian velocity components
U_A, U_B, U_C	upper bidiagonal matrices associated with the LU-ADI algorithm
U, V, W	contravariant velocity components
V	velocity
V_a	local velocity normal to rotor disk
V_{eff}	effective local velocity in plane normal to rotor radius
V_h	ideal induced velocity at the rotor disk in hover $\left(= \Omega R\sqrt{C_T/2}\right)$
V_{max}	maximum magnitude of velocity in wall jet

V_t	local rotor swirl velocity
x, y, z	Cartesian coordinates
α	local angle of incidence
α_i	local induced angle of incidence
β	rotor blade pitch angle
γ	ratio of specific heats
$\delta_\xi, \delta_\eta, \delta_\zeta$	central difference operators
$\Delta_\xi, \Delta_\eta, \Delta_\zeta$	forward difference operators
$\nabla_\xi, \nabla_\eta, \nabla_\zeta$	backward difference operators
ϵ	artificial dissipation coefficient
θ	local rotor blade twist angle relative to the twist at the 75% rotor blade span location
λ	coefficient of bulk viscosity
Λ_A	diagonal matrix of eigenvalues associated with the flux Jacobian matrix A
Λ_B	diagonal matrix of eigenvalues associated with the flux Jacobian matrix B
Λ_C	diagonal matrix of eigenvalues associated with the flux Jacobian matrix C
μ	coefficient of viscosity
ξ, η, ζ	chordwise, spanwise, and normal coordinates in body-conforming system
ρ	density
σ	spectral radius of flux Jacobian matrix
τ	time coordinate in computational domain; viscous stress
ϕ	local angle between freestream velocity and relative rotational velocity (=0 in hover)
Φ	matrix of flux limiters for artificial dissipation model
ψ	azimuthal angular coordinate of rotor
ω	vorticity
Ω	angular frequency of rotor rotation

Chapter 1

Introduction

1.1 Motivation

The tilt rotor aircraft is a unique flight vehicle which combines the vertical takeoff and landing capability of the helicopter with the efficient high-speed cruise performance of conventional fixed-wing aircraft. This is achieved by positioning, at both wing tips of a fixed wing, a rotor which can be tilted so as to provide lift for hover and thrust for cruise flight.

The concept was first proposed by Bell Helicopter engineers during World War II, and it evolved into a first prototype in 1955, designated the XV-3 [1]. In 1977, the NASA/Army/Bell XV-15, a 13,000 lb experimental tilt rotor aircraft, flew for the first time in a research program that continues today. The usefulness of the tilt rotor aircraft is evidenced in the recent development of the V-22 Osprey for the U.S. Armed Forces by a Bell Helicopter Textron/Boeing Helicopters team. The V-22 is a multi-service, multi-mission tilt rotor aircraft. It has a vertical take-off weight of 55,000 lb and is capable of transporting up to 40 passengers.

The tilt rotor vehicle with its unique features can also be exploited as a civil transport in the city-center to city-center commuter market or as a feeder to hub airports. The need for such a mode of transport will certainly increase as community real estate prices continue to increase, making new airport construction prohibitively expensive, driving new airport locations further away from large population densities.

The tilt rotor (in this report, "tilt rotor" refers to the entire configuration, i.e. the airframe and the rotors, not just the rotors) offers several considerable advantages over the rival tilt wing concept (in which the rotors and wing both rotate in the transition from helicopter to airplane mode and back). Wing tilt requires additional mechanical complexity resulting in increased structural weight to support the higher concentrated wing/fuselage junction loads. Also, due to the large exposed frontal wing area in hover, the tilt wing, in vertical flight in gusty wind or cross-wind conditions, is much more susceptible to controllability problems than the tilt rotor.

A major limitation of the current tilt rotor configuration, however, is the aerodynamic download imposed on the wing by the rotor flowfield when hovering. Because the wing is fixed, the rotor flow, in hover, hits the wing near 90 degrees. The download force on the wing has been measured and can be as large as 10 – 15 percent of the total rotor thrust [2,3]. Assuming the payload-carrying capability to be about 25% of gross take-off weight, complete elimination of the download could increase the effective payload by over 50%. The need for a thorough understanding, and the eventual reduction, of wing download, then, is the major impetus driving this theoretical study on tilt rotor flowfields.

The flowfield about a tilt rotor configuration is very complex. The rotor, typically located about one wing chord above the tilt rotor wing, induces a flow which is closely coupled to the flow about the wing. The rotor flowfield itself is very complicated. The rotor imparts not only a vertical downwash to the flowfield, but also, due to the rotational motion of the rotor, a velocity tangential to the circumferential direction called the swirl velocity. The outer portions of the rotor blades see a transonic flow which may, at very high tip speeds, even yield upper surface shocks and shock-induced boundary layer separation. A spiraling wake vortex sheet is shed from each blade. Regions of concentrated vorticity (tip vortices) which trail from the blade tips, also propagate in a helical motion in the rotor wake interacting with the following blades and also with the wing. On the tilt rotor wing upper surface there exists a large region of nearly-stagnated flow. The flow is highly three-dimensional with essentially a two-dimensional chordwise flow near the wing tip which becomes primarily spanwise further inboard along the wing. Due to symmetry of the hovering tilt rotor flowfield,

the spanwise flow from both wings meets at the vehicle centerline and is redirected upwards. Some of this rising column of air is re-ingested by the rotor thus creating a large-scale recirculation pattern which reduces rotor performance. This flow pattern has been termed the "fountain effect". Beneath the wing is a large region of unsteady, turbulent, separated flow. Refer to Fig. 1 taken from Ref. [3] for simplified sketches of the main flow features about a V-22 in hover.

As stated previously, the primary motivation for this work is to gain a better understanding of the tilt rotor flowfield in hover with the hope that this would lead to ways of reducing the download in future designs. The wing and the rotor and their close proximity to each other is the principal contributor to wing download. The effects of the fuselage, tail, and nacelle of the tilt rotor aircraft on download, although perhaps not unimportant, are secondary. It is desired, in this study, to analyze the principal features of the tilt rotor flowfield by solving the Navier-Stokes equations. This allows the modeling of the physics of the flowfield far more accurately than hitherto attempted. The state of the art, at this time, in the numerical solution of these equations does not permit the simultaneous computation of the complete tilt rotor aircraft. This current study, therefore, focuses on the Navier-Stokes solution of wing/rotor interaction for a tilt rotor aircraft in hover.

1.2 Previous Work

1.2.1 Experimental Work

Flight test of the XV-15 [1,4] has yielded quantitative estimates of hover performance including the effect of flap deflection on download. Figure 2 taken from Ref. [1] shows the download (DL) normalized by the rotor thrust (T) plotted as a function of flap angle. These measurements were taken at a sufficient height above the ground so as to eliminate ground effect. The ratio DL/T is reduced from over 16% at zero flap deflection to about 9% when the flaps are deflected to 67°. With increasing flap deflection, the download is reduced, due not only to the reduction of wing area affected by the rotor downwash, but also to the reduction of vertical drag coefficient.

Superimposed on the same figure is a data point from a NASA outdoor test [9] of a 0.658-scale model of the V-22 rotor and wing. (This test is discussed further below).

To study the tilt rotor flowfield, the flexibility and control offered by wind tunnel testing has been found to be very helpful. McCroskey et al. [5] measured the drag of two-dimensional wind tunnel models of the XV-15 airfoil (a modified NACA 64A223) with various flap and leading edge configurations. They found that the drag on the airfoil in a freestream flow at -90 degrees was very sensitive to not only flap angle but also the surface curvature distribution on the upper surface near the leading edge. Increasing the flap angle reduces the frontal area thereby reducing the download. The shape of the airfoil and flap also affect the vertical drag. A flat plate has a 2-D drag coefficient about twice that of a circular cylinder. Increasing airfoil thickness and camber, then, which tend to make the airfoil less like a flat plate and more like a circular cylinder or ellipse, contribute to download reduction. Further discussions on the effects of wing geometry on download can be found in a review of tilt rotor download research by Felker [6].

Maisel et al. [7] continued this 2-D experimental effort on the XV-15 airfoil by examining the effects of several different flap and leading edge configurations on the download. They found that reduction of "frontal" area resulting from flap deflection accounted for less than half of the total download reduction. It was observed that modification of the contours of the leading edge and of the flap had a significant impact on download reduction by delaying flow separation. Increasing the curvature on the flap upper surface and introducing a slat in front of the leading edge both aided in reducing the download.

Also, it was found that the measured download was sensitive to variations in angle of attack away from -90°. This demonstrates the need to include the effect of swirl imparted by the rotor in any attempt to accurately predict the download on an actual three-dimensional tilt rotor configuration. Reference [7] also notes that the download is fairly insensitive to the Reynolds number, at least in the range tested — from 0.6×10^6 to 1.4×10^6. This indicates that uncertainties arising from the definition of the Reynolds number appropriate for the wing/rotor configuration in hover should not affect the results.

Boeing has tested a powered tilt rotor model whose basic geometry was that of a 0.15-scale V-22 Osprey. Some results of this test are reported in Ref. [8]. Flow visualization verified the existence of chordwise flow on the wing upper surface near the wing tip and spanwise flow further inboard. The recirculation pattern at the plane of symmetry was observed, and due to re-ingestion of the fountain flow into the rotors, a loss in rotor thrust at a given power setting was measured. The 0.15-scale model test also served to evaluate the effect of changing the direction of rotor rotation on airframe download. Regardless of rotation direction, download decreased with increasing flap deflection. With the normal sense of rotation, i.e. the rotor blade passage above the wing is from leading edge to trailing edge, minimum download occurred at a flap deflection of about 75 – 80 degrees and, thereafter, began to increase. This was due to flow separation from the flap upper surface. With rotor rotation in the opposite direction (trailing-to-leading edge), the download was lower at the low flap settings and decreased continuously as the flaps were extended to beyond 90 degrees, reaching the same minimum value as observed for the normal rotation direction. This difference in behavior is due to the swirl in the rotor flowfield, and, in particular, the angle at which the flow impinges on the wing. These experimental observations reinforce the need to model the rotor swirl, if an accurate prediction of download is to be obtained.

Several experimental tests of a rotor alone in hover and of wing/rotor interaction have been undertaken at NASA Ames Research Center. Results from large-scale tests of a 0.658-scale V-22 rotor and wing conducted at the Outdoor Aerodynamic Research Facility (OARF) at NASA Ames are reported in Refs. [2,3,9]. A similar test of the 0.658-scale V-22 wing and rotor was undertaken in the 40- by 80-Foot Wind Tunnel at Ames; results are reported in Refs. [10,11]. The rotor blade planform differed slightly from that in the OARF test to reflect the evolving changes in the V-22 design. These tests provided measurements of rotor performance, wing surface pressures, and wing download. The OARF test measured the performance of the rotor alone. Rotor wake surveys showed the changes in the radial distribution of downwash velocity for different rotor thrust coefficients. Higher thrust levels yielded greater downwash velocities in the outer region of the wake than in the inboard portion of the wake. At lower thrust coefficients, the effect was reversed — the outer portions

of the wake had lower downwash velocities than the inboard region. The maximum value of the rotor figure of merit for the isolated rotor was found to be 0.808. This was reduced to 0.793 for the rotor in the presence of the wing, due to the region of recirculating flow at the plane of symmetry. Flow visualization at the OARF of the wing/rotor flowfield provided insight into the fountain flow and also clearly demonstrated the transition of chordwise flow on the wing upper surface near the wing tip to spanwise flow on the inboard portion of the wing. Both tests measured the small reductions in the download/thrust ratio that were due to increasing rotor thrust coefficient. Felker and Light [2] explained this effect as being due to the variations in the radial distributions of velocity (or dynamic pressure) in the wake due to changes in thrust coefficient. The inboard portion of the rotor wake contributes mainly to the chordwise flow over the wing upper surface, and the outboard portion of the wake contributes mainly to the spanwise flow. The local download on the wing is greater in regions of chordwise flow than in regions of spanwise flow. Changes in downwash distribution with rotor thrust coefficient C_T, therefore, affect the relative contributions of chordwise and spanwise flows to the total download. As the rotor thrust coefficient increases, the dynamic pressure in the outboard portion of the wake (near the wing root) increases, and consequently, the rotor dynamic pressure distribution contributes more to the spanwise flow and relatively less to the chordwise flow, resulting in a reduced download-to-thrust ratio.

In Ref. [2], Felker and Light describe their results from a 0.16-scale model test of the Sikorsky S-76 rotor with two different wings — (i) a conventional wing and a 25% plain flap, and (ii) a circulation control wing possessing slots near the leading and trailing edges for boundary layer control using tangential blowing. As in the test reported in Ref. [7], it was found that the download reduction due to increasing flap deflection was due to a combination of planform area reduction and the reduction of drag coefficient due to the changing geometry.

Beneath the wing of a tilt rotor configuration in hover, there exists a large region of separated flow typical of bluff bodies, as previously described. Because the static pressure in the separated flow region is generally somewhat less than freestream ambient pressure, a suction force on the wing lower surface contributes to the total

download. By energizing the boundary layer using tangential blowing near the leading edge (where the flow is close to separating), it should be possible to move the separation location further around the leading edge on the lower surface, by exploiting the Coanda effect. This should reduce the chordwise extent of the separated flow region below the wing and increase the lower surface pressure, thereby contributing to download reduction.

In tests by Felker and Light [2] using the 0.16-scale circulation control wing, however, it was found that most of the download reduction due to blowing was a result not of movement of the separation location and increase of base (wing lower surface) pressure, but of the decrease in pressure on the wing upper surface. The measured increase in pressure on the lower surface (that is expected with movement of the separation location towards the mid-chord) contributed only about 1/3 to the total download reduction. It was also observed that the reduction in pressure on the wing upper surface near the leading edge extended well aft of the location of the blowing slot. The blowing jet, then, entrained part of the rotor downwash, reducing the extent of near-stagnated flow on the wing upper surface, thereby contributing significantly to the download reduction. Figure 3, taken from Ref. [2], shows typical wing surface pressure distributions on the circulation control wing with and without blowing. The blowing slots were located at 3 percent and 97 percent of wing chord on the upper surface, the former blowing towards the leading edge, the latter towards the trailing edge. Figure 4, also taken from Ref. [2], shows the measured reduction in download/thrust ratio (DL/T) for a range of total pressures of the blowing slot supply plenum (used to control blowing jet velocity). The download/thrust was reduced by as much as 26% with blowing at both slots. It was found that blowing at the leading edge was particularly effective in reducing the download, contributing about 65 percent to this total reduction due to blowing. As the plenum pressure was increased beyond its optimum value, the download/thrust began to increase due to the jet extending further along the airfoil surface, increasing negative pressures on the lower surface aft of the leading edge.

1.2.2 Theoretical Work

The discussion below focuses on the theoretical modeling of: (i) a wing/rotor, and (ii) a rotor alone.

Wing/Rotor Modeling

Previous theoretical studies of airfoil and wing download in hover have either solved simpler fluid dynamic equations than in the current study or restricted the analysis to two dimensions.

Clark and McVeigh in Ref. [12] and Clark in Ref. [13] describe the application of a three-dimensional low-order panel method to a tilt rotor configuration. The rotor was modeled as an actuator disk using source singularities, and the rotor wake was represented by a time-averaged cylindrical vortex sheath. A blade element model of the rotor was used to feed time-averaged loading as a function of radial and azimuthal location to the panel code which also contained a model of the wing. The wing was modeled simply as a cambered plate using a lattice of doublet singularities. More recently, Lee [14] computed the 3-D tilt rotor flowfield using an unsteady, time-marching panel method. Wake filaments are shed from the edge of the rotor (modeled as an actuator disk) as well as the wing leading and trailing edges. Both of the above panel models were able to predict many of the overall tilt rotor flow features. Quantitative results, however, because of the nature of the equations solved (Laplace's equation) must be viewed with caution as separated flows cannot be accurately predicted with this formulation without a priori knowledge of separation locations and total or dynamic pressures in the wake region. As found in the experimental work described in Ref. [5], the separation location is very sensitive to leading edge curvature and thickness. Also, swirl in the flowfield can cause early separation on the flap at a considerable distance forward of the trailing edge. These important effects cannot be accurately predicted using a panel method. In fact, in the above panel models, the separation location was fixed at the wing leading and trailing edges. Download, therefore, which is dependent on viscous effects, can only be accurately predicted using an analysis which incorporates the effect of viscosity.

References [5,15] describe discrete-vortex seeding methods to calculate the unsteady, 2-D flow around an airfoil at an angle of attack of -90 degrees, by solving the vorticity transport equation. In Ref. [5], the wing is immersed in a freestream flow. In Ref. [15], to study rotor/wing interaction, a rotor is modeled using constant strength doublet panels which induce a normal velocity distribution. Since no integral boundary layer calculation was coupled with the potential flow calculation, boundary layer growth and separation location were not predicted. Separation location was specified and a uniform base pressure on the wing lower surface was assumed. The methods predicted the upper surface pressures fairly well but were incapable of accurately calculating the lower surface pressure.

Raghavan et al. [16] performed 2-D laminar Navier-Stokes computations on the XV-15 airfoil at -90 degrees angle of attack in a low Mach number and low Reynolds number freestream flow. The converged solution showed a significant periodic unsteadiness in the flowfield due to vortices shedding alternately from the airfoil leading and trailing edges. The mean value of the computed unsteady download did not correspond well with experimental measurements. This was again due to difficulty in predicting the base pressure. The inability to accurately model turbulence in the wake contributed to the observed discrepancies.

Stremel [17] computed the 2-D flowfield about a NACA 0012 airfoil with and without a deflected flap, using a velocity-vorticity formulation of the unsteady incompressible Navier-Stokes equations. His unsteady lift and drag results compared favorably with those of Ref. [16]. As the selected Reynolds number was 200, only laminar flow was computed.

Since the flow over the tilt rotor wing is highly three-dimensional, two-dimensional analyses such as those mentioned above are of limited usefulness. It is anticipated that, in three dimensions, due to a less-constrained flowfield than in two dimensions, the vortex shedding and turbulence in the wing wake will be reduced in strength, and a more accurate prediction of the separated flow region beneath the wing will be possible.

Rotor Modeling

As mentioned earlier, the flowfield of a lifting rotor alone in hover is very complicated. Each blade can be viewed as a rotary wing that sheds a sheet of vorticity in the form of a thin wake which trails the blade in a helical pattern. The change in blade loading occurs mostly at the blade tip. Much of the rotor wake vorticity, therefore, is concentrated in tip vortices which propagate in helices below the rotor disk. It is the combined effect of the vorticity in the wakes from all blades (in addition to the bound vorticity on the blades) that induces the axial and rotational motion in the rotor flowfield — i.e. the downwash and swirl. The acceleration of the flow beneath the rotor gives rise to contraction of the rotor flowfield. Characteristic of the rotor flowfield in hover is the close proximity of the wake shed from one blade to the following blades. These interactions can have a significant impact on local blade loading which affects overall rotor performance (see any text on helicopter aerodynamics; for example, Johnson [18]). Although all features of the flow physics can be accurately modeled only with the Navier-Stokes equations, the rotor flowfield has been modeled using a wide range of methods of varying complexity and accuracy.

Application of momentum theory, or a combination of momentum theory and blade element analysis, to an actuator disk representation of the rotor provides a time- and space-averaged approximation of the rotor loads and the resulting induced velocities in the rotor downwash. The local effect of shed vorticity on the following blades is not computed. Prescribed wake and free wake hover analysis methods model the wake as vortex sheets and filaments. In the prescribed wake approach the wake geometry is specified from experimental data; the free wake approach computes the force-free positions of the vortices. These two methods, in wide use today, are commonly coupled with lifting line or surface representations of the rotor blades. They are valid only for incompressible, potential flows.

The transonic flow on the blades can be computed by solving the full potential equation. This typically requires a finite difference or finite volume solution method which uses a grid around the rotor blades. Because the full potential equation does not allow for the convection of vorticity, modeling a free vortex wake within the finite difference domain must be modeled in Lagrangian fashion where the Biot-Savart law

is used to compute the induced velocities.

The Euler equations permit the transport of vorticity and are therefore better suited to the computation of blade/vortex sheet interaction. Ideally one would use the Euler or Navier-Stokes equations to model the complete rotor flowfield including not only the near-field region around the rotor blades but also the wake region extending below the rotor. Current computer limitations, however, do not permit the solution at the huge number of grid points that would be required to model the flowfield near each blade and the thin vortex sheets and highly concentrated tip vortices that extend far below the rotor. Coarse grids, which might be manageable in terms of available computer resources, are not only unable to resolve the concentrated vorticity, but also introduce unwanted numerical dissipation. This causes excessive, non-physical diffusion of the vorticity leading to inaccuracies in the overall solution.

In Ref. [19], Stremel developed a method to compute the two-dimensional, time-dependent evolution of a vortex wake behind a wing. His velocity-vorticity formulation for the Euler equations permitted the computation of solutions that were relatively independent of grid size. This is an important requirement for future methods in three dimensions that would allow accurate vorticity transport on coarse meshes. Stremel, in Refs. [20,17], extended the method to a velocity-vorticity formulation of the unsteady incompressible Navier-Stokes equations. The convection of finite-core vortices on a coarse mesh was combined with the viscous solution on a fine mesh around a 2-D body. The method allowed for the distribution of the interacting vortices onto the fine mesh.

Using a somewhat different approach, Srinivasan and McCroskey [21] computed airfoil/vortex interaction in two dimensions. They simulated the situation where the shed tip vortex of a rotor blade is parallel to a following blade. They solved the 2-D Euler and Navier-Stokes equations in a perturbation, conservation law form in primitive variables. They refer to their method as a prescribed-vortex or perturbation approach where the structure of the vortex is prescribed. The vortex is convected through the flowfield without being diffused by the numerical dissipation that is inherent in the computational method.

Methods of preserving vorticity on coarse grids are currently being developed for

three-dimensional applications. Typically, however, current rotor flowfield computations eliminate the problems associated with numerical diffusion inherent in the finite difference solution of wakes by modeling the wake region below the rotor using a prescribed or free wake analysis. This wake model is then coupled to a near-field Euler or Navier-Stokes solution around the rotor blades.

For example, Agarwal and Deese [22] solved the unsteady Euler equations for a helicopter rotor in hover using an explicit, finite volume method. The effect of the wake on the rotor was computed using a free wake analysis to determine a correction applied to the geometric angle of attack of the blades due to the local induced downwash. In a similar approach, Roberts [23] coupled an explicit, finite volume Euler solver with a free wake model for a two-bladed hovering rotor. The bound circulation distribution along the span of each rotor blade was determined from the Euler solution and used to set the strength of the wake vortices. The effect of the wake was introduced into the Euler solution by using the wake-induced velocities to define the required outer boundary conditions. Also, the local effect of the trailing vortices was modeled using a prescribed flow perturbation scheme, similar to that implemented in Ref. [21].

Quasi-steady solutions of a 2-bladed rotor in hover have been obtained by Srinivasan and McCroskey [24] using a flux-split, approximately-factored, implicit algorithm to solve the unsteady, thin-layer Navier-Stokes equations. The computation of the vortices shed from the rotor tips is affected adversely by numerical diffusion due to insufficient grid density beneath the rotor. The effect of the shed vorticity in the rotor wake, and in particular, the induced downwash, was estimated in a similar fashion to Ref. [22], where a correction to the effective local angle of attack of the hovering blades was made. In Ref. [25] Srinivasan et al. computed the viscous, three-dimensional flowfield of a lifting 2-bladed helicopter rotor in hover without resorting to any wake models. An upwind, implicit, finite-difference method was used to solve the thin-layer Navier-Stokes equations in a computational domain of limited size that extended only 8 rotor blade chords in all directions. Fine-grid (nearly one million points) results for blade surface pressures corresponded well with experiment, and the roll-up of the tip vortex was computed. This computation, although very impressive, took about 15 CPU hours on the Cray-2 supercomputer. Due to the limited

computational region, a solution was obtained for only two revolutions of the rotor wake before the flow exited the downstream boundary. The results compare more favorably with experiment than those of Ref. [24]. Further work is required, however, to resolve important issues such as rotor drag and power, and detailed wake geometry.

In a computationally less demanding approach, Rajagopalan and Mathur [26] modeled a three-dimensional rotor in forward flight using a distribution of momentum sources added to the steady, incompressible, laminar Navier-Stokes equations. Rotor geometry and blade sectional aerodynamic characteristics were incorporated into the evaluation of the source terms. Their results represent a time-averaged solution. Shed vortex details were not resolved due to the coarseness of the grid. In complexity, this method lies between an actuator disk representation where the blade loads are averaged over the rotor disk and an Euler (or Navier-Stokes) computation of the individual blades.

McCroskey and Baeder [27] estimated that in order to calculate two revolutions of a two-bladed rotor above a simple fuselage using a typical, implicit, thin-layer Navier-Stokes code with algebraic eddy-viscosity modeling of turbulence, a 100 megaflop computer would require 40 CPU hours and 30 million words of memory (or 4 hours of CPU for a one gigaflop machine). It is clear then, that accurate, routine calculations of 3-D rotorcraft flows including detailed modeling of the rotor blades will remain elusive for some time.

1.3 Current Approach

Despite the research efforts of the past several years, gaps in our fundamental understanding of the tilt rotor flowfield remain. It is the objective of this current work, then, to gain a better understanding of this complex flowfield, by modeling it using current computational fluid dynamic (CFD) techniques. It is hoped that many of the limitations imposed by the previously-described two- and three-dimensional methods applied to the tilt rotor flowfield may be removed. In particular, it is desired to compute the wing download of a tilt rotor aircraft in hover, and to study the effects of tangential blowing on download reduction. As can be inferred from the previous

section, however, accurate, simultaneous, numerical prediction of all the tilt rotor flow features discussed in Section 1.1 still lies beyond the state of the art. To render the problem tractable, simplifications are made. Only the wing and rotor are modeled. The fuselage, tail, nacelle, and rotor hub of the tilt rotor aircraft are neglected. Study of the three-dimensional wing/rotor interaction of a tilt rotor configuration in hover, then, is the primary focus of this work. Since accurate modeling of the flow about the individual rotor blades and of the vorticity in the wake is a complex task and a tremendous computational drain, and since the primary interest here is in wing download prediction and not in detailed rotor simulation, the rotor modeling is simplified in this study. The rotor is modeled as an actuator disk where the blade loads are averaged over elemental areas of the rotor disk.

Flow separation from the wing leading edge and from the flap, caused by significant viscous effects, creates a large region of separated flow beneath the wing. This region of the tilt rotor flowfield has a significant impact on wing download. Thus, the Navier-Stokes equations, which model the viscosity in the flow, are used to describe the flowfield. The form of these equations and the method of solution employed in this study are discussed in the next chapter. The flow equations are discretized and solved on a mesh of grid points. Chapter 3 is devoted to a discussion of the development of a suitable 3-D mesh that possesses grid point distributions which permit the resolution of not only the large-scale tilt rotor flowfield features but also the smaller-scale features of the flow about the wing including the boundary layer and flow separations. Chapter 4 discusses the implementation of the boundary conditions required by the Navier-Stokes equations. The unique manner in which the rotor is modeled as an integral part of the Navier-Stokes solution is also discussed. The implementation of the tangential blowing jet is also described. Chapter 5 presents computed results of a rotor alone as well as wing/rotor interaction and compares them with some existing experimental data. Results which show the download reduction effect of tangential blowing are also presented. The final chapter, Chapter 6, summarizes the conclusions drawn from this work and outlines some near and longer term recommendations for further work.

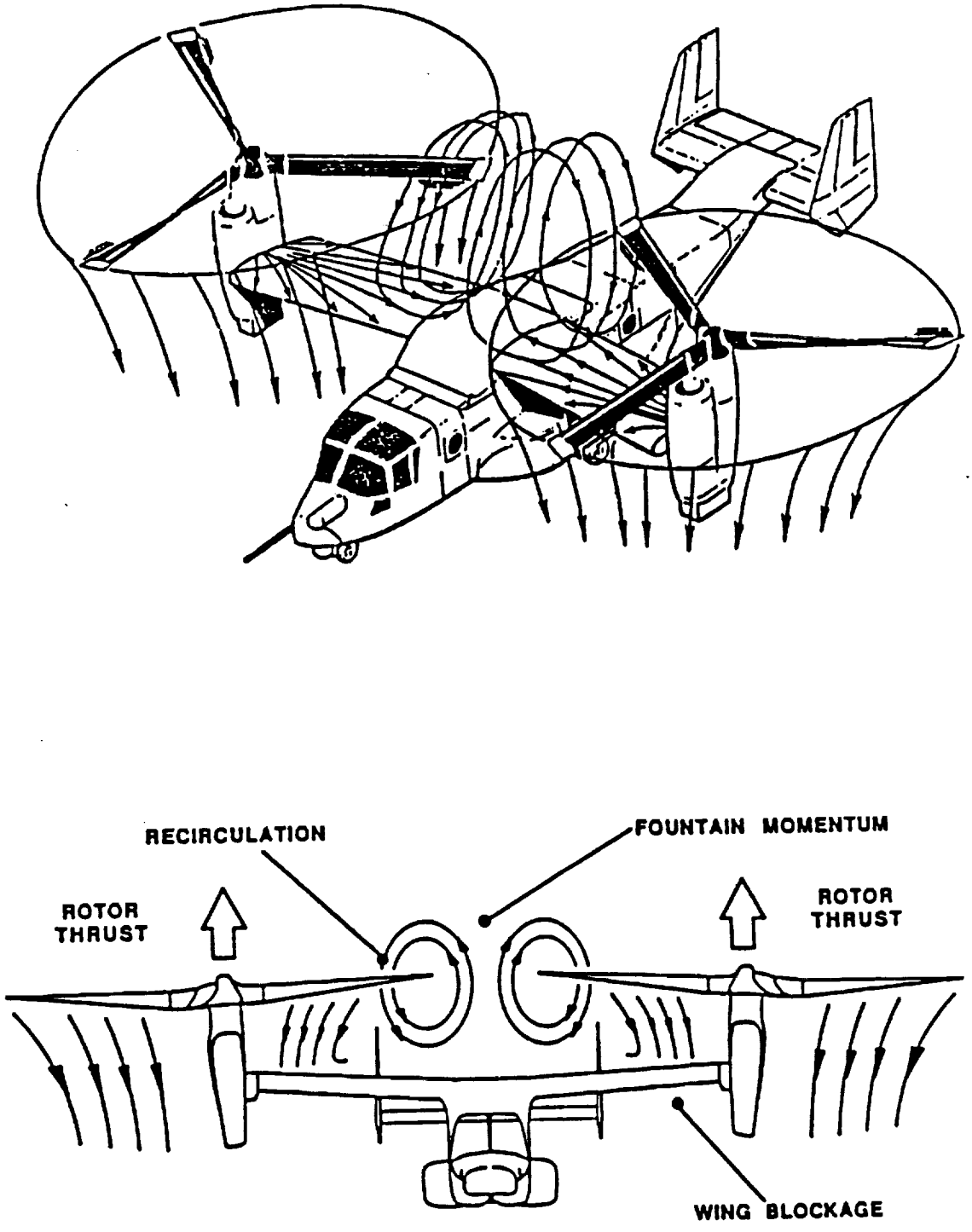

Figure 1: Sketches of the V-22 in hover, showing the main flow features.

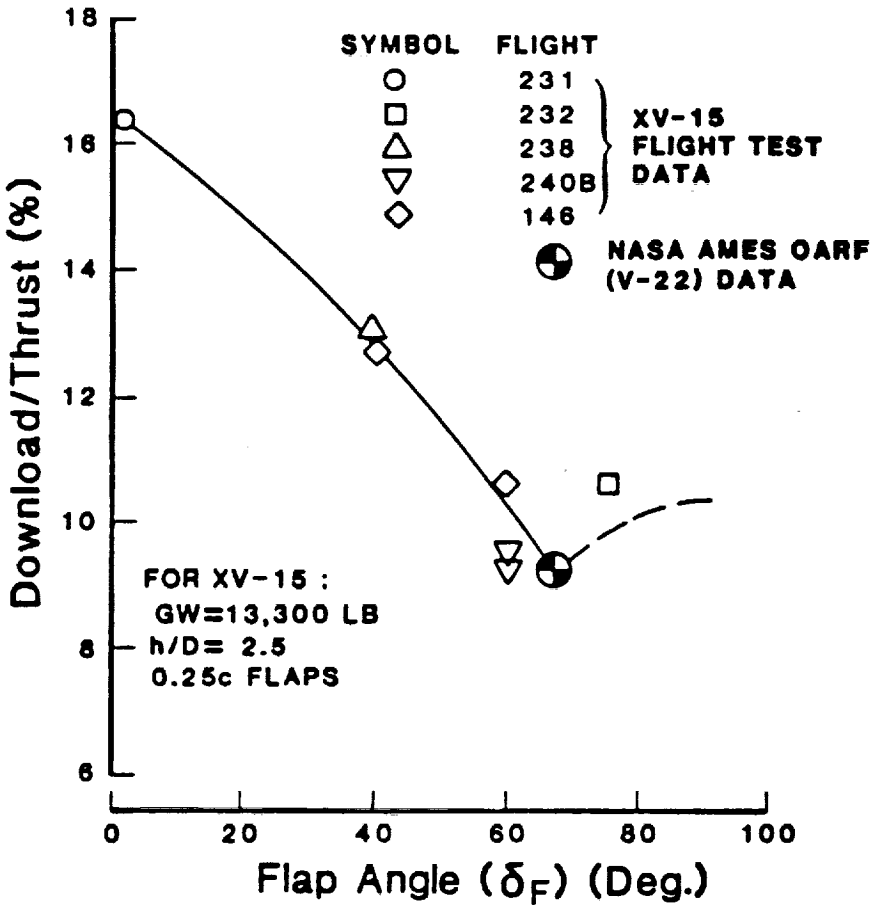

Figure 2: Effect of flap angle on download (taken from Ref. [1]).

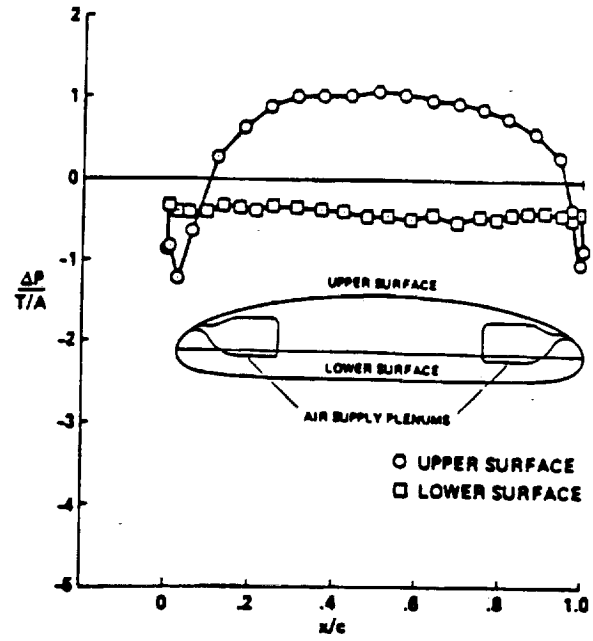

(a) blowing off, $P_p/P_{atm} = 1.00$.

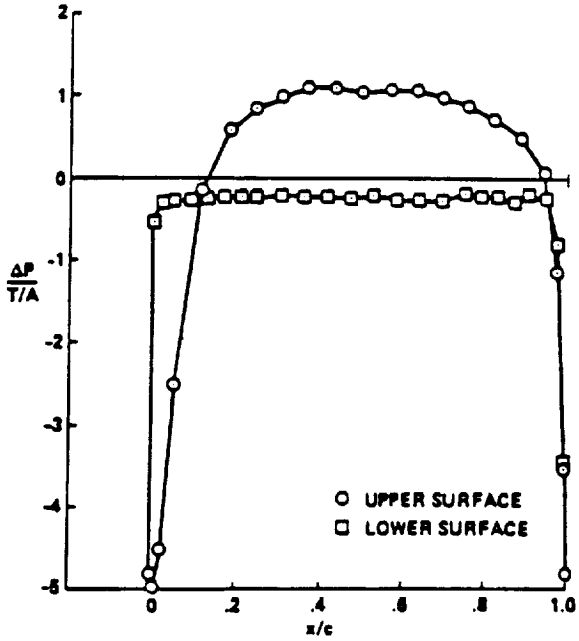

(b) blowing on, $P_p/P_{atm} = 1.09$.

Figure 3: Typical surface pressure distributions measured on a circulation control wing with and without blowing (taken from Ref. [2]).

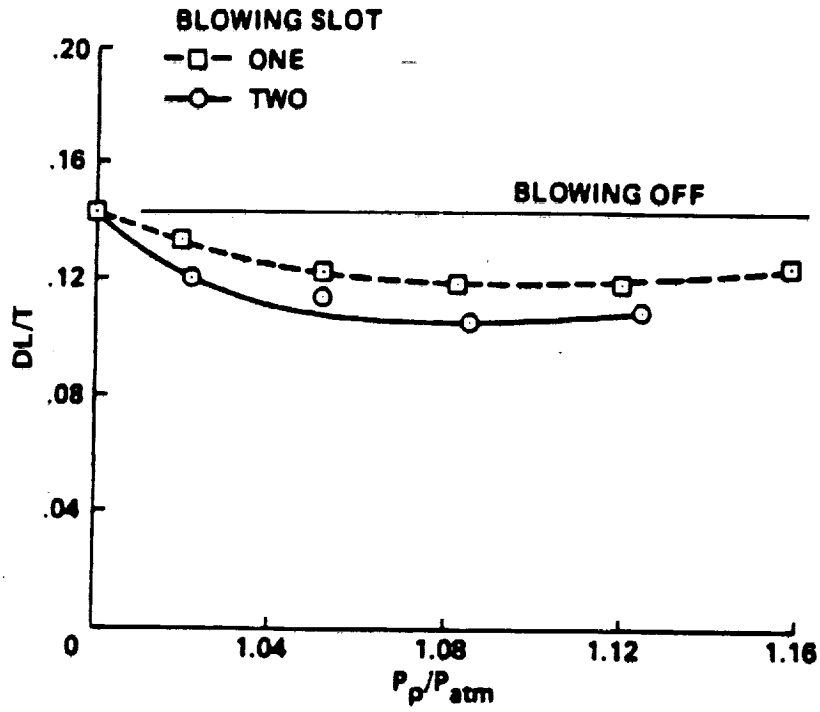

Figure 4: Measured variation in download with blowing plenum pressure (taken from Ref. [2]).

Chapter 2

Flow Equations and Solution Method

2.1 General Comments

In this study the flowfield about a tilt rotor configuration is represented by the unsteady thin-layer Navier-Stokes partial differential equations. It is assumed that there are no body forces (eg. gravity effects are not important) and there is no heat addition or removal. The thin-layer approximation, described later, assumes that the viscous forces are confined to a small region near the wing surface. The basic solution algorithm, employed to solve the equations, is referred to as the LU-ADI scheme developed by Obayashi and Kuwahara [28]. It was extended and applied in a Fortran computer code called "LANS3D" to a three-dimensional transonic wing calculation [29] and a wing-fuselage transonic flow computation [30] by Fujii and Obayashi. Yeh et al. applied this code to the Navier-Stokes computation of the flow about a delta wing with spanwise [31] as well as tangential [32] leading edge blowing used to control vortex shedding.

The solution algorithm, then, has been shown in the above-mentioned references to be robust and efficient for thin-layer Navier-Stokes computations. Although the numerical time integration is performed in an implicit fashion, the boundary conditions are updated explicitly. This allows easier application of the method to a

wide variety of geometries and grid topologies. It was therefore decided, for the research undertaken in this current work, to utilize the basic numerical scheme implemented in that version of "LANS3D" previously applied to delta wing computations by Yeh et al. [31,32,33]. Much of the effort involved in the research reported here has focused on implementing and extending the above method to model the current problem of interest — the tilt rotor flowfield in hover.

This chapter outlines the basic formulation of the equations and their method of solution. Greater details of the basic numerical algorithm can be found in Refs. [28, 29,30,33]. Also discussed in this chapter are the modifications to the basic solution algorithm that were implemented to provide an effective mechanism for modeling the rotor and also the tangential jet on the wing surface. These modifications involve exploiting the "blanking" feature of the so-called "chimera" technique [34]. This is described in more detail later in this chapter and in Chapter 5. Also outlined briefly in this chapter are the turbulence models employed for the general flowfield about the wing and in the region of the tangential jet.

2.2 Governing Equations

The Navier-Stokes equations are the most basic continuum-representation of fluid dynamic flows. The equations are written and solved in conservation-law form where the dependent variables are expressed in the form of spatial gradients (see, for example, Refs. [33,35]). Although not particularly significant in the current low Mach number application where the locally-transonic rotor blade flow is not computed, the conservation-law form ensures proper shock capturing (i.e. accurate prediction of shock location and strength) for transonic flows. To convert the equations to a more useful form for computational purposes and to apply the thin-layer approximation, the full three-dimensional Navier-Stokes equations are first manipulated somewhat, as described below.

For convenience, the equations are non-dimensionalized. The density ρ is divided by the freestream density ρ_∞, the velocity components u, v, and w by the freestream

speed of sound a_∞, and the total energy per unit volume e by $\rho_\infty a_\infty^2$. Conforming to the normal convention, u is in the wing chord (x) direction (positive aft), v is in the wing spanwise (y) direction (positive outboard), and w is in the vertical (z) direction (positive upwards). The coefficient of viscosity μ is normalized by μ_∞ and the time is normalized by c/a_∞ where c is the wing chord. Applying this non-dimensionalization to the Navier-Stokes equations results in a term containing the expression $(\rho_\infty a_\infty c)/\mu_\infty$ which is simply the Reynolds number Re based on the freestream speed of sound.

Next, the Navier-Stokes equations are transformed from Cartesian coordinates (x, y, z, t) to a generalized, body-fitted, curvilinear coordinate system (ξ, η, ζ, τ). This makes the formulation independent of the body geometry thereby easing the specification of the boundary conditions. It also allows for straight-forward application of the thin-layer assumption. In addition, since the physical domain is transformed into a computational domain which is a rectangular parallelepiped with uniformly-sized mesh cells, then standard differencing schemes for equi-spaced grid points can be used for the spatial derivatives. The coordinate transformation is defined by:

$$\begin{aligned} \xi &= \xi(x, y, z, t) \\ \eta &= \eta(x, y, z, t) \\ \zeta &= \zeta(x, y, z, t) \\ \tau &= t \end{aligned} \tag{1}$$

where t and τ are the independent variables of time in the physical and transformed coordinates, respectively. The airfoil surface in the chordwise direction is transformed to the ξ-coordinate, the spanwise direction is transformed to η, and ζ is normal to the wing surface. Details of this transformation procedure can be found in Refs. [36,37]. By writing the transformation in terms of spatial derivatives and applying the chain rule, a transformation Jacobian J and several identities called metrics can be defined as follows:

$$J = 1/\det \begin{vmatrix} x_\xi & x_\eta & x_\zeta \\ y_\xi & y_\eta & y_\zeta \\ z_\xi & z_\eta & z_\zeta \end{vmatrix} \tag{2}$$

where $x_\xi = \partial x/\partial \xi$, $x_\eta = \partial x/\partial \eta$, etc. The metrics are given by:

$$\begin{aligned}
\xi_x &= J\,(y_\eta z_\zeta - y_\zeta z_\eta), & \zeta_x &= J\,(y_\xi z_\eta - y_\eta z_\xi) \\
\xi_y &= J\,(x_\zeta z_\eta - x_\eta z_\zeta), & \zeta_y &= J\,(x_\eta z_\xi - x_\xi z_\eta) \\
\xi_z &= J\,(x_\eta y_\zeta - x_\zeta y_\eta), & \zeta_z &= J\,(x_\xi y_\eta - x_\eta y_\xi) \\
\eta_x &= J\,(y_\zeta z_\xi - y_\xi z_\zeta), & \xi_t &= -x_\tau \xi_x - y_\tau \xi_y - z_\tau \xi_z \\
\eta_y &= J\,(x_\xi z_\zeta - x_\zeta z_\xi), & \eta_t &= -x_\tau \eta_x - y_\tau \eta_y - z_\tau \eta_z \\
\eta_z &= J\,(x_\zeta y_\xi - x_\xi y_\zeta), & \zeta_t &= -x_\tau \zeta_x - y_\tau \zeta_y - z_\tau \zeta_z
\end{aligned} \tag{3}$$

Note that for stationary grids (no body motion), the metric time derivative terms are zero. From a finite volume point of view, the transformation Jacobian J is the inverse of the local grid cell volume, and the metrics are grid cell area projections.

Generally, for aerodynamic applications of practical interest (particularly in three dimensions), the thin-layer approximation is applied to the Navier-Stokes equations to reduce the computational effort. For the relatively high Reynolds numbers which are typical of such problems, the viscous effects are confined to a small region near the body surface and in the wake. Computer memory limitations usually necessitate concentrating the available grid points near the surface of interest in order to resolve the boundary layer. This results in grid spacing that is fine, normal and near to the surface, and that is relatively coarse, tangential to the surface. With this type of grid, even if the full Navier-Stokes equations were solved, the viscous terms possessing velocity gradients tangential to the body would not be resolved because of insufficient grid density along the surface. For most cases of interest (i.e. high Re flows), however, these terms are negligible anyway. Therefore, it is justifiable to eliminate from the calculation the viscous fluxes associated with the directions parallel to the surface, i.e. the ξ- and η- directions. This approximation is easily applied since the equations are already transformed into the body-fitted computational domain. The thin-layer approximation is similar in philosophy to the assumptions made in boundary layer theory. Less restrictive than boundary layer theory, however, the thin-layer approximation retains the normal momentum equation and allows pressure variation across the boundary layer.

Beneath the wing of the tilt rotor configuration in hover the flow is turbulent, unsteady, and separated, as mentioned in Chapter 1. In such a flow, all components of the viscous stress exist and are probably important and shouldn't be neglected. This, then, is one of the major limitations of the present method for studying the tilt rotor flowfield. Even if the full Navier-Stokes equations were solved, however, limitations of the turbulence model (discussed in the next section) in regions of extensive separation would contribute to inaccuracies in the computed flowfield. Nonetheless, the current approach makes the calculation tractable and far superior to any method hitherto applied to this problem.

Applying the thin-layer approximation, then, the non-dimensional, three-dimensional, unsteady Navier-Stokes equations in conservation-law form in transformed, body-fitted, curvilinear coordinates become:

$$\frac{\partial \hat{Q}}{\partial \tau} + \frac{\partial \hat{E}}{\partial \xi} + \frac{\partial \hat{F}}{\partial \eta} + \frac{\partial \hat{G}}{\partial \zeta} = \frac{1}{Re}\frac{\partial \hat{G}_v}{\partial \zeta} \tag{4}$$

where the symbol '^' indicates transformed variables. The $\hat{Q}$ vector contains the transformed, conservative flow variables:

$$\hat{Q} = J^{-1}\begin{bmatrix} \rho \\ \rho u \\ \rho v \\ \rho w \\ e \end{bmatrix} \tag{5}$$

Note that the elements of the $\hat{Q}$ vector, as well as all flow variables referred to in subsequent discussions in this chapter, are non-dimensional quantities, unless noted otherwise.

The vectors $\hat{E}$, $\hat{F}$ and $\hat{G}$ contain the inviscid (or "Euler") terms. The vector $\hat{G}_v$ contains all the viscous terms that remain after application of the thin-layer approximation. The elements of these vectors are shown below:

$$\hat{E} = \frac{1}{J}\begin{bmatrix} \rho U \\ \rho u U + \xi_x p \\ \rho v U + \xi_y p \\ \rho w U + \xi_z p \\ (e+p)U - \xi_t p \end{bmatrix}, \qquad \hat{F} = \frac{1}{J}\begin{bmatrix} \rho V \\ \rho u V + \eta_x p \\ \rho v V + \eta_y p \\ \rho w V + \eta_z p \\ (e+p)V - \eta_t p \end{bmatrix}$$

$$\hat{G} = \frac{1}{J}\begin{bmatrix} \rho W \\ \rho u W + \zeta_x p \\ \rho v W + \zeta_y p \\ \rho w W + \zeta_z p \\ (e+p)W - \zeta_t p \end{bmatrix}, \qquad \hat{G}_v = \frac{1}{J}\begin{bmatrix} 0 \\ \zeta_x \tau_{xx} + \zeta_y \tau_{xy} + \zeta_z \tau_{xz} \\ \zeta_x \tau_{yx} + \zeta_y \tau_{yy} + \zeta_z \tau_{yz} \\ \zeta_x \tau_{zx} + \zeta_y \tau_{zy} + \zeta_z \tau_{zz} \\ \zeta_x \beta_x + \zeta_y \beta_y + \zeta_z \beta_z \end{bmatrix} \tag{6}$$

where p is the static pressure and U, V, and W are the contravariant velocity components that appear as a result of the coordinate transformation. The contravariant velocity U is the component of velocity parallel to the wing surface and in the direction of the wing chord, V is the component of velocity in the spanwise direction, and W is normal to the wing surface. They are given below:

$$\begin{aligned} U &= \xi_t + \xi_x u + \xi_y v + \xi_z w \\ V &= \eta_t + \eta_x u + \eta_y v + \eta_z w \\ W &= \zeta_t + \zeta_x u + \zeta_y v + \zeta_z w \end{aligned} \tag{7}$$

The components of the viscous stress are defined by:

$$\begin{aligned} \tau_{xx} &= -\frac{2}{3}\mu(u_x + v_y + w_z) + 2\mu u_x \\ \tau_{yy} &= -\frac{2}{3}\mu(u_x + v_y + w_z) + 2\mu v_y \\ \tau_{zz} &= -\frac{2}{3}\mu(u_x + v_y + w_z) + 2\mu w_z \\ \tau_{xy} &= \tau_{yx} = \mu\,(u_y + v_x) \\ \tau_{xz} &= \tau_{zx} = \mu\,(u_z + w_x) \\ \tau_{yz} &= \tau_{zy} = \mu\,(v_z + w_y) \\ \beta_x &= \frac{\gamma\mu}{Pr}\partial_x e_i + u\tau_{xx} + v\tau_{xy} + w\tau_{xz} \end{aligned} \tag{8}$$

$$\beta_y = \frac{\gamma\mu}{Pr}\partial_y e_i + u\tau_{yx} + v\tau_{yy} + w\tau_{yz}$$
$$\beta_z = \frac{\gamma\mu}{Pr}\partial_z e_i + u\tau_{zx} + v\tau_{zy} + w\tau_{zz}$$

where $u_x = \partial u/\partial x$, $v_y = \partial v/\partial y$, $\partial_x e_i = \partial e_i/\partial x$, etc. From the definition of the total energy e, the internal energy per unit mass is

$$e_i = \frac{e}{\rho} - \frac{(u^2 + v^2 + w^2)}{2}$$

The Prandtl number Pr is defined as $Pr = c_p\mu/k$ where c_p is the specific heat at constant pressure and k is the coefficient of thermal conductivity. Also, γ is the ratio of specific heats which, for air, is equal to 1.4. Pressure is related to the conservative flow variables through the equation of state for a perfect gas:

$$p = (\gamma - 1)\left[e - \frac{\rho}{2}\left(u^2 + v^2 + w^2\right)\right] \tag{9}$$

To evaluate the spatial derivatives of the Cartesian velocity components in Eq. 8, the chain rule is applied. For example,

$$u_x = \xi_x u_\xi + \eta_x u_\eta + \zeta_x u_\zeta$$

Implicit in the expressions for the viscous stresses (Eq. 8) is the assumption that the fluid is Newtonian (viscous stresses are linearly related to the rate of strain) and that its properties are isotropic (having no preferred direction), and that it satisfies Stokes' hypothesis which states that the bulk viscosity $(\lambda + 2/3\mu)$ is zero. Experience of many researchers over many years has shown that these assumptions are valid for most flows of aerodynamic interest.

2.3 Turbulence Model

The unsteady Navier-Stokes equations are generally considered to accurately represent the physics of turbulent flows. In order, however, for a numerical solution of these equations to resolve all scales associated with the turbulent eddies for large Reynolds number flows, an extremely dense grid spacing resulting in a huge number

of grid points would be required. Because of computer memory and speed limitations, grids can not be made fine enough to fully capture the turbulence in the flow. It is therefore necessary to use models for simulating turbulence.

The approach employed here is commonly taken for large Reynolds number 3-D compressible Navier-Stokes computations. The Navier-Stokes equations are time-averaged using a mass-weighted variable approach (refer, for example, to Ref. [38]). The velocities and thermal dependent variables such as temperature and enthalpy are split into a mass-averaged mean-flow part and a mass-averaged fluctuating quantity. The pressure and density are defined as having a mean-flow part and a fluctuating contribution which is not mass-averaged. Time-averaging gives rise to new terms in the resulting "Reynolds-averaged" Navier-Stokes equations. These new terms can be interpreted as "apparent" stress gradients and heat-flux quantities due to turbulent motion. The turbulent stresses are commonly referred to as Reynolds stresses. Applying the Bousinesq assumption which relates the Reynolds stresses to the rate of strain, the effect of turbulence can be approximated by an effective viscosity often called "eddy" viscosity that is due to the additional mixing caused by the turbulent flow. This turbulent viscosity model is far less demanding computationally than more complicated (and more or less accurate) approaches which typically require the solution of additional differential equations that model the characteristics of turbulence. To limit the computational requirements of an already demanding three-dimensional problem, a simple algebraic turbulence model, discussed in the next section, is employed in this work. The total effective viscosity can then be defined as the sum of a laminar contribution (μ_l) and a turbulent part (μ_t):

$$\mu = \mu_l + \mu_t \tag{10}$$

The laminar viscosity contribution is determined from Sutherland's formula:

$$\mu_l = \mu_{ref} \left(\frac{T}{T_{ref}} \right)^{3/2} \frac{T_{ref} + 198.6°R}{T + 198.6°R} \tag{11}$$

where T is the temperature in degrees Rankine (°R). The turbulent contribution to viscosity μ_t is obtained from the algebraic turbulence model.

Similarly, the total effective coefficient of thermal conductivity is expressed as:

$$\begin{aligned} k &= k_l + k_t \\ &= \frac{c_p \mu_l}{Pr_l} + \frac{c_p \mu_t}{Pr_t} \end{aligned} \tag{12}$$

For the range of temperatures and pressures of interest here, for air, the laminar Prandtl number Pr_l is 0.72 and the turbulent Prandtl number Pr_t is 0.90 (see, for example, Ref. [38]).

An algebraic turbulence model developed by Baldwin and Lomax [39] for boundary layers has been employed for the computations undertaken in this study. It is applied to the flowfield around the wing. Because jet flows possess somewhat different turbulence characteristics, another turbulence model more appropriate for the blowing region is used. An eddy viscosity model proposed by Roberts [40] for turbulent wall jets on curved surfaces is implemented. These two turbulence models are discussed briefly below. Based on a combination of theory and empiricism, these models, although far from precise predictors of turbulence, do provide a means of improving the simulation of a real flow.

2.3.1 The Baldwin-Lomax Model

The eddy viscosity model of Baldwin and Lomax [39] is in common use today for estimating the effect of turbulence in aerodynamic flows. It uses a two layer formulation that includes an inner region (where the wall has a considerable influence on eddy size) and an outer region.

The eddy viscosity in the inner region is estimated using the Prandtl-Van Driest formulation:

$$(\mu_t)_{inner} = \rho l^2 |\omega| \tag{13}$$

where $|\omega|$ is the magnitude of the vorticity ($|\nabla \times \vec{V}|$) and l is the "mixing" length scale. In the outer region, the eddy viscosity is written as

$$(\mu_t)_{outer} \propto F_{max}\, \zeta_{max} \tag{14}$$

where F_{max} and ζ_{max} represent the turbulent velocity and length scales in the outer part of the boundary layer. The quantity F_{max} is the maximum value of the following

function:

$$F(\zeta) = \zeta\,|\omega|\left[1 - \exp\left(-\zeta^{+}/A^{+}\right)\right] \tag{15}$$

where $\zeta^{+} = \zeta\sqrt{\rho_w \tau_w}/\mu_w$ and the subscript w represents the conditions at the wall. A^{+} is a constant equal to 26, and ζ is the distance of a point in the flowfield normal to the nearest solid wall. The value ζ_{max} is the ζ-location where $F(\zeta)$ reaches a maximum in a given velocity profile. In wake regions, because of the relatively-large distance from the wing surface, ζ^{+} becomes increasingly large and the exponential term of Eq. 15 approaches a value of zero. As suggested by Baldwin and Lomax, for points in the wake, the exponential term is omitted. For the download computation, this is applied to all points beneath the wing in the wake.

2.3.2 Turbulence Model for Wall Jet

The algebraic turbulence model, briefly described here, is used in the region of the thin, tangential jet on the wing surface. Based on a semi-empirical theory by Roberts [40], it was previously applied by Yeh [33] in the numerical study of delta wing leading edge blowing.

Assuming self-similar velocity profiles typical of free jet flows, Roberts obtained a simple expression for the eddy viscosity of a wall jet:

$$\mu_t = \frac{K}{4k^2}\, V_{max}\, b \left(\frac{\zeta}{\zeta_{max}}\right)^2 \tag{16}$$

where $K = 0.073$ and $k = 0.8814$. Also, V_{max} is the maximum value of the magnitude of velocity in a given velocity profile. Here ζ_{max} represents the ζ-location corresponding to V_{max}. The parameter b is the normal distance from the wall to the ζ-location where the velocity is $V_{max}/2$. Experiments have shown b to have a value of about $7\zeta_{max}$. For $\zeta > \zeta_{max}$, ζ/ζ_{max} is set to one.

Surface curvature causes extra rates of strain in the flow which affect the turbulence structure by influencing the radial distribution of velocity fluctuations. According to Shrewsbury [41], this can increase the effective viscosity by an order of magnitude greater than planar flows. The ratio $-(V/R)\,/\partial V/\partial\zeta$ represents the extra rate of strain produced by the curvature normalized by the inherent shear strain,

where R is the radius of curvature. This effect is added to the jet-induced viscosity of Eq. 16 to obtain an estimate for the eddy viscosity of a curved wall jet:

$$\mu_t = \frac{7K}{4k^2} V_{max}\, \zeta_{max} \left(\frac{\zeta}{\zeta_{max}}\right)^2 \left(1 - \frac{V/R}{\partial V/\partial \zeta}\right) \tag{17}$$

This turbulence model for the jet is applied in the region of the wall jet from the jet exit slot to the flow separation point.

2.4 Numerical Algorithm

The numerical algorithm used here to solve the three-dimensional compressible thin-layer Navier-Stokes equations is an implicit, time-accurate, finite difference scheme developed by Fujii and Obayashi [29,30]. The algorithm has been extended in this work to allow the "blanking out" or excluding of specified regions of the computational domain from the implicit solution. Values of the solution vector at these blanked (excluded) locations are then updated explicitly using values obtained from an independent analysis. This is a very convenient and effective means of modeling the rotor, as is discussed in greater detail later. The numerical algorithm is briefly outlined below.

The solution technique employs an implicit, approximately-factored, non-iterative method developed by Beam and Warming [42]. Explicit methods suffer the disadvantage of having a severe restriction on time step size in order to maintain stability. This is particularly acute for Navier-Stokes solutions where, because of the relatively small scales associated with resolving the boundary layer, the partial differential equations are very stiff. Often, the steady-state solution is of principal interest, so being able to use large time steps to accelerate the rate of convergence is very important. Implicit methods are stable for relatively large time steps even for highly nonlinear equations such as the Navier-Stokes equations.

A first-order accurate implicit time integration scheme is selected to march the solution of the unsteady Navier-Stokes equations in time. A second-order accurate (or higher) scheme is not used as it would necessitate saving the solution from previous time levels, resulting in a significant increase in the computer memory requirements.

The method, as used here, already requires considerable memory for 3-D computations. Applying, then, to Eq. 4, the first-order accurate numerical time integration method referred to as the implicit (or backward) Euler scheme (not to be confused with the "Euler" fluid dynamic equations) yields

$$\hat{Q}^{n+1} - \hat{Q}^n + h\left(\frac{\partial \hat{E}^{n+1}}{\partial \xi} + \frac{\partial \hat{F}^{n+1}}{\partial \eta} + \frac{\partial \hat{G}^{n+1}}{\partial \zeta} - \frac{1}{Re}\frac{\partial \hat{G}_v^{n+1}}{\partial \zeta}\right) = 0 \tag{18}$$

where h is the time step, $n+1$ is the time at which $\hat{Q}$ is desired, n is the previous time level at which $\hat{Q}$ is known everywhere, and $\hat{Q}^n = \hat{Q}(nh)$.

Since the flux vectors $\hat{E}$, $\hat{F}$, $\hat{G}$, and $\hat{G}_v$ are nonlinear functions of $\hat{Q}$, then Eq. 18 is nonlinear in $\hat{Q}^{n+1}$. In order for the solution method to be non-iterative, so as to limit the computational effort to a manageable level, the nonlinear terms are linearized in time about $\hat{Q}^n$ by a Taylor series expansion such that

$$\begin{aligned}
\hat{E}^{n+1} &= \hat{E}^n + A^n \Delta\hat{Q}^n + O\left(h^2\right) \\
\hat{F}^{n+1} &= \hat{F}^n + B^n \Delta\hat{Q}^n + O\left(h^2\right) \\
\hat{G}^{n+1} &= \hat{G}^n + C^n \Delta\hat{Q}^n + O\left(h^2\right) \\
\hat{G}_v^{n+1} &= \hat{G}_v^n + M^n \Delta\hat{Q}^n + O\left(h^2\right)
\end{aligned} \tag{19}$$

Note that $\Delta\hat{Q}^n = \hat{Q}^{n+1} - \hat{Q}^n$. Also, A^n, B^n, C^n, and M^n are the flux Jacobian matrices given by:

$$A^n = \frac{\partial \hat{E}}{\partial \hat{Q}}, \quad B^n = \frac{\partial \hat{F}}{\partial \hat{Q}}, \quad C^n = \frac{\partial \hat{G}}{\partial \hat{Q}}, \quad M^n = \frac{\partial \hat{G}_v}{\partial \hat{Q}} \tag{20}$$

where the symbol '$\hat{}$' has been omitted from the flux Jacobian matrices for simplicity. Expressions for these matrices can be found in Ref. [43].

In the Beam and Warming method, the alternating direction implicit (ADI) algorithm replaces the inversion of one huge matrix — which would be prohibitively expensive to compute — with the inversions of three block tridiagonal matrices, one for each direction. Efficient block tridiagonal inversion routines exist, making this algorithm a viable solution technique. Substituting the linearizations of Eq. 19 into Eq. 18 and applying the Beam-Warming approximate factorization yields

$$
\begin{aligned}
&[I + i_b\, h\delta_\xi A^n - i_b\, D_I|_\xi]\,[I + i_b\, h\delta_\eta B^n - i_b\, D_I|_\eta] \\
&\quad \left[I + i_b\, h\delta_\zeta C^n - i_b\, hRe^{-1}\delta_\zeta J^{-1} M^n J - i_b\, D_I|_\zeta\right] \Delta\hat{Q}^n \\
&\quad = -i_b\, h\left[\delta_\xi \hat{E}^n + \delta_\eta \hat{F}^n + \delta_\zeta \hat{G}^n - Re^{-1}\delta_\zeta \hat{G}_v^n\right] \\
&\quad\quad -i_b\,[D_E|_\xi + D_E|_\eta + D_E|_\zeta]\,\hat{Q}^n
\end{aligned}
\tag{21}
$$

where I is the identity matrix. D_I and D_E are, respectively, the implicit and explicit artificial dissipation terms required for numerical stability; they are discussed in more detail later. The significance of the integer i_b is discussed below. Also, δ is a second-order central difference operator.

The algorithm is first-order accurate in time and second order-accurate in space. The validity of using a first-order accurate (in time) scheme for unsteady computations is justified later in this section. The reasons for selecting second-order accurate differences for the spatial derivatives are outlined in the last section of this chapter. The equations are solved in "delta form" where $\Delta\hat{Q}^n = \hat{Q}^{n+1} - \hat{Q}^n$. The left hand side of Eq. 21 is called the "implicit" part and the right hand side the "explicit" part of the algorithm. This is a useful formulation because, for steady-state solutions, $\Delta\hat{Q}^n \to 0$, and the solution is independent of the choice of implicit operators on the left hand side of Eq. 21. In the above notation,

$$
[I + i_b h\, \delta_\xi A^n]\,\Delta\hat{Q}^n = \Delta\hat{Q}^n + i_b h\, \delta_\xi \left(A^n \Delta\hat{Q}^n\right)
$$

Note that the central difference operator δ acts on $A^n\Delta Q^n$, not on just A^n.

In Ref. [34], Benek, Buning, and Steger discuss a new 3-D grid embedding scheme, which they refer to as a "chimera" scheme after the Greek mythological creature that possessed several incongruous parts. This technique allows for solutions of multiple overlapping grids. An embedded mesh introduces a "hole" into the mesh in which it is embedded. The grid points that lie within this "hole" can be excluded ("blanked") from the solution of the encompassing mesh. Interpolation between overlapping grids is used to specify boundary values for the solution of each grid. The solution is performed alternately on each mesh. Since only one global mesh is defined for the computations performed in this study (refer to Chapter 3), the grid interpolation

portion of chimera is not required. The blanking capability for selected regions of the computational domain, however, offers a unique and effective means of modeling the rotor and also the tangential jet on the wing surface. The specific details describing how the rotor and jet are implemented in the computation are discussed in Chapter 4. Additional descriptions of the chimera method can be found in Refs. [44,45] where applications to moving grids are described. The analysis in this chapter demonstrates how the blanking feature is implemented in the basic LU-ADI algorithm.

The blanking feature of the chimera scheme requires that an integer i_b be defined and assigned a value of zero or one at every grid point. Equation 21 gives the implementation for the Beam-Warming method. If $i_b = 0$, the $\Delta\hat{Q}^n$ at this grid location becomes zero and the solution at this point remains unchanged. Values of the flow parameters are updated explicitly using a separate analysis. In the case of the rotor, for example, a momentum theory/blade element analysis is applied at the blanked rotor grid points (refer to Chapter 4). If $i_b = 1$, the location is not blanked and the implicit treatment of the solution remains unchanged.

Each ADI operator forms a block tridiagonal matrix. Most of the computational effort involved in an implicit method such as the one outlined above is associated with the inversion of the block tridiagonal matrices. The computational efficiency can be enhanced significantly by applying a matrix diagonalization introduced by Pulliam and Chaussee [46]. In this way, the matrix in each of the three directions can be reduced to a scalar tridiagonal. Their approach is based on the fact that the flux Jacobian matrices A, B, and C each have real eigenvalues and a complete set of eigenvectors. This means that the flux Jacobians can each be diagonalized by similarity transformations as indicated below:

$$\Lambda_A = T_\xi^{-1} A T_\xi, \quad \Lambda_B = T_\eta^{-1} B T_\eta, \quad \Lambda_C = T_\zeta^{-1} C T_\zeta \tag{22}$$

where, for simplicity, the superscript n has been dropped. Λ_A, Λ_B, and Λ_C are diagonal matrices containing the eigenvalues of matrices A, B, and C, respectively. The elements of the diagonal matrices are the characteristic speeds of the flow. In

the transformed coordinate system, the matrix Λ_A, for example, is given as

$$\Lambda_A = \begin{bmatrix} U & 0 & 0 & 0 & 0 \\ 0 & U & 0 & 0 & 0 \\ 0 & 0 & U & 0 & 0 \\ 0 & 0 & 0 & U + a\sqrt{\xi_x^2 + \xi_y^2 + \xi_z^2} & 0 \\ 0 & 0 & 0 & 0 & U - a\sqrt{\xi_x^2 + \xi_y^2 + \xi_z^2} \end{bmatrix} \tag{23}$$

T_ξ, T_η, and T_ζ are similarity transformation matrices. Expressions for the other diagonal matrices and the transformation matrices can be found in Refs. [46,47].

In the ξ-direction, for example, the Beam-Warming ADI operator can be written in the diagonal form as

$$\begin{aligned} &[I + i_b\, h\delta_\xi A - i_b\, D_I|_\xi] \\ &\quad = T_\xi T_\xi^{-1} + i_b\, h\, \delta_\xi \left(T_\xi \Lambda_A T_\xi^{-1}\right) - i_b\, T_\xi\, D_I|_\xi\, T_\xi^{-1} \\ &\quad \approx T_\xi \left[I + i_b\, h\delta_\xi \Lambda_A - i_b J^{-1} \epsilon_I \delta_\xi^2 J\right] T_\xi^{-1} \end{aligned} \tag{24}$$

where second-order implicit smoothing has been prescribed. The implicit smoothing factor ϵ_I is the product of a user-specified constant K_I, the time step h, and the spectral radius σ_A (maximum of the absolute values of the eigenvalues) of the matrix A, i.e. $\epsilon_I = K_I\, h\, \sigma_A$.

Moving T_ξ and T_ξ^{-1} outside of the difference operator δ_ξ introduces an error which renders the method (at best) first-order accurate in time [46]. For steady-state calculations, where the right hand side of Eq. 21 goes to zero as $\Delta\hat{Q}^n \rightarrow 0$, the converged solution obtained using the diagonal algorithm is identical to that obtained from the original Beam-Warming ADI scheme since the right hand side is the same for both methods. For unsteady calculations, however, the Pulliam-Chaussee diagonalized algorithm introduces the possibility of nonconservative errors in the time varying part of the solution. Shock speeds, for example, may be incorrectly computed. This, however, should not be a significant problem in the current application. Shocks, if they occur at all in the tilt rotor flowfield, are located on the upper surface of the rotor blade tip region. In the current formulation though, the rotor is modeled as an actuator disk (see chapter 4) where the detailed flow about each blade is not computed anyway. In addition, Pulliam and Chaussee, in Ref. [46], indicate that, based

on numerical experimentation, their method is applicable to unsteady flows without shocks. Also, Guruswamy [48,49] obtained accurate results for both unsteady Euler and Navier-Stokes aerodynamic and aeroelastic calculations using the diagonalized form of the Beam-Warming method.

Fujii, Obayashi, and Kuwahara [28,29,30] introduced a further modification to the left hand side operators that reduces each tridiagonal matrix — obtained after the diagonalization described above — to a product of a lower and an upper bidiagonal matrix, thereby further reducing the computational effort. This is possible by employing a flux vector splitting technique and by using a diagonally dominant factorization. These modifications are outlined below.

The central differencing in Eq. 24 is decomposed into two one-sided differences using the flux vector splitting technique of Steger and Warming [50]. The ξ-direction operator becomes:

$$[I + i_b\, h\delta_\xi A - i_b\, D_I|_\xi] = T_\xi \left[I + i_b\, \nabla_\xi \Lambda_A^+ + i_b\, \Delta_\xi \Lambda_A^-\right] T_\xi^{-1} \tag{25}$$

where

$$\Lambda_A^\pm = \frac{h}{2}\left(\Lambda_A \pm |\Lambda_A|\right) \pm \mathcal{J}^{-1}\epsilon_I J \tag{26}$$

and ∇_ξ and Δ_ξ are backward and forward differences, respectively. Λ_A^+ contains all the positive eigenvalues and Λ_A^- contains all the negative eigenvalues, of the diagonal matrix Λ_A. For numerical stability, the positive-moving characteristics (eigenvalues) are backward differenced, and the negative-moving characteristics are forward differenced. Two-point, first-order accurate differencing is used for the backward and forward differences. They are, respectively,

$$\begin{aligned} \nabla_\xi \Lambda_A^+ &= \Lambda_{A_j}^+ - \Lambda_{A_{j-1}}^+ \\ \Delta_\xi \Lambda_A^- &= \Lambda_{A_{j+1}}^- - \Lambda_{A_j}^- \end{aligned} \tag{27}$$

where the subscripts '$j-1$', 'j', and '$j+1$' are the grid point indices in the ξ-direction. The inverse of the Jacobian $\mathcal{J}^{-1}$ found in Eq. 26 is evaluated at the central point 'j'.

Substituting Eq. 27 into Eq. 25 and re-arranging terms, the ξ-direction operator

becomes

$$= T_\xi \left[\underbrace{-i_b \Lambda^+_{A_{j-1}}}_{L_A} + \underbrace{I + i_b \left(\Lambda^+_{A_j} - \Lambda^-_{A_j}\right)}_{D_A} + \underbrace{i_b \Lambda^-_{A_{j+1}}}_{U_A} \right] T_\xi^{-1} \tag{28}$$

$$= T_\xi \left[L_A + D_A + U_A\right] T_\xi^{-1}$$

where L_A, D_A, and U_A are lower bidiagonal, diagonal, and upper bidiagonal matrices, respectively.

Diagonally dominant factorization, first suggested by Lombard et al. [51], yields

$$L_A + D_A + U_A = \left(L_A + D_A\right) D_A^{-1} \left(D_A + U_A\right) + O\left(h^2\right) \tag{29}$$

The second-order error, that results from the above factorization, is consistent with the previous approximations. Equation 29 can be shown to be true by examining Eqs. 26 and 28 and noting that L_A and U_A are of order h, and D_A is of order 1.

Finally, the ξ-direction ADI operator becomes:

$$T_\xi \underbrace{\left[L_A + D_A\right]}_{\textit{lower bidiagonal}} \underbrace{\left[D_A^{-1}\left(D_A + U_A\right)\right]}_{\textit{upper bidiagonal}} T_\xi^{-1}$$

$$= T_\xi \left[I + i_b \left(\nabla_\xi \Lambda^+_A - \Lambda^-_{A_j}\right)\right] \left[I + i_b\, h\, |\Lambda_A|\right]^{-1} \left[I + i_b \left(\Delta_\xi \Lambda^-_A + \Lambda^+_{A_j}\right)\right] T_\xi^{-1} \tag{30}$$

A similar procedure is followed for the η- and ζ- directions. The matrix inversion for each direction has been reduced to a product of a lower and an upper scalar bidiagonal matrix. It is implemented by performing a forward sweep followed by a backward sweep.

The viscous flux Jacobian matrix M is not simultaneously diagonalizable with the flux Jacobian C [43]. The ζ-direction operator of Eq. 21, therefore, must be modified. To retain the diagonalization in all three directions (and not incur the computation penalties associated with not simplifying the block tridiagonal operator in the ζ-direction), the viscous flux Jacobian M is simply neglected. Neglecting the matrix M does not affect the converged steady-state solution ($\Delta\hat{Q}^n \rightarrow 0$) because the right hand side of Eq. 21 remains unchanged. For the diagonalized Beam-Warming Method without flux vector splitting, Pulliam [47] found that neglecting the viscous

flux Jacobian M did not affect the stability or convergence rates for steady-state solutions, when compared to a method where the viscous flux Jacobian was retained in an additional implicit factor on the left hand side of Eq. 21. Pulliam and Steger [52] also verified this method for 2-D steady viscous flows and convecton dominated unsteady flows. Guruswamy [49] computed the three-dimensional unsteady viscous flow about a semi-infinite wing undergoing pitch oscillations, using the diagonalized Beam-Warming method. His results compared well with measured data. Obayashi and Guruswamy [53] computed the unsteady shock-vortex interaction on a flexible delta wing. They used the LU-ADI solution algorithm similar to that described previously. Instead of employing central differences and explicit artificial dissipation, however, they used upwinding to compute the inviscid fluxes. The numerical results showed fairly good agreement with experimental data for this difficult test case. The above examples, then, serve to validate the basic flow algorithm employed in this current work, for application to unsteady viscous flows. One can confidently expect the method to be capable of computing the unsteadiness of the tilt rotor flowfield — in particular, the vortex shedding from the wing leading and trailing edges.

Fujii and Obayashi [29] found that to ensure adequate stability of the thin-layer viscous terms when using the split flux vector approach, it was required to add a small amount of additional dissipation to the split diagonal matrices $\Lambda_C^{\pm}$ as shown below.

$$\Lambda_C^{\pm} = \frac{h}{2}\left(\Lambda_C \pm |\Lambda_C|\right) \pm \mathcal{J}^{-1}\epsilon_I J \pm \nu I \tag{31}$$

where

$$\nu = \frac{2\,\mu\left(\zeta_x^2 + \zeta_y^2 + \zeta_z^2\right)}{Re\,\rho\,\Delta\zeta}$$

where, in the computational domain, $\Delta\xi = \Delta\eta = \Delta\zeta = 1$.

Finally, the present scheme can be summarized as follows,

$$\begin{aligned} &T_\xi\left(L_A + D_A\right) D_A^{-1}\left(D_A + U_A\right) T_\xi^{-1} T_\eta \left(L_B + D_B\right) D_B^{-1}\left(D_B + U_B\right) T_\eta^{-1} T_\zeta \\ &\left(L_C + D_C\right) D_C^{-1}\left(D_C + U_C\right) T_\zeta^{-1}\,\Delta\hat{Q}^n \\ &\qquad = -i_b\, h\left[\delta_\xi \hat{E}^n + \delta_\eta \hat{F}^n + \delta_\zeta \hat{G}^n - \frac{1}{Re}\delta_\zeta \hat{G}_v^n\right] \\ &\qquad\quad -i_b\left[D_E|_\xi + D_E|_\eta + D_E|_\zeta\right]\hat{Q}^n \end{aligned} \tag{32}$$

Analytical expressions for $T_\xi^{-1}T_\eta$ and $T_\eta^{-1}T_\zeta$ and their inverses (see Ref. [46]) can be used to reduce the computational effort.

It is evident from the above equation that the inversion process has been reduced to one forward scalar sweep and one backward scalar sweep in each direction, and simple matrix multiplications.

This section has outlined the features of the LU-ADI algorithm developed by Fujii, Obayashi, and Kuwahara [28,29,30]. Also described is the implementation of the solution blanking feature within the basic LU-ADI numerical scheme. The algorithm, in its current form, provides an effective means of specifying flow parameters to model flowfield discontinuities in the interior of the computational domain. As is discussed in more detail in Chapter 4, the influence of the rotor and of the tangential wall jet are modeled using this approach.

2.5 Artificial Dissipation

A linear, constant coefficient Fourier stability analysis (assumes periodic boundary conditions) for the three-dimensional hyperbolic wave equation shows a mild, unconditional instability for the Beam-Warming factored algorithm [47]. Artificial dissipation (also called "smoothing"), both explicit and implicit, is required to render the scheme stable. The amount required is small relative to the physical, viscous dissipation. In the current implementation of the solution algorithm, second-order smoothing in the form of two one-sided differences is incorporated in each left hand side operator as shown in the previous section (see Eqs. 25 and 26). Implicit artificial dissipation serves to increase the stability bound imposed by the explicit artificial dissipation, and to enhance convergence.

The most common procedure for the explicit, right hand side of Eq. 21 is to add fourth-order artificial dissipation. This is required to dampen high-frequency growth thereby controlling nonlinear instability [43]. Employing only fourth-order dissipation, however, can produce non-physical oscillations near shocks [47] or at other discontinuities that may occur in the flowfield, such as at the edge of the rotor slipstream or across the rotor in computations of the tilt rotor flowfield. The

increased damping offered by second-order dissipation can be exploited to eliminate the overshooting and undershooting at flow discontinuities. Second-order smoothing, however, if applied everywhere, introduces excessive dissipation. For the right hand side of the equation, therefore, a nonlinear combination of fourth-order and second-order smoothing is employed. The dissipation model proposed by Obayashi, Fujii, and Gavali [54] is used here. The smoothing is treated similarly in each coordinate direction. As an example, the ξ-direction smoothing term of Eq. 21 is given by

$$D_E|_\xi \hat{Q}^n = \nabla_\xi \left\{ \left(I - \Phi_{j+\frac{1}{2}}\right) \left(\frac{\epsilon_E}{J}\right)_{j+\frac{1}{2}} \Delta_\xi J\hat{Q}^n - \Phi_{j+\frac{1}{2}} \nabla_\xi \Delta_\xi \left[\left(\frac{\epsilon_E}{J}\right)_{j+\frac{1}{2}} \Delta_\xi J\hat{Q}^n \right] \right\} \quad (33)$$

where

$$\begin{aligned} \Phi &= \text{matrix containing the flux limiter functions} \\ \epsilon_E &= K_E\, h\, \sigma_A \\ K_E &= \text{input constant} \\ \sigma_A &= \text{spectral radius of flux Jacobian matrix A} \\ &= |U| + a\sqrt{\xi_x^2 + \xi_y^2 + \xi_z^2} \end{aligned}$$

All parameters evaluated at $j + \frac{1}{2}$ are simply arithmetic averages of the values at j and $j + 1$. The matrix Φ is made up of elements whose values depend on the local flow gradients. For a relatively smooth variation of local flow properties, the corresponding element of Φ would take on a value near one so that only fourth-order dissipation would be used. Conversely, for large flow gradients, the element of Φ would be near zero thereby allowing the second-order terms to dominate. For further details about this explicit smoothing and for definition of the elements of the matrix Φ, see Ref. [54]. Note that the constants K_I (see Eq. 24) and K_E, the user-specified inputs for the implicit and the explicit dissipation, respectively, are selected to have the minimum values commensurate with obtaining consistently stable solutions.

2.6 Additional Features

The numerical computation of the flux derivatives and transformation metrics using central differences for 3-D problems introduces small errors due to violation of flow conservation. Typically, freestream values of the fluxes are subtracted from the

governing equations to achieve perfect freestream capture [43]. In the present hover computation, however, where the flow at the far-field boundary is non-uniform and near zero, an approach suggested by Vinokur [37] and implemented for plume flows with non-uniform freestream by Obayashi [55] is more appropriate. By computing the metrics and Jacobian using a finite volume approach over a distance of two grid cell widths in each direction, and by evaluating the flux derivatives using second-order accurate central differencing, freestream preservation is ensured. That is why a second-order accurate differencing is selected for the central difference operator on the right hand side of Eq. 32. To ensure freestream preservation, then, for the current application of a tilt rotor in hover, the method is limited to second-order spatial accuracy. In order to regain solution accuracies comparable to those obtainable with the original Fujii and Obayashi method [29,30], which employed fourth-order accurate central differences for the inviscid terms together with freestream subtraction, a greater number of grid points is required, particularly in the regions of large flow gradients.

To further enhance convergence speeds for steady-state calculations, Fujii and Obayashi incorporated a space-varying time step size h. This modification can be very effective for grids that have a wide variation in grid spacing. By scaling h with grid spacing, a more uniform local Courant number (ratio of local time step to grid cell width multiplied by the characteristic velocity) can be maintained throughout the flowfield. Since the local transformation Jacobian J scales with the inverse of grid cell volume, the following has been found to work well (refer to Ref. [52]):

$$h = \frac{h|_{ref}}{1 + \sqrt{J}}$$

where $h|_{ref}$ is a fixed, user-specified time step. This option is employed for the rotor alone computations (discussed in Chapter 5) because of the steady nature of the solution obtained using the actuator disk model for the rotor.

The numerical method was extended in the current work to incorporate several other features. The capability to model two-dimensional flows was added, as described in Chapter 4. This proved useful in developing new grids and boundary conditions. Although not used in the current tilt rotor model, a multiple zone capability,

scalar tridiagonal inversion in all three coordinate directions, implicit treatment of the ξ-direction periodic boundary condition using a periodic scalar tridiagonal inversion algorithm, and constant coefficient explicit smoothing were all implemented. Some of these additional features may be useful in future applications of the computer code.

Chapter 3

Grid Generation

3.1 General Comments

Grid generation is a very important aspect of computational fluid dynamics. The grid is the assembly of points at which the numerical solution to the relevant partial differential equations is found. To maintain solution accuracy, the grid should possess a smooth distribution of points (see Ref. [56]). Also, the distribution of points in the grid (or mesh) must be compatible with the fluid dynamics equations being solved and the particular flowfield.

As discussed in Section 2.2, the thin-layer approximation is made so as to limit the computational requirements to a manageable level. The viscous fluxes normal to the surface are dominant. In order to resolve this important contribution, the grid spacing must be very fine near, and in a direction normal to, the surface. Grid spacing can be much coarser along the surface where the far less significant tangential viscous fluxes need not be resolved. In addition, grid points must be clustered in regions where relatively large flow gradients are anticipated.

For the tilt rotor computation, three-dimensional grids are generated by stacking vertical, parallel, two-dimensional grids at spanwise locations along the wing and beyond the wing tip. A Poisson equation solver [57] is used to create each of the smoothed 2-D grids, clustering the points near the airfoil and the rotor. O-grids

are selected (over C-grids and H-grids) as they completely encircle the airfoil cross-section. They offer the most desirable grid point distribution for this type of flowfield where large flow gradients occur around both the leading and the trailing edge.

For the wing/rotor interaction computations, a grid with a flat region in the plane of the rotor is desired so as to enable an easier and more accurate implementation of the boundary conditions that correspond to the rotor. Figure 5 shows two views of a typical 2-D grid at a spanwise station inboard of the wing tip. Although only one zone, the smoothing for each 2-D grid is actually carried out independently on two separate meshes to obtain the desired grid spacing in the location of the rotor: (1) an inner grid whose inner boundary is the airfoil surface and whose outer boundary is the circumferential grid line containing the flattened upper portion used to define the rotor location, and (2) an outer grid enveloping the first grid and extending to a circular outer boundary 15 wing chords from the airfoil.

The V-22 wing is of constant cross-section with a squared wing tip. The mesh is generated for a wing flap deflection of 67°. This flap angle was found to be near-optimum for minimum download in flight tests of the XV-15 tilt rotor aircraft [4]. This angle is selected also because considerable experimental data exists from 0.658-scale model tests of the V-22 wing/rotor at this flap deflection (see Refs. [9,10]). To minimize discontinuities in the 3-D grid, the wing cross-section is gradually reduced to a point on the outer 3% of the wing semi-span. This gives rise to a singular line outboard of the wing tip. This and other features of the grid can be better appreciated in Fig. 6, a perspective, cutaway view of portions of the 3-D grid. The vertical grid plane in the foreground is the plane of symmetry. To facilitate the specification of the symmetry boundary conditions (see Section 4.2), the mesh actually extends one grid plane inboard of the plane of symmetry. The outer edge of the rotor disk is superimposed on the grid to help visualize the position of the rotor with respect to the wing. The rotor lies in a plane that is about one wing chord above the wing. Figure 7 is a cutaway view showing the outer boundaries of the grid. More details of the grid are presented in Section 3.3.

Implicit in the use of a plane of symmetry is the assumption that the flowfields on either side of the vertical centerline-plane are a mirror image of each other. Although

the computational effort is greatly reduced relative to analyzing both halves of the tilt rotor configuration, it is important to note that the plane of symmetry, for this current computational problem, only approximates the actual flowfield. As mentioned in Chapter 1, the flowfield generated by the rotors is unsteady and highly complex. Although the actual rotors are physically cross-coupled (i.e. interconnected in the event of a power failure in one engine), finite tolerances in the mechanical system result in slight variations in rotor blade position and pitch angle between the two rotors. Also, blade flexibility and the impossibility of manufacturing identical rotor sets, ensure that the rotor flowfields generated by each rotor are not identical. In addition, slight differences in the manufactured wing affect the vortex shedding at the wing leading and trailing edge. It is highly unlikely, then, that the separated flowfields, also influenced by non-identical rotor flows, are perfectly symmetric about the vehicle centerline. The local, instantaneous differences between the flowfields on either side of the vehicle center may or may not be significant. It is difficult to assess the validity of the symmetry assumption. It is assumed in this study, however, that the time-averaged effects of the actual flow assymetries are negligibly small. In any case, the current approach of time-averaging the unsteady effects of the rotor onto an actuator disk (see Chapter 4), is probably a greater limitation of the current tilt rotor model than the plane of symmetry. The plane of symmetry used in the numerical computations, however, is definitely more appropriate than the image plane used in the experimental studies (refer to Ref. [2], for example). The image plane provides a plane of symmetry of only finite dimensions. Additionally, it has the undesired effect of providing a surface for viscous effects, in the form of boundary layer growth, to be introduced. This may affect the flowfield; in particular, the recirculation fountain. The actual flow at the vehicle centerline may experience some vorticity generation due to assymetries in the flowfield. The shear stresses due to the interaction of free flows, however, would be different from those produced in the boundary layers which develop on an image plane.

To obtain the desired clustering of 2-D grid planes along the wing and beyond the wing tip, an exponential type of stretching is employed. If a distribution of N points is desired along a curve of specified length S, and the arc length between the first two

points is specified to be ΔS, then an expression for the total length can be written as (refer to Fig. 8) :

$$\begin{aligned} S &= \Delta S + \alpha\Delta S + \alpha^2\Delta S + \alpha^3\Delta S + \cdots \\ &= \Delta S \sum_{k=0}^{N-2} \alpha^k \end{aligned}$$

Defining a function f where

$$f = S - \Delta S \sum_{k=0}^{N-2} \alpha^k$$

then an iterative root finding procedure (Newton-Raphson method) is used to determine the value of α that satisfies $f = 0$ within a desired tolerance. This stretching function can easily be extended to a distribution of points with exponential stretching in both directions, i.e. a different ΔS is specified at both ends of the interval.

To generate a mesh for a 2-D calculation, three identical 2-D grids are stacked parallel to each other. This is required because the Navier-Stokes code employs a second-order accurate 3-point spatial numerical differencing. The computational results are then referred to as "pseudo 2-D" as they are essentially 2-D in character although they are generated by a 3-D method. This is made possible by proper application of symmetry boundary conditions at both ends of the mesh (refer to Section 4.2). Considerable use was made of this pseudo 2-D capability in the development of the grids and rotor model.

3.2 Elliptic Grid Generation

To ensure smooth grid point distributions on the interior of a 2-D mesh, an elliptic grid solver is employed. The elliptic grid generation scheme was first proposed by Thompson, Thames, et al. in Refs. [58,59]. It requires specification of grid point locations along the boundary — in this case, both the inner boundary (airfoil surface) and the outer boundary. The solution algorithm is outlined below.

The Poisson equations are used to generate a boundary-fitted, curvilinear 2-D grid:

$$\begin{aligned} \xi_{xx} + \xi_{yy} &= P(\xi,\eta) \\ \eta_{xx} + \eta_{yy} &= Q(\xi,\eta) \end{aligned}$$

where (ξ, η) represent coordinates in the computational domain, (x, y) represent coordinates in the physical domain, and P and Q are source terms which control the grid point spacing in the mesh interior. The computational domain is rectangular and the grid points within it are evenly-spaced. To simplify the evaluation of the derivatives and to ease the specification of the boundary conditions, the above equations are transformed to, and solved in, the computational domain. To do this, the roles of the independent and dependent variables are interchanged, and the equations become

$$\begin{aligned} \alpha x_{\xi\xi} - 2\beta x_{\xi\eta} + \gamma x_{\eta\eta} &= -J^2 (P x_\xi + Q x_\eta) \\ \alpha y_{\xi\xi} - 2\beta y_{\xi\eta} + \gamma y_{\eta\eta} &= -J^2 (P y_\xi + Q y_\eta) \end{aligned} \tag{34}$$

where

$$\begin{aligned} \alpha &= x_\eta^2 + y_\eta^2 \\ \beta &= x_\xi x_\eta + y_\xi y_\eta \\ \gamma &= x_\xi^2 + y_\xi^2 \\ J &= x_\xi y_\eta - x_\eta y_\xi \end{aligned}$$

All derivatives are approximated using standard second-order accurate finite differences. The spatial increments $\Delta\xi$ and $\Delta\eta$ can, without any loss in generalization, be assumed to be constant everywhere and equal to 1. The grid point locations on the boundary must be specified, and an initial guess for the interior grid values must be made.

This method with $P = Q = 0$ provides no control over the grid point spacing near a boundary. The grid points tend to be pulled away from the surface by the Laplacian elliptic solver. Sorenson and Steger [57] developed a technique for defining P and Q such that the angle at which the $\xi = constant$ grid lines intersect the boundary, as well as the distance between the boundary and the first off-boundary grid point on these grid lines, can be specified. In this way, grids having a very fine grid spacing near surfaces (for viscous calculations) can be generated. Also, orthogonality of the grid at the boundaries can be specified, if desired.

Any number of standard relaxation schemes can be used to solve the system of two Poisson equations. Two different solution algorithms were tried during the course

of this work. The first, an alternating direction implicit (ADI) scheme, is constructed using approximate factorization to convert the solution process to two tridiagonal matrix inversions. The solution method is discussed in more detail in Ref. [60]. It worked well for cases where the airfoil surface had no discontinuities (except for the trailing edge). Convergence difficulties were experienced for configurations where the flap was deflected resulting in surface discontinuities at the flap/main foil junction both on the upper and the lower surface. These unresolved problems necessitated the use of an alternate method. Sorenson [61] developed a solver based on the SLOR (successive line over-relaxation) scheme. This method was found to produce converged solutions regardless of the flap angle.

3.3 Grid Details

To ensure proper resolution of the thin tangential jet for blowing calculations, a thin region of the grid surrounding the wing surface is defined algebraically. The first 7 points in this region are equi-spaced and extend along a grid line normal to the wing surface to a distance 0.002 of the wing chord (c). This corresponds to a typical blowing slot height used in previous experiments by Felker and Light [2]. The remaining 6 points are stretched exponentially along the normal to a distance $0.006c$ from the wing surface. Although the number of points prescribed in the thin region surrounding the airfoil is somewhat arbitrary, there is a sufficient number to ensure adequate resolution of the velocity profiles in the jet and in the boundary layer. The same grid is used regardless of whether blowing is applied or not. The grid orthogonality at the wing surface contributes to increased accuracy in defining the boundary conditions required for the Navier-Stokes solution. Also, it provides for an easier and more appropriate implementation of the tangential jet (for more details, see Chapter 4). The outer edge of this thin algebraically-defined region which surrounds the airfoil is defined as the inner boundary to the Poisson grid generator. Orthogonality of the grid lines at this inner boundary is specified in the definition of the P and Q source terms of the Poisson equations. Figure 9 shows a blow-up of

the grid in the region of the leading edge at a typical wing cross-section. The highlighted grid line corresponds to the outer edge of the algebraically-defined region and the inner boundary of the Poisson-smoothed grid.

To avoid problems associated with resolving the flow around the V-22's blunt trailing edge (0.32%c thick), the airfoil was extended to a point at the trailing edge and re-scaled to its original chord.

As previously mentioned, the V-22 wing has a constant cross-section with a squared wing tip. To minimize discontinuities in the grid, the wing cross-section is gradually reduced to a very small circle (having radius equal to $0.0003c$), over the outer 3% of the wing semi-span. Five parallel 2-D grid planes are used to define this tip region. Although this is insufficient to accurately resolve all the details of the flow around the tip, it is deemed adequate for the present study. Further grid development in this region should focus on modeling the presence of the nacelle which is neglected in the current work. Outboard of the wing tip, the singular line (actually an extremely slender cylinder of grid points) extends to the outer boundary in the spanwise direction. At each spanwise station outboard of the tip, the first thirteen $\eta = constant$ grid lines are defined to be concentric circles. This improves the accuracy of the specification of the boundary conditions on the singular line (see Chapter 4) contributing to greater solution stability.

Two horizontal layers of grid points are used to define the influence of the rotor (see Chapter 4). It was found by numerical experimentation that placing these two planes of points $0.01c$ apart yielded accurate and stable solutions.

Except where otherwise stated, the computations of wing/rotor interaction discussed in Chapter 5 are performed on a grid whose dimensions are 73x47x70. There are 73 points that define the airfoil cross-section in the ξ-direction. Forty-seven 2-D grid planes are stacked in the spanwise η-direction, 23 of which are on the wing. Seventy points stretch from the wing surface to the outer boundary in the ζ-direction. Forty-six of these points extend from the wing surface to the plane of the rotor. The grid extends to approximately 15 wing chords (over 3 rotor diameters) normal to the wing surface and beyond the wing tip.

A computer program has been developed to create the three-dimensional grid

described above. Changes in the number of grid points and in the grid spacing are easily made. Grids for wings with a different airfoil cross-section can be generated in a straight-forward manner. Different flap deflections can also be modeled simply by redefining the airfoil geometry.

Accurate modeling of the gap between the main foil and the flap is a difficult task and would require further development of the gridding program. In addition, it should be noted that modeling the geometry of the slot would increase considerably the number of grid points, perhaps exceeding the available computer memory limits. As mentioned in Chapter 1, the fuselage, tail, and nacelle of the V-22 are not modeled in this study. They are complicated geometries which must be modeled using multiple grid blocks. Although the Navier-Stokes code has been extended to multiple-zone applications, development of these complicated 3-D zonal grids ensuring smooth transition between blocks, is beyond the scope of this work.

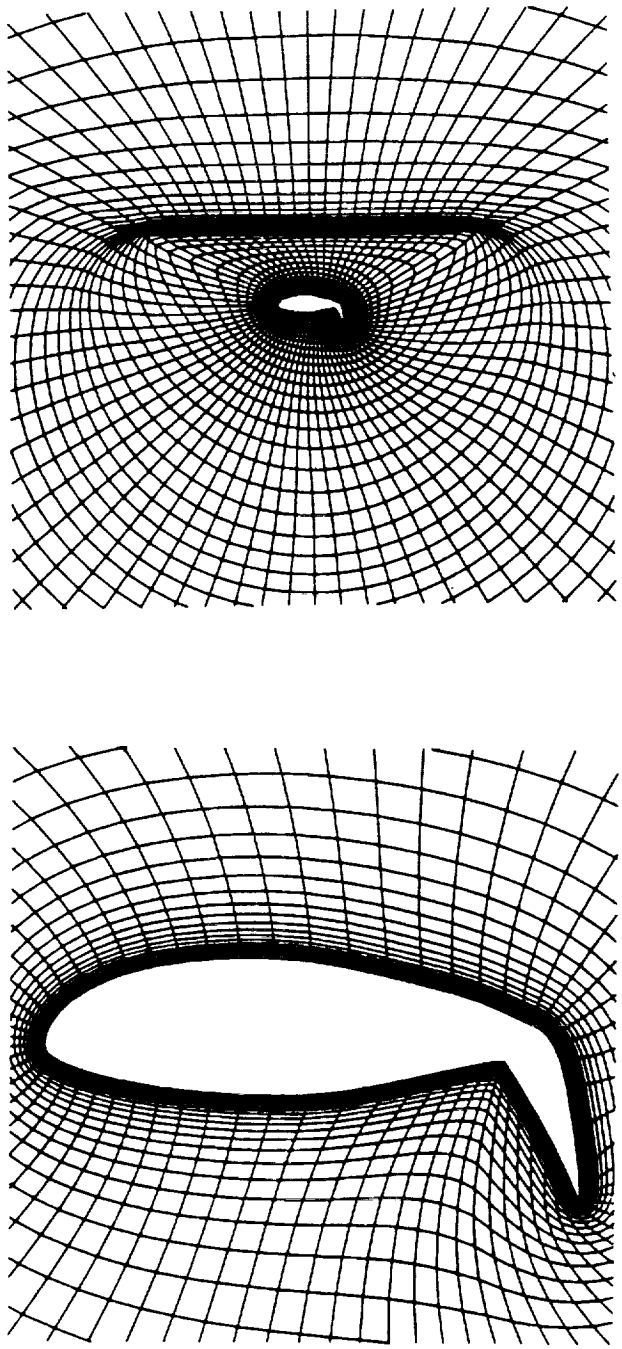

Figure 5: Cross-sectional cut through mesh showing the concentration of grid points around wing and rotor.

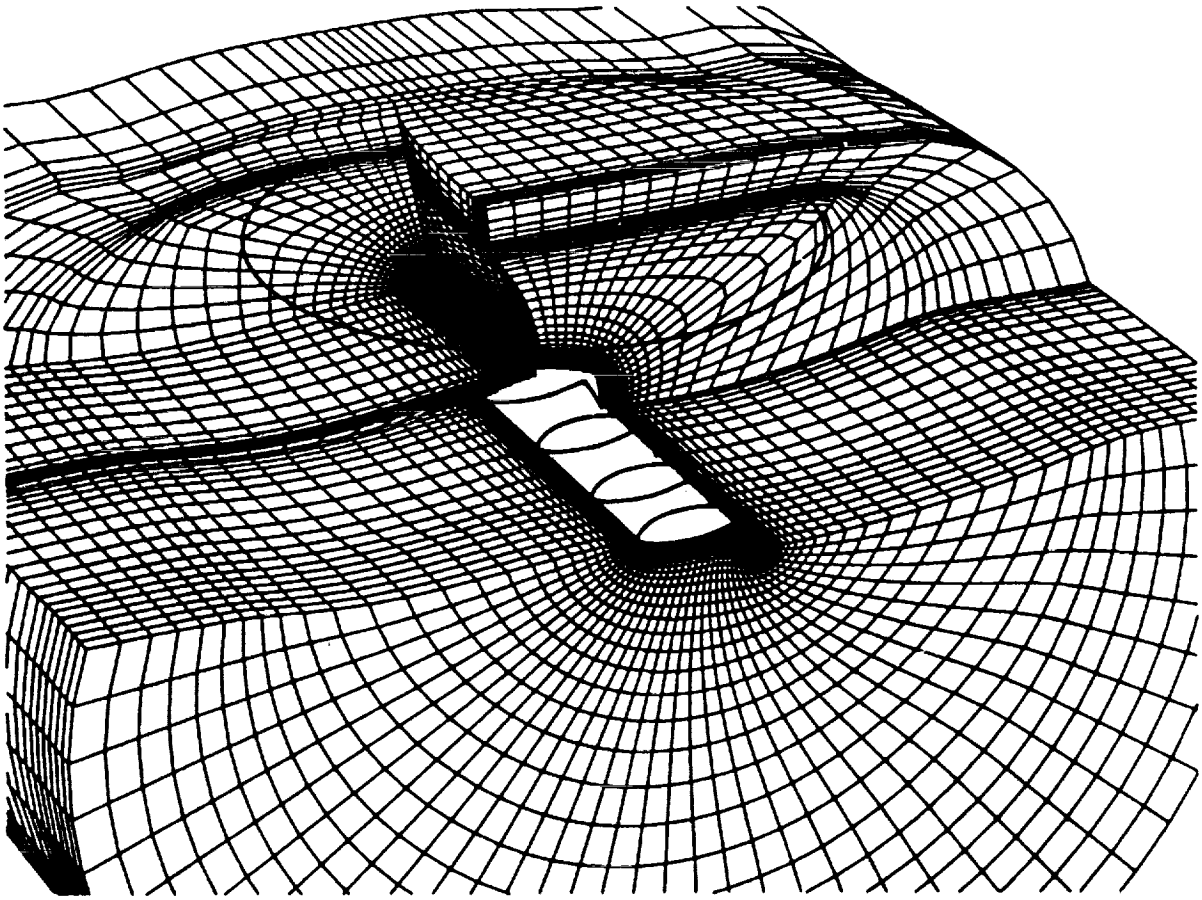

Figure 6: Cutaway view of mesh showing wing and rotor locations.

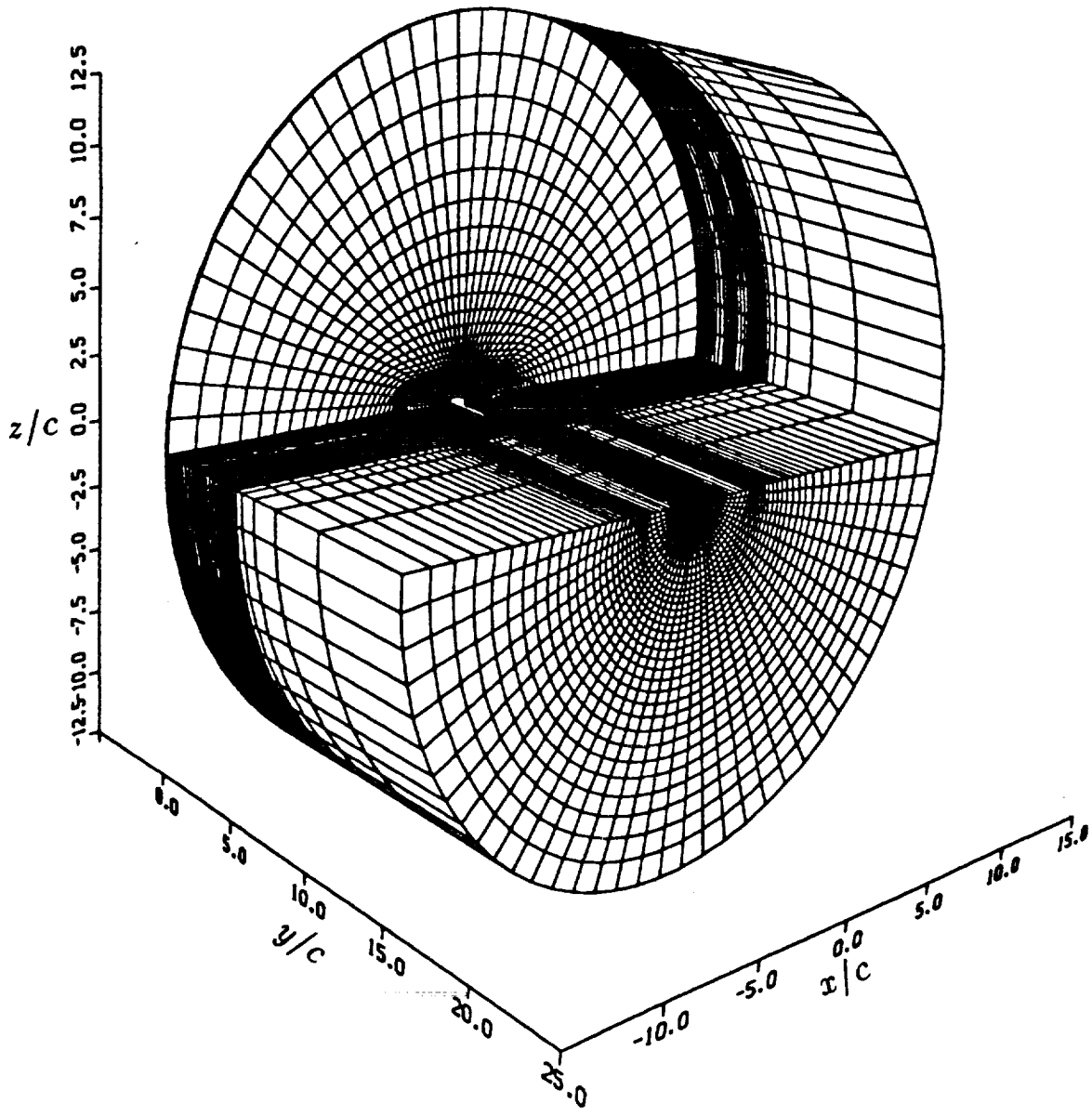

Figure 7: Cutaway view of mesh showing the outer boundaries of the grid.

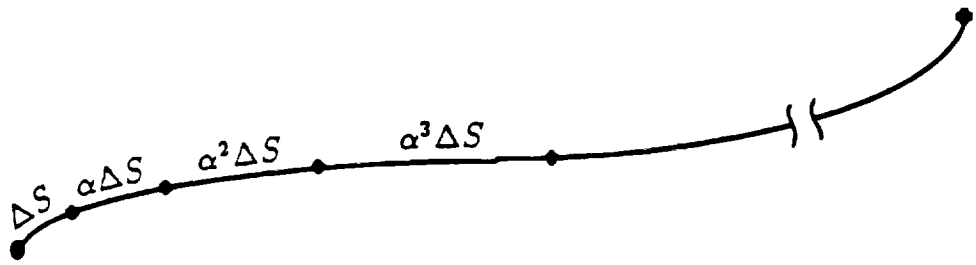

Figure 8: Exponential grid point stretching applied to an arbitrary curve.

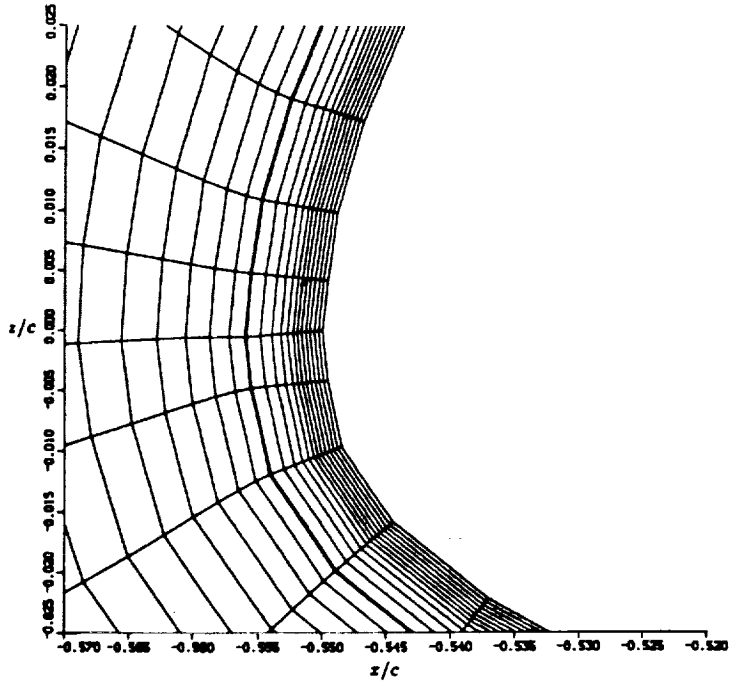

Figure 9: Blow-up of the grid in the region of the leading edge at a typical wing cross-section.

Chapter 4

Boundary Conditions

4.1 General Remarks

The finite difference solution of the Navier-Stokes equations requires specification of boundary conditions on all domain boundaries. In the numerical method employed in this study (described in Chapter 2), the boundary conditions are applied explicitly, i.e. the flow variables at the boundaries are evaluated using the most recent solution. This permits greater flexibility in applying the boundary conditions to a variety of geometries and flow situations. At all grid points located on the mesh boundaries, each of the five flow parameters that make up the vector of conserved quantities $\hat{Q}$ must be updated explicitly – either by specifying them or by extrapolating them from computed interior values. Referring then to the definition of $\hat{Q}$ in Section 2.2, the density ρ, the mass fluxes from the three momentum equations ρu, ρv, and ρw, and the total energy per unit volume e must all be updated at each time step.

Determination of the boundary conditions representative of a lifting rotor require a separate analysis and will be discussed in a later section. First, those boundary conditions not pertaining to the rotor will be described.

4.2 Non-Rotor Boundary Conditions

At grid points on the wing surface, for viscous (Navier-Stokes) calculations the no-slip boundary condition is imposed, i.e. all components of velocity are set to zero ($u = v = w = 0$). Inviscid computations can also be performed using the present computer code by omitting all viscous terms, i.e. the $\hat{G}_v$ flux vector, and by applying the inviscid boundary condition on the wing — zero normal velocity. In the computational domain, this condition is easily satisfied by setting the contravariant velocity component normal to the surface, W, to zero.

The pressures on the wing surface are found by solving the normal momentum equation (refer to [56,62]). The normal momentum equation is derived by taking the dot product of the vector comprised of the transformed x-, y-, and z-momentum equations, and the unit normal vector, $\vec{n}$. The viscous effects on the pressure at the surface are assumed to be insignificant and are neglected (typical boundary layer assumption).

$$\left[x\text{–}mom\,\vec{i} + y\text{–}mom\,\vec{j} + z\text{–}mom\,\vec{k} \right] \cdot \vec{n} \;=\; normal\ momentum \tag{35}$$

where

$$\vec{n} = \frac{\nabla\vec{\zeta}}{\left|\nabla\vec{\zeta}\right|} = \frac{\zeta_x\vec{i} + \zeta_y\vec{j} + \zeta_z\vec{k}}{\sqrt{\zeta_x^2 + \zeta_y^2 + \zeta_z^2}}$$

From the momentum equations, it can be seen that the normal momentum equation, at the body surface reduces to $\partial p/\partial n = p_n = 0$. Performing the above operations,

$$\begin{aligned} p_\xi\left(\xi_x\zeta_x + \xi_y\zeta_y + \xi_z\zeta_z\right) + p_\eta\left(\eta_x\zeta_x + \eta_y\zeta_y + \eta_z\zeta_z\right) + p_\zeta\left(\zeta_x^2 + \zeta_y^2 + \zeta_z^2\right) & \\ + \;\; \rho U\left(\zeta_x u_\xi + \zeta_y v_\xi + \zeta_z w_\xi\right) + \rho V\left(\zeta_x u_\eta + \zeta_y v_\eta + \zeta_z w_\eta\right) & \\ = \;\; p_n\sqrt{\zeta_x^2 + \zeta_y^2 + \zeta_z^2} \;\; = \;\; 0 & \end{aligned} \tag{36}$$

Evaluating the above expression at the surface, U and V are zero for viscous flow calculations, p_ζ can be approximated by second-order one-sided differences, and p_ξ and p_η are expressed as second-order central differences. Re-arranging the equation, and applying approximate factorization, results in an implicit solution algorithm for p at the surface which involves two one-dimensional tridiagonal inversions — one in

the ξ-direction and the other in the η-direction. Obtaining surface pressures using the above method yields a more accurate and stable solution method than simply using zero-order extrapolation.

Assuming adiabatic conditions at the surface (no heat flux, i.e. $\partial T/\partial n = 0$), and noting from above that $\partial p/\partial n = 0$, then, from the equation of state for an ideal gas ($p = \rho RT$), the density gradient normal to the surface is also zero. The density at the surface, then, is obtained by a zero-order extrapolation from the value at the nearest off-body point normal to the wall. The final quantity required, the total energy per unit volume e, is calculated from Eq. 9 using the previously-defined quantities.

Beyond the wing tip, where the airfoil cross-section collapses to a circle with very small diameter (0.0003 of a wing chord), the values of $\hat{Q}$ on the singular line are determined by averaging the flow properties computed at the grid locations adjacent to and surrounding the singular line. Outboard of the wing tip then, for each element q of the $\hat{Q}$ vector, and for all j from 1 to $JMAX$ (the maximum value of j), at $l = 1$,

$$q_{j,l=1} = \frac{\sum_{j=1}^{JMAX} q_{j,l=2}}{JMAX} \tag{37}$$

where j is the index in the ξ-coordinate direction and l is the index in the ζ-direction.

As discussed previously in Chapter 3, symmetry of the tilt rotor flowfield in hover is assumed. Therefore, to reduce the computational effort, only one-half of the tilt rotor configuration is modeled. Two parallel 2-D grid planes located at spanwise indices $k = 1$ and $k = 3$ straddle (and are equi-distant from) the plane of symmetry at $k = 2$. The grid points in plane $k = 3$ are mirrored about the plane of symmetry to define the following symmetry boundary conditions at $k = 1$:

$$\begin{aligned} \rho_1 &= \rho_3 \\ (\rho u)_1 &= (\rho u)_3 \\ (\rho v)_1 &= -(\rho v)_3 \\ (\rho w)_1 &= (\rho w)_3 \\ e_1 &= e_3 \end{aligned} \tag{38}$$

This ensures that, at the centerline, the gradients (normal to the plane of symmetry)

of temperature and pressure are zero. The normal gradient of the velocity components that are tangential to the plane of symmetry (u and w) is zero. The spanwise component of velocity v is also effectively zero at $k = 2$.

The 3-D Navier-Stokes computer code was extended to allow "pseudo 2-D" computations, i.e. computations of 2-D flowfields using the 3-D solver. This was found useful for developing new grids and boundary conditions. Because three-point second-order spatial differencing is used on the right hand side of Eq. 32, at least three parallel and identical 2-D grids are required. For "pseudo 2-D" calculations, then, symmetry boundary conditions are applied at grid planes $k = 1$ and $k = 3$ using the solution at grid plane $k = 2$, in a manner similar to Eq. 38. This ensures that the code effectively sees an infinitely long wing having constant airfoil section.

The grid points of each two-dimensional O-grid line in the j-direction wrap around the airfoil, and the first and last points are coincident at the trailing edge. This creates a periodic boundary which extends from the airfoil trailing edge to the outer boundary. The $j = 1$ and the $j = JMAX$ boundaries are therefore coincident. In the computational domain, however, they are at opposite ends and are coupled by the following periodic boundary condition:

$$\begin{aligned} q_1 &= \frac{1}{2}(q_2 + q_{JMAX-1}) \\ q_{JMAX} &= \frac{1}{2}(q_2 + q_{JMAX-1}) \end{aligned} \tag{39}$$

The periodic boundary conditions are simply taken to be the average of the flow properties on both sides of the boundary.

On all the outer boundaries of the computational domain (about 15 wing chords from the wing surface, for the computations performed here), either inflow or outflow boundary conditions are specified. The flow is essentially inviscid in these far-field regions. The Euler equations are hyperbolic partial differential equations. Applying a method of characteristics analysis to hyperbolic PDE's helps to determine the appropriate boundary conditions for inflow and outflow boundaries. For subsonic flow in three dimensions, four of the characteristic velocities are positive and the fifth one is negative. For a subsonic inflow boundary, then, four independent thermodynamic and kinematic flow properties should be specified, and one should be extrapolated

from the interior of the flow domain. For a subsonic outflow boundary, on the other hand, only one property should be specified and four extrapolated. For typical computational fluid dynamic applications, where the freestream flow is non-zero, inflow boundary conditions are applied at those grid points on the outer boundary that are upstream of the wing. Freestream Mach number, the flow angles, and the pressure are commonly specified and the density is extrapolated from the interior of the computational domain. The outflow boundary is defined at those points on the outer boundary which lie downstream of the wing. In the tilt rotor hover case, however, where the flowfield is being driven solely by the rotor situated near the center of the computational domain, it was found that treating the entire outer boundary as an outflow boundary gives the best results. The only constraint imposed on the outer flowfield, then, is the static pressure which is set to its freestream ambient value. All other flow properties at the outer boundary are obtained by zero-order extrapolation.

4.3 Rotor Model

4.3.1 Approach

As discussed in Chapter 1, detailed modeling of individual rotor blades and the discrete vorticity shed into the wake behind each blade, using the latest CFD techniques, is a formidable task requiring computer resources that push the currently-available technology. The problem is further compounded by the necessity, in this current research effort, to also accurately model the detailed flow about the wing. The focus of this current work is the computation of wing download and not the detailed calculation of the local flow around each of the rotor blades. The problem then is rendered more tractable by employing a simpler model for the rotor. The rotor is assumed to be an actuator disk, i.e. the blade loads are time- and space-averaged over elemental areas that comprise the entire rotor disk. In the past, as mentioned in Section 1.2.2, Clark [13] and Lee [14] employed actuator disk models in their panel method computations of a tilt rotor in hover. Their rotor models produced results that were representative of the actual overall flowfield features. The actuator disk

approach to modeling the rotor neglects the unsteadiness of the rotor flow and the influence of the shed vorticity on the rotor blades and on the wing. The impact of these simplifications is difficult to assess. It is expected, however, that the rotor's time-averaged influence on the wing should be predicted quite well.

Figure 10 is a view of those points of the computational grid that lie in the plane of the rotor. Superimposed on the figure is an outline of the wing and also the rotor disk which has been subdivided uniformly into a number of radial and azimuthal segments. At each elemental area on the rotor disk, an average of each of the flow properties (the density ρ and the velocity components u, v, and w) is determined from the most-recently computed solution at all points within the elemental area. Momentum theory/blade element analysis is then applied which yields updated flow properties. These are then specified at all grid points within the given area. This approach allows the incorporation of the effects of blade geometry, airfoil aerodynamic characteristics, blade twist and pitch angles, and rotor rotational speed, as described below. In this way, the influence of the rotor can be described by distributions of local pressure rise through the rotor and local swirl velocity. The method has similarities with that described in Ref. [26] where source terms, added to the incompressible Navier-Stokes equations, were evaluated using 2-D blade section characteristics, to compute the 3-D, time-averaged, rotor flow in forward flight. A discussion of the validation of the rotor model is presented in Section 5.2, where comparisons are made with simple momentum theory and experimental data for a rotor alone.

4.3.2 Combined Momentum Conservation/Blade Element Analysis

Glauert [63], McCormick [64], and Prouty [65] provide good discussions on momentum conservation and blade element analyses applied to propellers and/or rotors. These classical analyses assume that there is no slipstream contraction and that the flow through the rotor disk has no radial component. They generally allow only radial variations of torque and thrust. The momentum theory/blade element analysis

presented below, on the other hand, allows slipstream contraction. A radial component of flow is permitted although, for the purpose of evaluating the aerodynamic forces on the rotor blades, only the axial and tangential flow components are taken into account. Also, the method discussed below computes both azimuthal and radial variations of torque and thrust.

Relative flow angles and resultant aerodynamic forces acting on an elemental area of the rotor disk are shown in Fig. 11.

The swirl above the rotor disk is zero, and immediately downstream it jumps to V_t. Therefore, in the rotor plane, the swirl is assumed to be $V_t/2$ as shown in Fig. 11. The analysis has been generalized here to include ascending and descending flight (i.e. V_∞ and, therefore, the angle ϕ are non-zero). Each elemental area dA sweeps through an angle $d\psi$ and possesses a radial width dr (i.e. $dA = r\, d\psi\, dr$).

Calculation of Local Pressure Rise across the Rotor Disk

The elemental thrust dT acting on an elemental area dA of the rotor disk is equal to the total load, generated by all the blades, on an annulus of the rotor disk (situated a distance r from the axis of rotation), multiplied by the factor $d\psi/2\pi$ which represents the average time spent over each elemental area. This yields:

$$dT = B\frac{d\psi}{2\pi}\left(L\cos\left(\phi + \alpha_i\right) - D\sin\left(\phi + \alpha_i\right)\right) \tag{40}$$

where B is the number of blades, and L and D, respectively, are the aerodynamic lift and drag forces produced by a rotor blade segment of width dr. The angle α_i is the induced angle of incidence, and the angle ϕ (see Fig. 11) is zero for the hover case.

From the definition of the two-dimensional aerodynamic force coefficients C_l and C_d, the blade segment lift and drag, respectively, can be written as

$$\begin{aligned} L &= \frac{1}{2}\rho\, V_{eff}^2\, C_l\, c\, dr \\ D &= \frac{1}{2}\rho\, V_{eff}^2\, C_d\, c\, dr \end{aligned} \tag{41}$$

where V_{eff} is the effective local velocity in the plane normal to the rotor radius and c is the local blade chord.

Substituting Eq. 41 into Eq. 40,

$$dT = \frac{1}{2}\rho V_{eff}^2 B\, c \frac{d\psi}{2\pi} dr \left(C_l \cos(\phi + \alpha_i) - C_d \sin(\phi + \alpha_i)\right) \tag{42}$$

In the current implementation, the 2-D aerodynamic force coefficients are assumed to be functions of angle of incidence α and the Mach number M, i.e.

$$\begin{aligned} C_l &= f_1(\alpha, M) \\ C_d &= f_2(\alpha, M) \end{aligned} \tag{43}$$

They are determined from a look-up table comprised of actual Boeing wind tunnel test results for the four different airfoil sections that define the V-22 rotor blade (obtained from Boeing's C81 airfoil deck of XN-series airfoils).

Note that from Fig. 11, $\alpha = \beta + \theta - (\phi + \alpha_i)$ where θ is the local blade twist relative to that at the 75% span location, and β is the blade pitch angle setting. A simple iterative root finding scheme is employed at each time step to determine β for a desired thrust coefficient C_T. In other words, at each time step, the rotor blade pitch is trimmed to obtain the specified trim thrust coefficient. This procedure is outlined in a later section.

At each time step of the computation, the results from the most current Navier-Stokes solution are used to obtain the flow angles, velocity components, and the density at the rotor disk. In particular, the induced angle of incidence α_i, the effective velocity V_{eff}, and the density ρ are determined. As previously mentioned, local averages of the required flow properties are taken by summing the values of all the points within a given elemental area. The lift and drag coefficients associated with each elemental area are obtained using the table look-up, by inputting the computed average local angle of incidence and Mach number. The elemental thrust dT is then computed from Eq. 42. The local pressure rise across the rotor disk Δp, which is used as a boundary condition for the Navier-Stokes solution, is then easily obtained from

$$\Delta p = \frac{dT}{dA} \tag{44}$$

Calculation of Local Swirl Velocity at the Rotor Disk

Referring to Fig. 11, the elemental torque dQ acting on an elemental area dA is:

$$dQ = B\frac{d\psi}{2\pi}\left(L\sin\left(\phi+\alpha_i\right)+D\cos\left(\phi+\alpha_i\right)\right)r \tag{45}$$

Substituting Eq. 41 into Eq. 45,

$$dQ = \frac{1}{2}\rho\, V_{eff}^2\, B\; c\frac{d\psi}{2\pi}dr\left(C_l\sin\left(\phi+\alpha_i\right)+C_d\cos\left(\phi+\alpha_i\right)\right)r \tag{46}$$

Another expression for dQ can be derived by considering the conservation of angular momentum. The torque produced by an elemental area of the rotor disk on the fluid is equal to the rate of change of angular momentum (the mass flow multiplied by the net circumferential change in velocity multiplied by the moment arm r):

$$dQ = \underbrace{\rho\left(rd\psi dr\right)\left(V_a+V_\infty\right)}_{mass\ flow}\quad\underbrace{V_t}_{velocity\ change}\quad r \tag{47}$$

where V_a is the component of the local induced velocity normal to the rotor disk and, for hover, $V_\infty = 0$. Given dQ computed from Eq. 46, the tangential (or swirl) velocity V_t can be obtained from Eq. 47.

Now that the pressure rise Δp and swirl velocity V_t have been computed, they are applied as "interior boundary conditions" as described below.

Blanking Technique for Rotor

Because rotor thrust is a function not of absolute static pressures, but of the change in pressure Δp through the rotor disk, two adjacent horizontal layers of grid points are used to specify the desired flow conditions. The total effect of the rotor is assumed to take place between these two layers of rotor grid points. The two horizontal planes of grid points which lie closest to the plane of the actual rotor and which lie within the rotor radius are defined as rotor grid points. These points are blanked out of (excluded from) the implicit solution process, and their flow values updated explicitly. This is done by setting the blanking parameter i_b (see Chapter 2) to zero for all rotor grid points. For all other grid points in the computational domain, i_b is set to one. The lower and upper layers of rotor grid points (separated by a vertical distance of only

$0.01c$) are referred to, in the discussion below, as L and $L+1$, respectively. These two layers of points are seen superimposed on each other in Fig. 10.

An approach similar to that used in Ref. [66] is adopted here to define a consistent set of boundary conditions for the rotor. Consideration of the characteristic velocities of the flowfield indicates that for a subsonic inflow boundary, four flow properties must be specified and one can be extrapolated from the interior solution domain.

The rotor grid points of layer L are considered to be an inflow boundary. This means that the flow is viewed as moving from the region above, into the region below, the rotor. Ideally, the direction (flow angles) of the flow through the rotor would be specified from measured experimental data or, alternatively, from a complete Navier-Stokes solution of the rotor. In the absence of this information, which does not exist, the velocity components are specified as described below. The x-component of velocity is a combination of the u velocity at $L+1$ plus the component of swirl in the x-direction. Similarly, the y-component of velocity is a combination of the v velocity at $L+1$ plus the component of swirl in the y-direction. They are given below assuming a counterclockwise rotation of the rotor as seen from above (as for the V-22):

$$\begin{aligned} u|_L &= u|_{L+1} - V_t \sin\psi \\ v|_L &= v|_{L+1} + V_t \cos\psi \end{aligned} \tag{48}$$

The angle ψ is the angular location of a given rotor grid point with respect to a horizontal line extending aft from the rotor axis of rotation (see Fig. 10). The swirl velocity V_t is obtained from the analysis described previously.

The pressure at the L layer of rotor grid points (inflow boundary) is defined to be the pressure immediately above the rotor plus the rotor-induced pressure rise Δp computed in the previous analysis:

$$p|_L = p|_{L+1} + \Delta p \tag{49}$$

The final quantity to be specified is the density. Because of the low subsonic Mach number flow induced by the rotor in hover, the flow is essentially incompressible. The density can, therefore, be assumed to be freestream density with negligible error.

Alternatively, either the total temperature or the total pressure could be specified at the layer L of rotor grid points from which the density could be derived, as shown below.

In the absence of a Navier-Stokes solution about the individual blades which would yield the total temperature or total pressure immediately downstream of the rotor disk, experimental data must be utilized. Here it is assumed that the total pressure $p_o|_L$ produced by the rotor at each elemental area of the rotor disk acts at the inflow boundary L and is known. The rotor can be regarded as a compressor of very low pressure ratio. The definition of compressor efficiency η is used to relate the total temperature ratio across the rotor $T_o|_L \,/\, T_o|_{L+1}$ to the total pressure ratio across the rotor $p_o|_L \,/\, p_o|_{L+1}$ (see, for example, Oates [67]):

$$\frac{T_o|_L}{T_o|_{L+1}} = 1 + \frac{\left(\left(\frac{p_o|_L}{p_o|_{L+1}} \right)^{\frac{\gamma-1}{\gamma}} - 1 \right)}{\eta} \tag{50}$$

The total pressure and the total temperature immediately above the rotor $p_o|_{L+1}$ and $T_o|_{L+1}$, respectively, are assumed to be unchanged from their freestream ambient values. The local rotor efficiency η is estimated as described below. Equation 50 is used to compute the local total temperature immediately downstream of the rotor (at the inflow boundary L) $T_o|_L$.

Compressor efficiency is defined as the ideal work divided by the actual work, for a given pressure ratio [67]. If the efficiency were 100%, the compression process would be isentropic — i.e. there would be no losses due to viscous dissipation or shocks on the rotor blades. The previously-described blade element theory can be used to obtain an estimate of the local compressor efficiency. The aerodynamic efficiency in hover is the ratio of the ideal power to the actual power for a given thrust (see, for example, Stepniewski [68]). For a rotor having a constant rotational speed, this reduces to the ratio of torques, which is essentially equivalent to the definition of the compressor efficiency. The actual local torque on an elemental area of the rotor disk is given by Eq. 46. The ideal torque is the required torque where the losses are zero. The ideal process is an isentropic (inviscid, adiabatic) process. The 2-D drag coefficient C_d of Eq. 46 is comprised of all the non-isentropic contributions to drag, i.e. the viscous

effects and shocks. The ideal local torque, therefore, can be determined from Eq. 46 by simply setting C_d to zero. Taking the ratio of ideal to actual torque, the local compressor efficiency can be estimated by:

$$\eta = \frac{C_l \sin(\phi + \alpha_i)}{C_l \sin(\phi + \alpha_i) + C_d \cos(\phi + \alpha_i)} \tag{51}$$

Below the rotor, the flow can again be assumed to be isentropic. The isentropic flow relations (see any textbook on compressible fluid dynamics, for example, Ref. [35]) can then be used to compute the static temperature at the layer L of rotor grid points, using the total temperature computed from Eq. 50:

$$T|_L = T_o|_L \left(\frac{p_L}{p_o|_L} \right)^{\frac{\gamma-1}{\gamma}} \tag{52}$$

With $p|_L$ from Eq. 49 and $T|_L$ from Eq. 52, the density $\rho|_L$ is determined from the equation of state for an ideal gas:

$$\rho|_L = \frac{p|_L}{RT|_L} \tag{53}$$

In the current formulation, since experimental data was not available, the total pressure imparted by the rotor is assumed to be simply the sum of the static and dynamic pressures at rotor grid points L assuming a freestream value of density.

The final inflow boundary condition is not specified as the others, but, rather, is extrapolated. The mass flow normal to the rotor $\rho w|_L$ is updated by applying zero-order extrapolation using the computed flowfield values at $L - 1$:

$$\rho w|_L = \rho w|_{L-1} \tag{54}$$

The above inflow boundary conditions are computed at all rotor grid points of layer L using values of the flow parameters (at either $L+1$ or $L-1$) from the current (most recent) computation.

The row $L + 1$ of rotor grid points is considered to be an outflow boundary. In other words, the flow is viewed as exiting from the region above the rotor. For the outflow boundary conditions to be consistent, four flow properties are extrapolated and one is fixed. The density ρ, the mass fluxes ρu and ρv, and the total energy e are

updated using zero-order extrapolation from the solution at $L+2$. Mass continuity through the rotor disk is ensured by specifying

$$\rho w|_{L+1} = \rho w|_L \tag{55}$$

The swirl is imparted by the rotor to the flowfield downstream of the rotor disk. The rotational motion (swirl) upstream of the rotor is essentially zero. In early computations using the method described above, the computations showed significant swirl in the flowfield above (upstream of) the rotor. The rotor model, then, did not produce the expected behavior. This was attributed to the explicit artificial smoothing which, as formulated, was attempting to smooth out the flow discontinuities introduced by the rotor between the L and $L+1$ horizontal layers of rotor grid points. To eliminate this unwanted artificial dissipation, one-sided differencing, as opposed to the standard central differencing, is used when computing the smoothing at the $L+2$ grid points above the rotor and for the $L-1$ grid points below the rotor. This one-sided differencing is similar to that applied adjacent to the computational boundaries. This approach serves to isolate the calculation of the artificial smoothing from the flow discontinuities imposed by the rotor. It is very effective in eliminating the unwanted introduction of swirl above the rotor disk.

Calculation of Overall Rotor Performance

The total thrust and torque on the rotor disk are calculated by integrating the contributions from all elemental areas on the rotor disk. Eqs. 42 and 46 can be easily written in terms of $\partial^2 T/\partial r \partial \psi$ and $\partial^2 Q/\partial r \partial \psi$, respectively. Then

$$\begin{aligned} T_{TOT} &= \int_0^R \int_0^{2\pi} \left(\partial^2 T/\partial r \partial \psi\right)\, dr\, d\psi \\ Q_{TOT} &= \int_0^R \int_0^{2\pi} \left(\partial^2 Q/\partial r \partial \psi\right)\, dr\, d\psi \end{aligned} \tag{56}$$

where R is the rotor radius. The total rotor thrust coefficient and total rotor torque coefficient, in hover, are calculated using the standard definitions:

$$\begin{aligned} C_T &= \frac{T_{TOT}}{\rho A \left(\Omega R\right)^2} \\ C_Q &= \frac{Q_{TOT}}{\rho A \left(\Omega R\right)^2 R} \end{aligned} \tag{57}$$

where Ω is the rotor rotational speed, and A is the rotor disk area.

The figure of merit FM is a measure of hover efficiency. It is defined as the ratio of the minimum possible power (ideal induced power) required to hover to the actual power required to hover (induced power plus profile power) for a given thrust. It can be expressed in terms of the rotor thrust coefficient C_T and the rotor power coefficient C_P. Note that in hover, the power coefficient is equal to the torque coefficient, i.e. $C_P = C_Q$. The figure of merit, then, can be expressed as (see, for example, Johnson [18]):

$$FM = \frac{C_T^{3/2}/\sqrt{2}}{C_Q} \tag{58}$$

Except where otherwise noted, the rotor model assumes that the blades extend to the rotor centerline, and no account is taken of the rotor hub or its effect on the flowfield.

Iteration Procedure for Rotor

For a given rotor having specified blade geometry and for a given operating thrust coefficient C_T, an iterative solution procedure outlined below gives the local pressure rise and swirl velocity at each elemental area of the rotor disk, at a converged value of blade pitch angle setting β (also called collective). This procedure is performed at every time step of the Navier-Stokes solution. The starting solution for this iteration procedure is a previously-converged solution for a uniformly-loaded rotor operating at an equivalent thrust coefficient.

1. Input rotor RPM, and rotor geometry including:
   - number of blades
   - rotor radius
   - blade planform shape, i.e. local chord c distribution
   - blade twist relative to the 75% radial location, i.e. local θ distribution
2. Input 2-D airfoil characteristics: C_l, C_d as a function of α and M.

3. Extract the most recently computed values of the flow properties in the plane of the rotor; in particular, the flow angles and velocities.

4. Input desired total thrust coefficient C_{Tdes}.

5. Make a guess for the blade pitch angle β.

6. At each elemental area of the rotor disk, calculate Δp and V_t using the above information.

7. Integrate over the rotor disk to obtain C_T and C_Q.

8. If C_T is within a certain specified tolerance from the desired, user-specified value of thrust coefficient C_{Tdes}, then the solution is converged; otherwise, update the estimate of β by applying the false position method (refer, for example, to Ref. [69]) to find the root of the function $F = C_T - C_{Tdes}$. The new guess for the blade pitch angle β_{new} can be written as

$$\beta_{new} = \beta_{low} - \frac{F(\beta_{low})}{F(\beta_{old}) - F(\beta_{low})}(\beta_{old} - \beta_{low})$$

where β_{low} is a specified value of β known to be lower than the converged value, and β_{old} is the previous guess for the blade pitch angle. With β_{new}, go to step (6) and repeat steps (6) through (8).

4.4 Wall Jet

In previous CFD studies, Yeh [33] used multiple zones and Tavella et al. [70] used actuator planes to model a tangential, circulation-control jet on the surface of a wing. In the current approach, the blanking feature of the "chimera" scheme is employed to model the jet, in a manner similar to that used for the rotor. It is a new and effective technique and not restricted to application at zonal boundaries as are the previous methods.

To simplify grid generation, the spanwise step in the wing surface formed by the blowing slot is not resolved. As described below, the wall jet is imposed at a number

of grid points normal to the surface. Except for the local computed pressure, the jet is defined independently of the local flowfield. The jet, then, is assumed to dominate the local flowfield and to be unaffected by any upstream boundary layer development. A similar approach taken in Ref. [70], for tangential leading edge blowing on a delta wing, was found to give results that were of comparable accuracy to computations where the jet slot was fully resolved.

Refer to Fig. 12 during the following discussion. To model the jet, a selected number L_{jet} (seven are used here) of grid points along grid lines J and $J+1$, for all 2-D grid planes inboard of the wing tip, are defined at which the implicit solution is "blanked", or excluded. The solution is updated explicitly with the "internal boundary conditions" described below. The primary wall jet boundary conditions are specified at the L_{jet} points on grid line J and are considered to form an inflow boundary. The grid line immediately upstream, i.e. $J+1$, is considered to be an outflow boundary.

For the inflow boundary at J, the static pressure p at the jet slot exit is assumed constant across the width (0.2%c) of the jet and equal to the computed pressure immediately outside the jet slot, i.e. the pressure at $L_{jet}+1$ (see Fig. 12). The temperature at the jet exit is assumed to be freestream ambient. The density ρ can then be computed from the equation of state for a perfect gas. The total jet plenum supply pressure p_p is normalized by the freestream ambient pressure and is a user input. The Mach number at the jet exit is calculated assuming isentropic expansion of the compressed air from the plenum pressure p_p to the local static pressure p at the jet exit. Employing also the definition of the speed of sound, the jet exit velocity is given by (see any textbook on compressible fluid dynamics):

$$V_{jet} = \sqrt{\left(\left(\frac{p}{p_p}\right)^{\frac{-(\gamma-1)}{\gamma}} - 1\right)\frac{2\gamma}{\gamma-1}\frac{p}{\rho}} \tag{59}$$

The jet is assumed to be tangent to the airfoil surface at the jet exit.

At the outflow boundary at $J+1$, the pressure is fixed by applying the computed value of pressure just outside the slot region (i.e. the pressure at $L_{jet}+1$). First-order extrapolation, using the flow properties at $J+1$ and $J+2$, is employed to update

all the remaining required flow properties, i.e. density and the mass fluxes. If the points $J+1$ and $J+2$ are relatively far apart and the flow gradients large, first-order extrapolation may be unstable. In such cases, zero-order extrapolation is employed. Except where otherwise noted, however, first-order extrapolation has been employed.

Typically the blowing momentum coefficient C_μ is defined as the ratio of the jet momentum to the freestream momentum. In the current hover computation, however, where the freestream velocity is essentially zero, the freestream momentum is replaced by the momentum imparted by the rotor. Writing both the numerator and the denominator per unit length, the blowing momentum coefficient is defined here to be

$$C_\mu = \frac{\rho V_{jet}^2 h}{T/A\, c} \tag{60}$$

where V_{jet} is the jet exit velocity defined in Eq. 59, h is the slot height, T/A is the rotor thrust loading, and c is the wing chord. Applying the definition of the rotor thrust coefficient C_T from Eq. 57, the blowing momentum coefficient becomes

$$C_\mu = \frac{V_{jet}^2 h}{C_T (\Omega R)^2 c} \tag{61}$$

In the present computation the density variation is very small and has been neglected in the above definition.

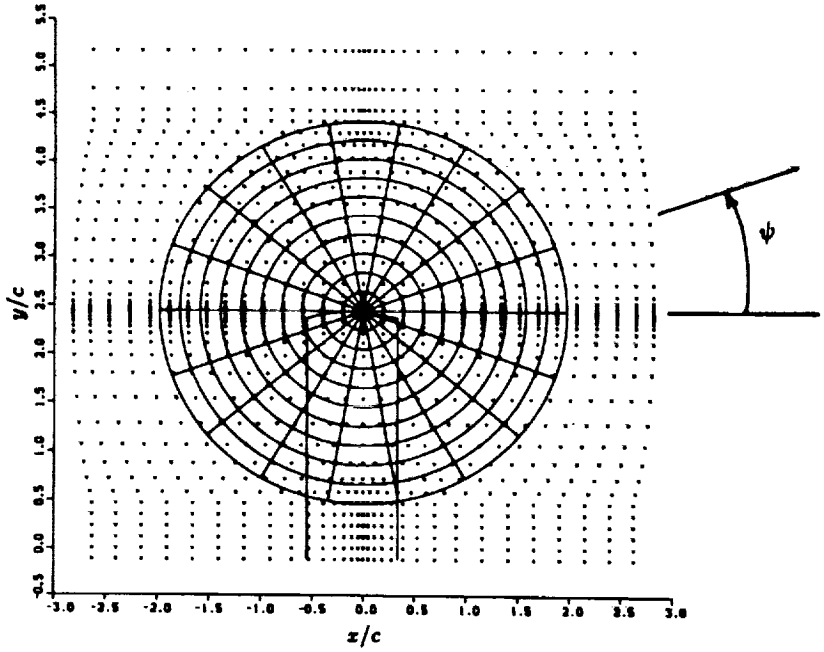

Figure 10: Top view of grid points in rotor plane, superimposed with the outline of the subdivided actuator disk.

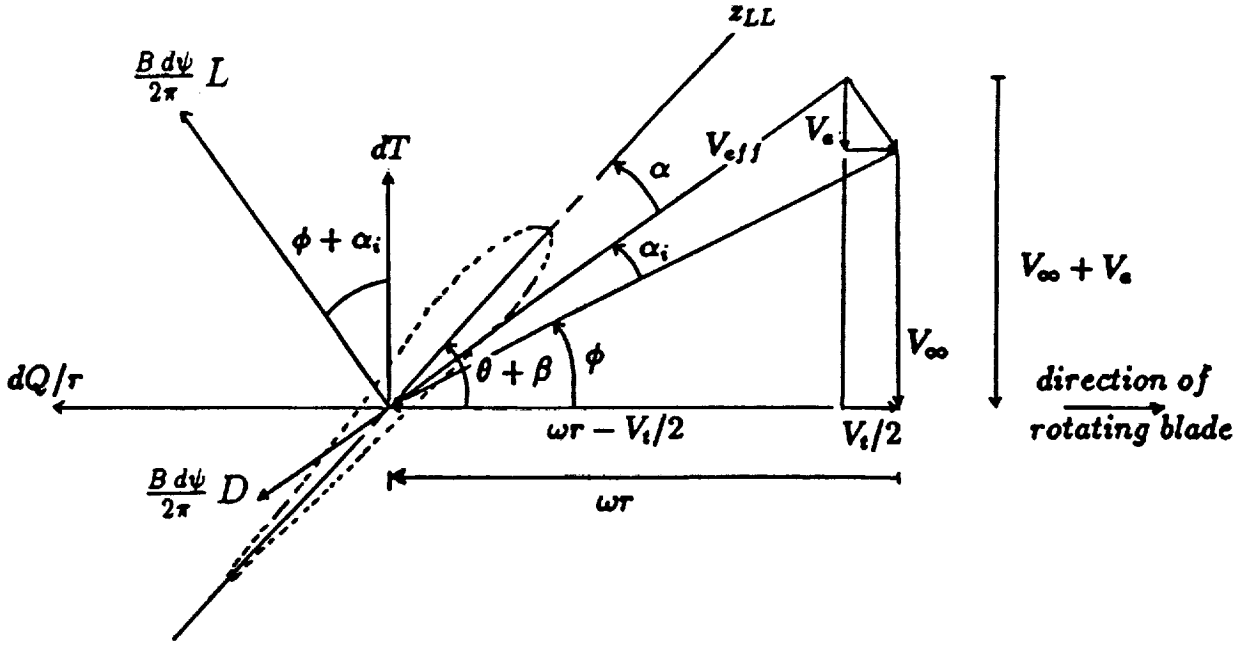

Figure 11: Relative velocities and forces at an elemental area of the rotor disk.

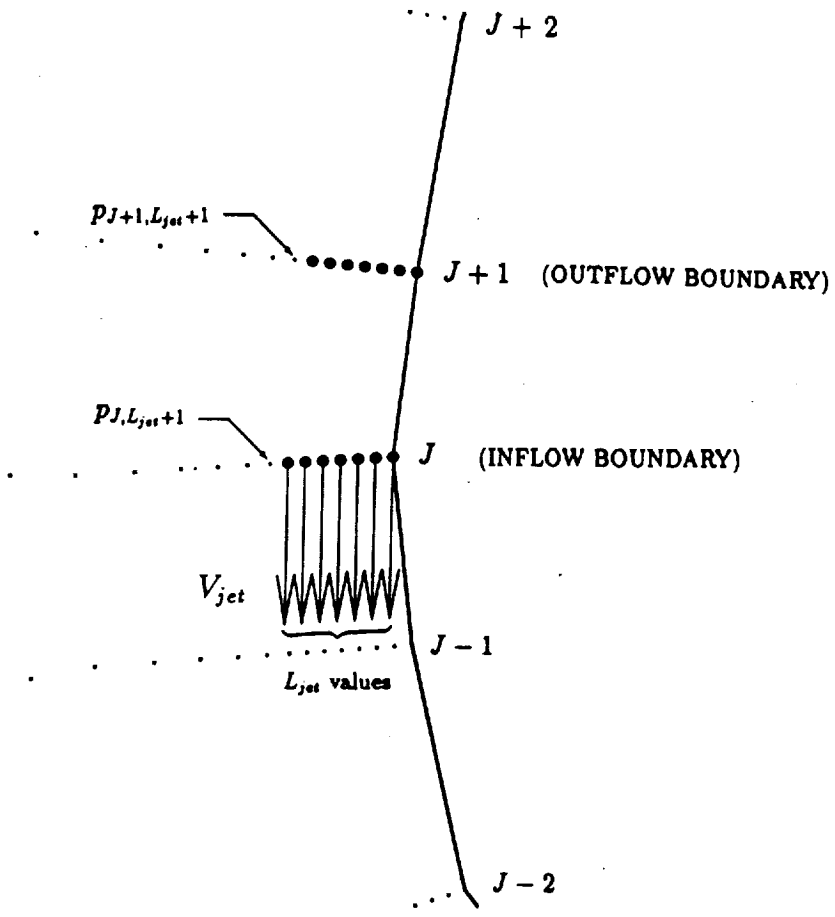

Figure 12: Blow-up of grid near the leading edge showing the inflow and outflow boundary conditions implemented for the tangential jet.

Chapter 5

Discussion of Results

5.1 Preliminary Comments

This chapter presents the results obtained for a variety of cases involving computations of a rotor alone and wing/rotor interaction. Results for the rotor alone serve not only to validate the current numerical model, but also to highlight some of its limitations. Computations have been performed for a uniformly-loaded rotor with no swirl, where a constant pressure rise across the disk is specified. Results for a non-uniformly-loaded rotor with swirl are also presented, where the rotor is modeled using the blade element/momentum theory described in Chapter 4. Computed results of wing/rotor interaction are presented for both of the above rotor models. This highlights the effects on wing download of swirl in the rotor flowfield. Finally, the effect on download of tangential blowing at the wing leading edge is shown.

Most of the visualization of the grids and solutions during the course of this work, and many of the figures in this report, have been generated using the computer graphics program known as PLOT3D [71,72]. Developed by Buning at NASA Ames Research Center, PLOT3D is a powerful interactive graphics tool capable of calculating and displaying a considerable number of different flowfield functions including pressure, Mach number, velocity vectors, and particle traces.

5.2 Rotor Alone

Accurate definition of the wing using stacked O-grids, as discussed in Chapter 3, results in a Cartesian-like grid representation for the rotor (refer, for example, to Fig. 10). Therefore, to provide a test, for the rotor alone, which is representative of the rotor model in the wing/rotor interaction computations, a Cartesian grid is used. The outer boundaries of the Cartesian grid extend five rotor radii from the rotor disk axis of rotation in the horizontal and vertical directions. The grid has dimensions of 47x47x47 with most of the grid points clustered in the region of the rotor disk. On each of the two principal axes on the rotor disk are defined 26 points along the rotor diameter. The grid spacing stretches from a minimum of $0.01R$ at the plane of the rotor to $0.4R$ at the top and bottom boundaries. The grid point distribution, though not identical to, is representative of that used in the wing/rotor computations discussed later. Figure 13 shows both a vertical cut and a horizontal cut through the center of the grid. The side view shows the clustering of points near the edge of the rotor. The location of the rotor disk is highlighted in the top view. All rotor alone computations assume that the flowfield is laminar throughout.

5.2.1 Rotor with Uniform Loading and No Swirl

Figures 14–16 show typical results for a uniformly-loaded rotor disk without swirl. As mentioned in Section 4.3, the presence and influence of the nacelle and the rotor hub have been neglected. For the results discussed here, a pressure rise $\Delta p/p_\infty = 0.0119$ is specified across the rotor. Since Δp is constant, it also represents the rotor thrust loading T/A. From the definition of the rotor thrust coefficient C_T (see Eq. 57), and assuming a rotor tip Mach number $M_{tip} = 0.72$ (typical of the experimental rotor tests described in Refs. [9,10]) and freestream conditions for density and speed of sound (reasonable assumption for the relatively low induced flow speed of the tilt rotor in hover), then for $\Delta p/p_\infty = 0.0119$, the rotor thrust coefficient is 0.0164. A value of $C_T = 0.0164$ is specified for many of the computations discussed in this chapter as it represents a typical thrust loading for the V-22 in hover. Also, experimental data exists at or near this value of C_T.

Figure 14 shows the contours of static pressure normalized by freestream pressure p/p_∞ around and through the rotor in a vertical plane through the rotor diameter. The cross-section of the rotor, whose dimensions have been normalized with respect to rotor radius, has been superimposed on the plot. Far above the rotor, the pressure is freestream ambient. As the rotor disk is approached from above, the flow accelerates and the static pressure drops. Note the pressure jump across the rotor disk. The flowfield is driven solely by this pressure rise. Below the rotor, the flow recovers its freestream value as the induced rotor flow attains a constant velocity. The contours of velocity magnitude (normalized by the freestream speed of sound) presented in Fig. 15 clearly show the flow being accelerated from a quiescent state above the rotor, drawn into the rotor, and accelerated to some maximum value below the rotor. This behavior is expected from simple momentum theory (see, for example, Ref. [18]). From momentum theory, the ideal induced velocity at the rotor disk is given by

$$V_h = \sqrt{\frac{T}{2\rho A}} \tag{62}$$

Note that by substituting Eq. 57 into Eq. 62, the ideal induced velocity can also be expressed in terms of the rotor thrust coefficient in hover, i.e.

$$V_h = \Omega R \sqrt{\frac{C_T}{2}} \tag{63}$$

As previously mentioned, for Δp uniform on the rotor disk, $T/A = \Delta p$. From Eq. 62, then, with $\Delta p/p_\infty = 0.0119$, and assuming freestream density, the ideal induced hover velocity normalized by the freestream speed of sound V_h is 0.06519. From simple momentum theory, the velocity induced in the far wake is twice that at the rotor disk; i.e. for this case, $2V_h = 0.1304$. This compares well with the computed value of 0.133. From Fig. 15 it can be seen that the flow into the rotor is fairly uniform except for a slight variation of induced velocities in the rotor plane along the diameter. The average flow velocity through the rotor disk appears to be somewhat higher than the ideal value of V_h. Also, the rotor wake contraction to 71% of the rotor diameter, anticipated from momentum theory, is not fully attained in the computation, as is shown more clearly in the next section. This is due to the fact that there is an insufficient number of grid points, particularly on the outer portion of the rotor disk

and wake, to compute more accurately the edge of the wake and its contraction. This lack of resolution in the wake also affects the computed flowfield at and above the rotor disk. Velocity contours in the wake (see Fig. 15) show that the flow velocities are fairly constant in the far wake along its width. Some wake dissipation is evident as the flow approaches the exit boundary — i.e. the flow gradually decelerates and the wake widens slightly. This is due to a combination of numerical and artificial diffusion. Numerical dissipation increases with increasing grid cell size. The stretched grid spacing below the rotor (refer to Fig. 13), therefore, contributes to the diffusion of the wake. The Cartesian grid makes it difficult to resolve the axisymmetric rotor flowfield with uniform accuracy for all azimuths of the rotor disk. This contributes to the slight non-uniformity on the rotor disk.

Figure 16 shows the velocity vectors through the rotor projected onto the vertical plane. Note the changing flow angles as the rotor disk is approached from above. The flow accelerations described above are clearly indicated by the changing lengths of the velocity vectors. The effect of numerical diffusion can be seen at the edge of the rotor slipstream. Experimental data shown later in this chapter indicates that the edge of the actual slipstream is considerably more distinct and the velocity gradient significantly greater. A finer mesh would be required to better resolve the shear layer formed between the inner and outer flowfields.

5.2.2 Rotor with Non-Uniform Loading and Swirl

This section describes the results obtained for a rotor imparting non-uniform radial distributions of pressure rise across the disk and of swirl velocity. The rotor simulated is the V-22 rotor operating at a thrust coefficient of 0.0164 and a rotor blade tip Mach number $M_{tip} = 0.72$. The blade chord and twist distributions, required for the blade element analysis, are taken from Ref. [10]. The blade geometry is extrapolated inboard from the hub location (at $r/R \approx .09$) to the rotor centerline ($r/R = 0$), as can be seen in Fig. 17. Similar to the uniformly-loaded rotor model discussed in the previous section, the presence and influence of the nacelle and the rotor hub are neglected.

The rotor disk is divided into annular elemental areas of equal width dr. Since circumferential variations do not exist for a rotor alone (modeled as an actuator disk) in

hover, the annuli are not subdivided azimuthally as is done for the wing/rotor interaction computations discussed later in this chapter. For the computations discussed here, the rotor disk is subdivided into 10 annular rings.

The only modification made here, to the rotor model described in Chapter 4, is the imposing of a limit on the magnitude of swirl velocity allowed at the most inboard annulus. It was found that not constraining the swirl often yielded unstable solutions because of the far-from-optimum flow angles in the blade root region where the rotational speed approaches zero. This resulted in the computation of oscillatory positive and negative swirl velocities. The swirl at the inner-most annulus is, therefore, constrained to be positive and less than 0.06 when normalized by the freestream speed of sound. It was found that this did not significantly affect the converged solution because the computed swirl velocities were always somewhat less than this value.

Figure 18 shows the computed radial distributions of blade loading (local blade lift and drag coefficients, C_l and C_d, respectively) and local blade angle of attack α for a non-uniformly-loaded rotor with $C_T = 0.0164$. Figure 19 shows the radial distributions of axial velocity V_a and swirl velocity V_t, normalized by the freestream speed of sound, computed at the rotor disk (i.e. at the horizontal layer L of rotor grid points — see Chapter 4). Experimental measurements of rotor blade loading and local flow angles and velocities in the rotor disk, or immediately below it, are difficult to make, and none are available for the V-22 rotor. Beyond the inner region of the rotor, say for $r/R \geq 0.2$, the computed results shown in Figs. 18 and 19 are probably fairly representative of the actual loads and velocities. Referring to Fig. 18, note that proceeding radially outwards, the angle of attack decreases and C_l tracks this behavior. The dip in the C_l curve and the spike in C_d near $r/R = 0.25$ is due to the local angle of incidence exceeding the stall angle, resulting in a local loss of lift and a large increase in drag. Due to the reduced axial velocities at the outer edge of the rotor disk, a slight increase in α is predicted at the blade tip. Being well below the stall angle, the local lift coefficient also increases proportionately. The increase in drag, however, is due not to the change in α, but to compressibility effects in the tip region (remember that $M_{tip} = 0.72$). Compressibility drag is introduced through the table look-up described in Section 4.3. Due to the absence of the hub, axial flow is induced

in the inner region of the rotor disk. The blade twist at the root is insufficient to accommodate the relatively high axial velocity (relative to the rotational component of velocity) as evidenced in the rapid drop to a negative angle of incidence. This causes C_l to become negative, and in turn, would yield a negative swirl velocity if V_t hadn't, rather arbitrarily, been set to zero for reasons mentioned previously. Outboard of the hub region, however, as can be seen in Fig. 19, the swirl, which is generally greatest in the inboard region of the rotor disk, decreases as r/R increases. The increase in swirl at the tip is due to the local increase in lift and drag coefficients, described above. The increase in the induced axial velocity V_a from the rotor center outboard, as evidenced in Fig. 19, is expected for a $C_T = 0.0164$. The effect of C_T on local induced velocities is discussed in more detail below, where comparisons with experiment are made. The relative magnitudes of swirl velocity with respect to axial velocity are representative of the actual rotor flowfield. From momentum theory analysis (see Ref. [18]), it is known that swirl velocities are generally considerably smaller in magnitude than are axial velocities except in the inboard region of the rotor disk where their magnitudes may be similar.

Figures 20 and 21 show the contours of normalized pressure (p/p_∞) and of normalized velocities ($|V|/a_\infty$), respectively, in a vertical plane through the center of the rotor disk. Comparing these figures with Figs. 14 and 15, the non-uniform rotor disk loading is clearly seen to cause a significant flow non-uniformity radially, particularly near the rotor disk. Figure 20 actually shows a small amount of negative loading produced near the center of the rotor disk. This is a result of the far-from-optimum flow angle that the rotor blade sees in this region. As mentioned previously, the rotor blades are assumed to extend all the way to the rotor center, thereby neglecting the presence and influence of the rotor hub. The maximum computed induced velocity in the rotor wake is 0.1300 which is near identical to the ideal induced velocity $2V_h = 0.1304$ derived from Eq. 63, again providing confidence that the current rotor model is valid. The velocity contours show that the wake exits the lower boundary as expected. The gradual spreading of the contour lines, however, again demonstrates the effect of numerical dissipation.

As mentioned in Chapter 4, the rotor imparts a rotational or swirl velocity component to the flowfield. Above the rotor, the swirl is zero. Below the rotor, the rotational motion is maintained in the wake downstream of the rotor. Figures 22 and 23 show the effect of the swirl computed by the non-uniformly-loaded rotor model with $C_T = 0.0164$. Figure 22 shows views of the velocity vectors projected onto two different horizontal planes: (i) immediately above the rotor, and (ii) immediately below the rotor. The extent of the rotor disk is shown on these plots. The view labeled "immediately above rotor" is actually a view looking down at the horizontal plane that contains the $L + 1$ layer of rotor grid points (see Chapter 4). As expected, the swirl is effectively non-existent. The view labelled "immediately below rotor" shows the results at the "L" layer of rotor grid points. The swirl velocity, computed using the blade element/momentum theory analysis described in Chapter 4, is specified at these points. Figure 22, then, serves to confirm that the discontinuous nature of the swirl motion is being computed. Figure 23 shows two views of particle traces which demonstrate the effect, on the flowfield downstream of the rotor, of the swirl imparted at the rotor disk. Particles are seeded into the flowfield at every grid point on the rotor centerline immediately above the rotor. The side view clearly shows that the rotational flowfield motion imposed at the rotor is communicated to the flowfield beneath the rotor, as expected. The top view also shows the rotation in the flowfield. The wake contraction is clearly evidenced. The wake contracts very quickly beneath the rotor disk to a minimum diameter of about 84% of the rotor diameter. As mentioned in the previous section, the wake contraction, from simple momentum theory, is 71% of the rotor diameter. The azimuthal non-uniformity of the computed wake seen in the top view of Fig. 23, and the discrepancies between the computed and the theoretical wake contraction are due, in large part, to the difficulty that the Cartesian grid is experiencing in computing more accurately the cylindrical-shaped flowfield. Along lines that are forty-five degrees to the principal axes of the grid in the horizontal plane, the mesh resolution of the outer edge of the rotor disk and its wake is at its worst. This can be more clearly visualized by referring back to Fig. 13 which shows the top view of the grid. Use of a finer mesh and a cylindrically-shaped one would help to further improve the solution.

CHAPTER 5. DISCUSSION OF RESULTS

The comparisons discussed below are made with experimental results obtained for a 0.658-scale V-22 rotor in hover (see Refs. [2,9]). The computed results shown are for a case where the rotor is alone, not influenced by a plane of symmetry. Figure 24 is a plot of the induced velocity as a function of radial location. The induced velocities are those in a horizontal plane below the rotor at a vertical location that corresponds to the position of the wing of the V-22 tilt rotor configuration. The velocities are normalized here by the ideal induced velocity at the rotor disk in hover V_h defined in Eq. 63. The results for two different thrust coefficients are presented: $C_T = 0.0164$ and $C_T = 0.0051$. The experimental tests show that the radial distribution of induced velocity is sensitive to the thrust coefficient. For the twist distribution of the V-22 rotor blades, as C_T and the corresponding blade pitch angle increase, the local aerodynamic blade loading becomes greater in the outboard region of the rotor thereby inducing greater velocities in the outer portion of the wake. At low thrust coefficients, the inboard region is more highly loaded. As can be seen from Fig. 24, these trends with C_T are predicted numerically although the actual computed velocities differ somewhat from the experimental measurements. The computed velocities extend to the rotor centerline because, as previously mentioned, the nacelle has not been modeled. The diffusion of the slipstream shear layer, discussed earlier, prevents a more accurate prediction of induced velocities.

Figure 25 shows a comparison of rotor figure of merit *FM* (defined in Eq. 58 of Chapter 4) between experimental results taken from Ref. [2] and computational results. As the thrust coefficient decreases, the disk loading decreases, thereby reducing the induced power relative to the profile power. The figure of merit, therefore, decreases as C_T decreases. Due to blade stall at high C_T, the profile losses increase and the figure of merit again begins to drop. The experimental figure of merit is predicted quite well by the numerical computation, over a range of rotor thrust coefficients. These results show that, despite the inaccuracies associated with not modeling the hub and nacelle or the discrete vorticity (rotor tip vortices) in the wake, and with less than optimum grid resolution due to limited computer resources, the current actuator disk model of the rotor simulates the expected overall flowfield behavior fairly well.

5.3 Wing/Rotor Interaction

The results discussed in this section are from computations of wing/rotor interaction in hover. To verify, at least qualitatively, that the method developed here yields solutions that are intuitively correct, the first computations described are for a uniformly-loaded rotor with no swirl. These results are followed by wing/rotor computations where the rotor model described in Section 4.3 is used. The non-uniform loading and swirl calculated by this model is a far better simulation of the actual rotor flowfield. Comparisons are made with experimental measurements of wing pressures and download. Also, comparisons of the computational results are made between the uniform and the non-uniform with swirl rotor models. This clearly shows the effect of swirl on the wing. Finally, computations of tangential jet blowing are described.

The geometry of the V-22 wing/rotor configuration is used as a basis for the numerical model. There are, however, notable differences. As mentioned in previous chapters, to simplify the grid generation, the fuselage, tail, nacelle, and rotor hub are not modeled. The six degrees of forward sweep of the V-22 wing is also not modeled. The wing and rotor are assumed in this study to be coplanar when they are actually angled 6° with respect to each other. The V-22 possesses 3.5° of wing dihedral and 2.5° of lateral nacelle cant. The nacelle is not modeled, and the center of the rotor is placed above the wing tip (not displaced outboard a distance equal to the nacelle half-width as in the actual configuration). The rotor radius of the numerical model is therefore reduced by the nacelle half-width to keep the extent of the rotor disk which lies above the wing essentially the same for both the actual and the computational configurations. The rotor disk of the numerical model was centered above the wing tip in anticipation of future comparison of results with those obtained from a NASA Ames OARF (Outdoor Aerodynamic Research Facility) test of a simplified 0.16-scale wing/rotor configuration (which has no nacelle). Normalized by the wing chord, the effective rotor radius is 1.98, the wing semi-span is 2.45, and the rotor height above the wing is 1.10 (an average of the varying height of the V-22 rotor disk above the wing). The wing is of constant chord with an airfoil section having a thickness/chord ratio of 0.23. Unless noted otherwise, the results reported here are all with the flap

deflected to 67°. The rotor axis of rotation is, as mentioned above, located at the wing tip, and is 55% of the wing chord aft of the wing leading edge. A rotor blade tip Mach number of 0.72 is assumed for all the calculations. Also, except where noted otherwise, the rotor thrust coefficient is 0.0164. The Reynolds number for the calculations described here is based on wing chord and ideal hover induced velocity. For $C_T = 0.0164$, the Reynolds number is $2.6\text{x}10^6$. No attempt is made to model the turbulence imparted by the rotor into the rotor slipstream.

5.3.1 Rotor with Uniform Loading and No Swirl

Similar to the rotor alone computations described in Section 5.2.1, a uniform rotor disk loading of $\Delta p/p_\infty = 0.0119$ is specified. As previously mentioned, with $M_{tip} = 0.72$, this corresponds to an effective thrust coefficient of 0.0164. Figures 26 – 34 show the results obtained with the uniformly-loaded rotor.

Figure 26 is a perspective view of the computed velocity vectors on the near-vertical computational grid plane that runs through the wing mid-chord line. The viewpoint is outboard of the wing tip and ahead of and above the wing. Flow acceleration through the rotor disk is clearly evidenced as is the flow stagnation on the wing upper surface. Close examination of the region below the wing tip shows the existence of a standing vortex. A recirculation flow pattern — the fountain flow — is also visible in the wing root region adjacent to the plane of symmetry.

Figures 27, 28, and 29 show the velocity vectors, the velocity magnitude (normalized by a_∞), and the pressure (normalized by p_∞), respectively, in a vertical plane that runs spanwise through the wing mid-chord. From Fig. 27, it can be seen that the flow is near-vertical beneath much of the rotor. The flow is spanwise outboard in the wing tip region both on the upper surface and the lower surface. As the wing surface is approached from above, the flow stagnates at about the three-quarter semi-span location and is re-directed spanwise inboard and outboard. The velocity vectors at the inboard region of the wing indicate that at this mid-chord location, the fountain extends less than 0.5c above the wing. As is shown in the next section, a portion of the computed fountain reaches a height of one chord above the wing, but at an x/c location further forward on the wing. The blockage effect of the wing on the flowfield

is clearly seen in Figs. 28 and 29 by comparing the flow above the wing with the flow outboard of the wing. The presence of the wing tends to reduce the velocity and increase the pressure in that portion of the rotor flowfield that lies above the wing. The small discontinuities at $2y/b = 2.45$ are due to an insufficient number of 2-D grid planes in the wing tip region to adequately resolve the flow. Convergence of the solution near the singular line that emanates spanwise from the wing tip (refer to Chapter 3) is slow, and a small residual effect is seen in the velocity magnitude contours.

Figures 30, 31, and 32 are views of the flowfield at a typical spanwise station, $2y/b = 0.7$. The location of the rotor disk is highlighted in the figures. Figure 30 shows the velocity vectors projected onto the vertical plane. Because there is no swirl, the flow through the rotor is near-symmetric about a vertical line running through the center of the rotor. These results are compared later with those obtained with the rotor swirl modeled. It will be seen that swirl introduces considerable asymmetry to the flowfield. From Fig. 30, it can be seen that the flow impinges on the wing surface and is re-directed fore and aft, accelerating around the leading edge and the knee (junction of main foil and flap) of the flap. In the wake beneath the wing the computation predicts the formation of two side-by side vortices, one shed from the leading edge and the other shed from the trailing edge. Whether this represents the real physical flowfield or not must be determined from future experimental measurements and flow visualization. The influence of the wing on the rotor flowfield is clearly evidenced in the velocity and pressure contour plots of Figs. 31 and 32, respectively. The presence of the wing reduces the velocity and increases the pressure of that portion of the rotor flowfield which lies above the wing. As expected, as the wing surface is approached from above, the flow continues to decelerate and the pressure continues to increase. Away from the wing, near the edges of the rotor wake, the flowfield remains essentially unaffected by the wing. The influence of the wing on the rotor flowfield can be better appreciated by comparing with the results of the rotor alone, Figs. 14, 15, and 16. The oscillations in the pressure immediately below the rotor could probably be eliminated by further grid refinement.

Convergence of the numerical solution is determined by the attainment of a steady

value of the mean download/thrust ratio, i.e. when the time-averaged download/thrust $\overline{DL/T}$ is constant. Actually, the computation was generally stopped when the percent change in time-averaged download/thrust between cycles was less than 0.2. "Pseudo 2-D" computations of an airfoil/actuator line configuration were performed during the course of this work to aid in the development of the numerical method, the grid, and the boundary conditions. These two-dimensional computations showed a much greater degree of unsteadiness in the flowfield than is observed in the three-dimensional results. This is due to the alternate shedding of vorticity from the leading and trailing edges that is computed in 2-D but not in 3-D. In two dimensions, it was observed that these vortices propagate downstream in a vortex street typical of bluff body flows. Results from these 2-D calculations were reported by the author in Ref. [73]. This unsteady wake behavior has also been computed in the two-dimensional analyses undertaken by Raghavan et al. [16] and Stremel [17] for low Reynolds number laminar flows. As mentioned previously, the converged three-dimensional solution shows two standing vortices, of opposite sense of rotation, side-by-side beneath the wing. This difference in unsteadiness of the wing wakes between the 2-D and 3-D computations is manifested in a plot of instantaneous DL/T versus non-dimensional time $t\,a_\infty/c$. Figure 33 shows the behavior of download/thrust with time as the computation proceeds, starting with an initially-quiescent flowfield and an impulsive start of the rotor pressure rise. Both the 2-D and 3-D computations show high frequency start-up transients which damp out rapidly. There is an overshoot of DL/T before a near-constant mean value is reached. Computations are generally continued a few more cycles than shown here, until the mean value of DL/T varies less than about 0.2% between cycles. The 2-D computation takes longer to settle to a constant mean value and the amplitude of periodic oscillation of download/thrust is much greater than in the three-dimensional computation. As previously mentioned, the differences in the unsteadiness are due primarily to the differences in the computed vortical flow in the wing wake. Lack of experimental data for, and flow visualization of, this type of flowfield make it difficult to determine the validity of the wake solutions. One would expect, however, less flow unsteadiness in 3-D due to the relaxing effect of a finite wing on the flowfield, but to what

extent is unknown. The observed differences in the computed wakes are probably due to a combination of flow physics, an insufficient number of grid points to resolve all the complicated flow features, numerical and artificial dissipation, and simplifications made in the thin-layer Navier-Stokes equations and in the turbulence model. Suggestions for improvements to the current model are discussed in Chapter 6.

Figure 34 is the computed oil flow pattern on the wing upper surface, viewed form the rear beyond the wing tip. The flow stagnates in the three-quarter semi-span region of the wing, and from this location the flow is re-directed spanwise inboard and spanwise outboard. The flow symmetry at the wing centerline is evidenced in the wing root region. The flow is primarily chordwise in the outer region of the wing and becomes more spanwise inboard, as expected. At the wing centerline the flow is re-directed chordwise fore and aft as indicated by the oil traces, and also vertically upwards to form the recirculation fountain. Note that the flow proceeds smoothly over the flap with no sign of separation.

5.3.2 Rotor with Non-Uniform Loading and Swirl

The results discussed below are for wing/rotor interaction where the non-uniform loading and swirl imparted by the rotor is modeled, using the method described in Chapter 4. The rotor model is the same as that used to obtain the rotor alone results of Section 5.2.2. The computations discussed below are for a case where the rotor thrust coefficient is 0.0164 and the rotor tip Mach number is 0.72. When comparisons with experiment are made, the data is taken from either the OARF test (see Ref. [9]) or the 40- by 80-Foot Wind Tunnel test (see Ref. [10]) conducted at NASA Ames Research Center on a 0.658-scale V-22 rotor and wing used to study wing/rotor interactions in hover. Figure 35, taken from Ref. [10], is a schematic of the 40- by 80-Foot Wind Tunnel model installation showing the wing, rotor, image plane, and model support structures.

Many of the flow features that were described in the previous section, computed using a uniformly-loaded rotor disk with no swirl, also occur when the more-representative model of the rotor is used. The fountain flow at the plane of symmetry,

C-2

the chordwise flow on the outer region of the wing surface and the spanwise flow further inboard, the standing vortex beneath the wing tip, and the flow accelerations through the rotor and around the leading and trailing edges are all observed with the non-uniformly-loaded rotor disk model. The results shown in this section serve to highlight the flow features that either do not appear or are somewhat different if the non-uniform loading and swirl are neglected.

The rotor's introduction of swirl into the flowfield is clearly shown in Fig. 36. Figure 36(a) shows the velocity vectors projected onto a horizontal plane immediately above the rotor. The flow is generally radial inwards towards the center of the rotor. In the region above the wing tip, it appears that the presence of the wing tip causes a small amount of radial-outwards movement of the flow. Figure 36(b) shows the velocity vectors in a horizontal plane immediately below the rotor. The increasing tangential (swirl) component of the vectors, as one moves from the edge of the rotor disk towards the center of the rotor, represents the increasing magnitude of the swirl, similar to that observed previously for the rotor alone in Figs. 19 and 22.

The fountain flow is clearly seen in Figure 37 which shows the instantaneous particle traces in a near-vertical spanwise plane in the region of the wing root. Note that the particles are drawn into the rotor from above, and as the wing surface is approached, the flow is re-directed spanwise inboard and outboard. Similar views can also be seen when rotor swirl is not modeled. It seems, then, that swirl has very little effect on the strength or location of the fountain. The fountain reaches a maximum height of about 1 chord above the wing surface at a chordwise location between the mid-chord and the leading edge — i.e. in the vicinity of the maximum thickness location of the airfoil section which lies at $x/c \approx 0.30$. Limited experimental flow visualization was obtained from the OARF test of the 0.658-scale model of the V-22 wing, rotor, and wing/fuselage fairing [9]. Tufts on the image plane and smoke released near the plane of symmetry indicate that the actual recirculation pattern (fountain) is somewhat larger than that computed, extending about two chords above the wing. This difference can at least partially be explained by the presence of the large wing/fuselage fairing in the experimental model which tends to increase the portion of the flow that is re-directed upwards.

Figure 38 is a perspective view of the computed oil flow pattern on the wing upper surface, as seen looking from the rear towards the flap from beyond the wing tip. The numerical results show the transition of primarily two-dimensional flow to three-dimensional flow towards the wing root. Flow visualization from the OARF test indicates that the 2-D behavior extends to the wing tip, whereas the computation yields considerable spanwise flow over the tip. This discrepancy may be due, at least in part, to the flow straightening effects of the nacelle and large, flat model support structure used in the test (refer to Fig. 35). In the three-quarter semi-span region, where the flow is primarily chordwise, the flow separates on the flap due to the adverse pressure gradient, and a region of flow reversal can be seen on the upper surface of the flap in Fig. 38. This flow separation on the flap does not occur when the rotor-induced swirl is not modeled. As seen previously in Fig. 34, the flow is smooth and unseparated over the entire length of the flap surface when the rotor is modeled as a uniformly-loaded disk with no swirl.

In the following discussions, reference is made to specific spanwise locations. As an aid to visualizing these locations relative to the extent of the rotor disk, reference should be made to Fig. 39. The edge of the rotor disk reaches a minimum spanwise value of $2y/b = 0.19$, or, relative to the wing chord, $y/c = 0.47$. Figure 40 is a typical view of the projection of velocity vectors onto a vertical, chordwise plane that lies well within the rotor slipstream — here corresponding to $2y/b = 0.7$. Note the discontinuity in velocity direction at the rotor disk due to the swirl imposed there. The leading edge-to-trailing edge bias in the flowfield is also due to rotor swirl. In contrast, for a case where the swirl is zero, Fig. 30 of the previous section shows a flowfield that is much more symmetric about the mid-chord with no velocity discontinuity at the rotor disk.

Figure 41 shows a comparison of wing surface pressures at the same spanwise location as above, i.e. $2y/b = 0.7$, computed using the two different rotor models. The pressures are relative to freestream ambient pressure, normalized by rotor thrust loading, i.e. $(p - p_\infty)/(T/A)$. Due to the unsteadiness in the wake that causes small amplitude fluctuations in download, these pressures are time-averaged over one period of oscillation of DL/T. Also, x/c is the distance along the chord from the leading

edge, normalized by the undeflected flap wing chord. The computed base pressure (pressure along the lower surface) is uniform, typical of bluff body flows, and is near-identical for both cases — i.e. it appears to be quite independent of swirl. The upper surface, on the other hand, sees pressure distributions that differ considerably depending on whether the swirl is modeled or not. The pressure for the case with no swirl is somewhat more uniform and more symmetrical about the mid-chord. The flow stagnates in the mid-chord region. With swirl, however, the flow stagnates further forward, closer to the leading edge. Because of the swirl-induced bias in the flowfield, the flap sees an onset flow that is at a considerably higher angle of attack. This causes a greater local flow acceleration and reduced pressure at the knee of the flap, relative to the case where there is no rotor swirl. The flow experiences, then, a much larger adverse pressure gradient as it approaches the trailing edge. This contributes to the flow separation on the flap upper surface observed in Fig. 38 that does not exist in the absence of swirl (see Fig. 34).

Figure 42(a) – (e) show the wing surface pressure distributions at five different spanwise stations. The computational data has been linearly interpolated to obtain the pressures at the desired spanwise locations. The experimental data has been taken from the "normal" pressure coefficient distributions of Ref. [10]. As can be seen from the plots of Fig. 42, there is an insufficient number of experimental data points to resolve the negative pressure peaks at the wing leading edge. The comparison of computational results with the experimental measurements is generally more favorable in the mid-semispan region of the wing than at the root or the tip. Outside of the rotor wake, at $2y/b = 0.145$ (see Fig. 42(a)), the upper surface pressures compare very well while the computed base pressure is somewhat greater than the experimental values. This seems to indicate that the actual wake contains shed vortices whose strengths are a little greater than those computed. The negative pressure peak at the knee of the flap is very well-predicted. These same comments apply to Figs. 42(b) and (c), at $2y/b = 0.332$ and $2y/b = 0.518$, respectively, except that the upper surface pressures are over-predicted. At $2y/b = 0.705$ (see Fig. 42(d)), both the upper and lower surface pressures are very well predicted. That the upper surface pressures compare so well

at $2y/b = 0.705$, but not as well further inboard on the wing, is due to differences between the computed and the actual rotor-induced velocities. As discussed earlier for the rotor alone results (refer to Section 5.2.2), these discrepancies are due primarily to an insufficient number, and less than optimum distribution of, grid points required to adequately resolve the radial distribution of rotor-induced flow. This contributes to inaccuracies in resolution of the rotor flowfield and to unwanted numerical dissipation which causes diffusion of the edge of the rotor slipstream.

Figure 42(e) shows the comparison of pressures near the wing tip, at $2y/b = 0.891$. The upper surface pressure is generally under-predicted as a result of the spanwise-outboard flow computed in the tip region (see, for example, Fig. 38) relative to the primarily chordwise flow seen experimentally. This also explains the reduced negative pressure peak over the flap, compared with experiment. Spanwise flow towards the wing tip was also computed in the previous section where a uniform pressure rise was specified across the rotor. This difference between the computed and the experimental flowfields, as stated previously, can be partially attributed to the flow straightening effects of the nacelle and model support structure of the experimental set-up. Also, the fact that the rotor centerline is actually about $13\%R$ outboard of the wing tip of the experimental model, encourages 2-D flow near the wing tip. As mentioned previously, anticipating future comparisons of results with on-going tests of a 0.16-scale simplified tilt rotor configuration at NASA Ames, the center of the rotor disk for the computation is above the wing tip — not displaced beyond the wing tip. The offset rotor centerline reduces the affect on the wing of the poor quality, low dynamic pressure flow that is generated at the inboard rotor region due to the far-from-optimum blade angles and blade thickness, and rotor hub interference. Thus, the flowfield in the wing tip region of the experimental model probably has a greater axial component which results in the greater chordwise flow. It should be remembered that the computed flow velocities and angles in the inner region of the rotor are not accurate representations of the actual flowfield. This contributes to the discrepancies in wing surface pressures in the wing tip region between the computational and the experimental results. The computed lower surface pressures at $2y/b = 0.891$ are somewhat less than the measured values. This is also probably due

to the increased spanwise flow predicted for the tip region. This causes a stronger tip vortex to be formed beneath the wing tip (see the standing vortex in Fig. 26) which induces a greater velocity at the lower wing surface reducing the base pressure.

Bearing in mind the differences in configuration between the computational and experimental models, the comparison of wing surface pressures is generally quite good.

Figure 43 compares the computed and measured time-averaged download/thrust per unit span normalized by the total time-averaged download/thrust. The computed distribution generally follows the shape of the experimental distribution. The edge of the computed rotor wake is diffused over several grid points, thus contributing to the more gradual download gradient in the region $0.2 < 2y/b < 0.5$. Greater grid point density, particularly in the region of the edge of the rotor slipstream, would be required to compute the spanwise download distribution more accurately. There is insufficient experimental data to observe the expected local increase in download at the wing root. The local increase in DL/T, predicted by the computation, is produced by the change in momentum due to the flow turning away from the surface in the recirculating fountain near the wing centerline.

The computed time-averaged download/thrust is 0.113 for the specified rotor thrust coefficient $C_T = 0.0164$. This is somewhat higher than that measured in the 0.658-scale model tests at NASA Ames, for the same thrust loading. For flaps deflected to 67°, and at a rotor tip Mach number approximately 0.70, a DL/T of 0.093 was measured in the OARF test [9] and a $DL/T = 0.078$ was measured in the 40- by 80-Foot Wind Tunnel test [10]. The latter test was performed with the nacelle set at an angle of 85 degrees with respect to the wing chord line (tilted forward slightly) — not at 90° which is typical for the V-22 aircraft in hover. Felker [11] estimates that the download is reduced by about one percent of rotor thrust for 10° of forward nacelle tilt. Using this as a guideline to estimate the download with the nacelle set at 90° gives $DL/T = 0.083$. The configurations for the two NASA tests were essentially the same except that the OARF model included a fuselage fairing, and the rotor for the 40- by 80-Foot Wind Tunnel test was slightly modified at the blade root. The presence of the fuselage fairing in the OARF test increases the download/thrust, but to what extent is unknown. It is interesting to note that, extrapolating flight test

data presented in Ref. [2], DL/T for the XV-15 aircraft at flaps 67° is approximately 0.10. The figure of merit, calculated from the current computation, is 0.746. This compares with 0.755 computed for the rotor alone (see Fig. 25). The tendency for the hover efficiency to drop when the rotor is in the presence of the wing (in the tilt rotor configuration) was also observed experimentally at the OARF. The measured figure of merit was reduced by about 2%, and as discussed in Ref. [2], is due to the negative impact of the re-ingested flow from the fountain.

Even accounting for uncertainties associated with the experimental measurement of download/thrust, the computed DL/T is somewhat greater than expected. This discrepancy can be attributed to several factors. The rotor plane and wing are not coplanar in the experimental models, as discussed earlier in Section 5.3. This is expected to contribute to the lower measured download/thrust, relative to the computed value. As discussed earlier, the lack of sufficient number of grid points and the less than optimum grid point distribution, particularly near the edge of the rotor slipstream, contribute to inaccuracies in the computed solution. Early computations using a grid of size 53x42x46 — a size selected to permit job execution in the 4 megaword memory queue of the CRAY Y-MP — yielded a $DL/T = 0.185$. The present mesh (73x46x70) is the largest single zone grid that could be handled by the Cray Y-MP (whose current memory limit is 8 megawords per job). Despite the difficulty in performing grid sensitivity studies on problems of this magnitude, it is obvious that further work would be required to determine to what extent the number of grid points affects the solution. Another source of uncertainty in the results is the turbulence model. The Baldwin-Lomax eddy viscosity model, employed in this study, was developed for relatively benign flows where regions of separated flow are small. In Ref. [39], the method is validated for simple flat plate and compression corner supersonic flows and for low angle of attack transonic airfoil computations. This turbulence model and its empirically-based constants does not accurately describe the turbulence in the flow beneath a bluff body, or in the case of the tilt rotor in hover, beneath the wing. Finally, application of the thin-layer assumption to the complete Navier-Stokes equations (see Chapter 2) introduces inaccuracies in the computation of the highly complex and turbulent flowfield beneath the wing. This approximation assumes that

only those viscous stresses created by velocity gradients normal to the wing surface are significant. In a large separated flow, however, the viscous stresses associated with velocity gradients in directions tangential to the wing are also probably important.

Convergence took about 25 CPU hours on the Cray Y-MP for the fine grid results presented here. The mildly-compressible nature (local velocities are less than $M = 0.3$) of the flow of the tilt rotor in hover (the local transonic flow on the blades is not modeled) adds to the numerical stiffness of the equations. Also, due to the fact that the entire flowfield is being driven by a relatively small region of the computational domain, i.e. the rotor actuator disk, solution convergence is rather slow.

The wing/rotor results were obtained first for a uniformly-loaded rotor with no swirl. Applying the rotor model for non-uniform loading with swirl, an additional 6–8 CPU hours are required to again reach convergence, starting from the previous converged solution. Solutions at different flap settings, at different rotor thrust coefficients, with opposite sense of rotor rotation or with tangential blowing (discussed in the following section) can also be obtained from previous solutions and require similar increments of CPU time to reach convergence.

The preceding results in this section show the effect of the rotor flow on the wing. The presence of the wing, in turn, has an effect on the flow generated by the rotor. The current method for modeling the rotor allows the computation of the time-averaged effect of the wing on the rotor. Figure 44 shows the influence of the wing on the flow at the rotor disk. At a given radial location $r/R = 0.60$, the azimuthal variation of axial velocity, pressure rise, and local blade angle of attack are plotted. So as to place all three parameters on the same plot, the axial velocity is normalized by the ideal induced velocity in hover, i.e. V_a/V_h, the pressure rise is normalized by the rotor thrust loading, i.e. $\Delta p\,/\,(T/A)$, and the angle of attack is divided by seven, i.e. $\alpha/7$. The azimuthal extent of that portion of the rotor disk, that is swept by the radius $r/R = 0.60$ and which lies above the wing, is indicated on Fig. 44. The blockage effect of the wing causes a deceleration of the axial flow in that area of the rotor disk which is above the wing. This can be seen as a dip in the curve of V_a/V_h in the region of the rotor disk above the wing. The local reduction in the axial velocity in the rotor plane immediately above the wing causes a local increase in the blade angle of attack (refer

to Fig. 11 in Chapter 4). This produces an increase in the local lift and drag force coefficients. Despite the reduced dynamic pressure caused by the reduction in axial velocity, the increase in α and the corresponding increase in force coefficients causes an increase in the local aerodynamic lift force that results in an increase of pressure rise (normalized by the thrust loading) of about 0.07. Although the time-averaged azimuthal variations in rotor flow computed here are fairly small, it is useful to be able to compute them in order to evaluate their impact on rotor-induced vibration, and rotor stability and control.

5.4 Tangential Blowing

A tangential jet of air on the wing upper surface near the leading edge can be used to reduce the download of the tilt rotor aircraft in hover. As mentioned in Chapter 1, download reduction due to leading edge tangential blowing has been previously measured on a model circulation-control wing tested at the Outdoor Aerodynamic Research Facility of NASA Ames. Figures 3 and 4, taken from Ref. [2] and previously presented in Chapter 1, show typical wing surface pressures with and without tangential blowing and the variation of download/thrust with blowing pressure ratio, that were measured in this test. Significant differences exist between the experimental configuration and the current tilt rotor numerical model. Of particular note for this blowing analysis is the substantial difference in the shape of the airfoil section of the circulation-control model relative to the V-22 wing airfoil used in the numerical study. Also, in the experiment the rotor axis was positioned above the wing centerline, not the wing tip. Direct comparisons of quantitative results, therefore, must be made with some caution. The general effects of blowing on wing surface pressures and the behavior of download versus increasing plenum pressure, however, are discussed and compared below.

The numerical results reported here are for a rotor with uniform disk loading and no swirl. It is expected that the effect of blowing on wing download is similar for both rotor models, and that the conclusions drawn from the results discussed below apply also to the case where the rotor disk is non-uniformly loaded and imparts swirl.

The computations discussed below are all for a uniform rotor disk loading of $\Delta p/p_\infty = 0.0085$ which, assuming a typical rotor tip Mach number equal to 0.72, represents a typical rotor thrust coefficient $C_T = 0.0117$. In Ref. [2], Felker and Light report that there is little effect of thrust coefficient on the reduction of download at thrust coefficients above 0.007. It is expected, then, that the numerically computed results for download reduction at $C_T = 0.0117$ are essentially the same as what would be computed for a range of C_T's up to and beyond $C_T = 0.0164$ (that was specified in computations previously described). As mentioned in previous discussions of the modeling of the jet (see Section 4.4), the jet is positioned at the wing leading edge ($x/c = 0.0$) and runs the length of the wing semi-span. The jet velocity is imparted vertically downwards. The work of Ref. [2] shows that the slot height has little effect on the download. Therefore, a representative height of 0.2% of wing chord is selected and kept unchanged for all the computations. As discussed in Section 5.3.1, there is only a small amount of unsteadiness predicted by the the numerical solution. Nevertheless, all results shown below, except where otherwise noted, are time-averaged over one period of oscillation of download.

Figure 45 shows two close-up views of the computed flowfield around the wing leading edge at a typical spanwise location, $2y/b = 0.7$. Figure 45(a) shows the velocity vectors for a case with no blowing. Figure 45(b) is an identical case but with leading edge tangential blowing specified with a pressure ratio $p_p/p_\infty = 1.04$. Note that the velocity vectors are not drawn to the same scale in both cases. The entrainment of the flow outside the jet is clearly seen in the changing velocity profiles beneath the leading edge. The jet has also caused the separation point to be shifted slightly further aft of the leading edge on the lower surface. Note also that by delaying separation, the outer flowfield wraps around the leading edge more than without blowing. This reduces the width of the separated wake region beneath the wing. This is more clearly observed in Fig. 46. The instantaneous particle traces (as mentioned before, there is very little computed unsteadiness, so these pictures vary little with time) are generated by particles seeded in the flowfield above the wing. Theoretically, assuming in a potential flow that the wake would be reduced to zero width, the pressures, then, would increase on the lower surface reaching stagnation pressure

in the mid-chord region. The resulting pressure drag would be zero. One would expect then, that movement of the separation location further aft, which reduces the width of the wake, would increase the base pressure, thereby reducing the download. From the computed pressures, however, it appears that although the separation point movement due to blowing is sufficient to have significant impact on the wake width, it has very little effect on the base pressure on the wing lower surface. Nevertheless, a reduction of download/thrust of 7% is computed for this case. The effect of the static pressure reduction in the jet due to surface curvature (caused by a balancing of pressure with the centrifugal force) is felt upstream causing a flow acceleration (and corresponding pressure drop) even before the jet is reached. Figure 47 shows the computed wing surface pressures at $2y/b = 0.7$ with and without blowing. Aft of about 30% chord on the upper surface and about 10%c on the lower surface, blowing has virtually no effect on the wing surface pressures. On the lower surface near the leading edge, blowing is seen to reduce the static pressure and, therefore, it actually contributes to the download. The magnitude and chordwise extent of the reduction in pressures on the upper surface, however, is greater than on the lower surface, thereby resulting in a net reduction in download. The jet tends to reduce the region of near-stagnated flow on the upper surface. These observations are similar to those of Felker and Light [2] who, as mentioned in Section 1.2.1, found experimentally that most of the download reduction is due to the reduction of pressure on the wing upper surface near the leading edge.

Figure 48 shows the behavior of download/thrust with plenum blowing pressure ratio. The pressure ratio p_p/p_∞ is varied from 1.00 (no blowing) to 1.12. This corresponds to a variation in blowing momentum coefficient C_μ (refer to definition Eq. 61) from 0.0 to about 0.10. As p_p/p_∞ is increased to 1.04, the download continues to drop. As the plenum pressure is increased further, DL/T begins to increase again. As mentioned in Section 1.2.1, this behavior was also observed in the experimental tests of Ref. [2]. The experimental results (refer to Fig. 4 in Chapter 1) show a greater reduction in download due to blowing than is computed — about 17% compared to 7%. Also, the optimum blowing pressure ratio for minimum download is about 1.08 for the experiment and about 1.04 found numerically. Considerable differences

between the computed and experimental results are to be expected. In addition to wing/rotor configuration differences, the constant radius of curvature of the leading edge of the experimental model wing is more ideally suited to boundary layer control. The flow is able to remain attached further aft of the leading edge on the lower surface. This delays flow separation, which as mentioned earlier, tends to increase the base pressure on the lower surface somewhat, thereby contributing to download reduction. In addition, the slot location on the circulation-control wing was at 3% chord which provided a potentially greater pressure reduction on the wing upper surface than for the numerical model where the slot location was fixed at $x/c = 0.0$. The increase in download beyond a pressure ratio of 1.04, as seen in Fig. 48, is due to the increasing jet velocity as the blowing pressure is increased. The jet, following the curved lower surface in the region just aft of the wing leading edge, causes a decrease in local pressure. This increased negative pressure on the lower surface near the leading edge offsets the pressure reduction on the upper surface, and the download increases.

Figure 49 shows the wing surface pressures on the leading edge of the wing at a spanwise location $2y/b = 0.15$ — outside of the rotor downwash (the edge of the rotor disk lies at $2y/b = 0.19$). The previously-described effect of increasing blowing is clearly shown. With blowing at $p_p/p_\infty = 1.04$, the extent of the wing chord where the pressure on the upper surface is less than on the lower surface, is greater than it is when there is no blowing — this produces a local upload. There is a region inboard of $x/c = 0.01$, however, where the surface pressures cross, introducing a small amount of download. As will be seen below, there is a small net download reduction with $p_p/p_\infty = 1.04$ relative to the download with no blowing (i.e. $p_p/p_\infty = 1.00$). From Fig. 49 it can be seen that increasing the plenum pressure ratio further to 1.08 causes the lower surface pressure to be less than the upper surface pressure along the full length of the leading edge region. It is easy to see that the download is greatest with this level of blowing.

Further outboard on the wing, the rotor downwash and wing wake affect the results. Figure 50 shows the pressure distributions near the leading edge at a spanwise location of $2y/b = 0.7$. At this location, increasing plenum pressure ratio to 1.04 and 1.08 causes the download to be continuously reduced as the chordwise extent and

the magnitude of lower surface pressure minus upper surface pressure increases. This occurs in spite of the increasing magnitude of local download close to the leading edge where the upper and lower surface pressures cross. The presence of a strong wing wake beneath that portion of the wing totally immersed in the rotor slipstream reduces the region of influence of the jet on the lower surface. For a pressure ratio of 1.08, the jet affects the lower surface pressures to about $x/c = 0.10$ at $2y/b = 0.7$ compared to about $x/c = 0.30$ at $2y/b = 0.15$. As can be seen from Fig. 50, the increase in plenum pressure causes a slight increase in base pressure. This was also seen in the experimental results of Ref. [2].

From the above results, it is seen that the effect of blowing varies with spanwise location along the wing. This is more clearly observed in Fig. 51 which shows the time-averaged local download per unit span for a range of blowing pressures. Increasing the plenum pressure above the optimum required for minimum wing download increases the local download on the inboard region of the wing, while reducing it on the outboard region. Tailoring the jet velocity along the span, then, could have a significant impact on download reduction. The jet velocities (and corresponding plenum pressures) should be greater on the outboard portion of the wing (within the rotor wake) than on the inboard region (outside of the rotor wake). In the light of these observations, the greater optimum plenum pressure found experimentally can be explained, at least in part, by the fact that the entire model wing is immersed in the rotor flowfield. Another interesting observation from Fig. 51 is that increasing the plenum pressure in the region of the fountain flow at the wing centerline reduces the local download. It appears that the entrainment of the outer flow by the jet helps somewhat in reducing the strength of the vertical flow in the fountain. The local dip and oscillations in the download per unit span near the wing tip are most likely due to insufficient resolution of the flowfield at the tip. Further grid refinement would be required in order to compute the tip flow more accurately.

5.5 Summary of Results

The numerical method developed during the course of this work, and described in the previous chapters, is able to predict many of the important flow features of the rotor alone and of the tilt rotor in hover.

The numerical model of the rotor allows the computation of the mean features of the rotor flowfield without performing a detailed analysis about the individual blades. The flow acceleration from a quiescent state far above the rotor disk towards and through the rotor is computed. The maximum velocity in the wake occurs below the rotor, as expected, where freestream pressure is recovered. For the case of a uniformly-loaded rotor disk with no swirl, the maximum computed dynamic pressure in the wake, derived from simple momentum theory, is verified by the numerical solution. Results with the non-uniform rotor disk model with swirl were compared with experimental data from a test of a model V-22 rotor. Although they differ somewhat, the computed induced velocities in the wake approximate the measured values. The numerical method predicts the effect of rotor thrust coefficient on the radial distribution of downwash. As C_T increases, the rotor downwash becomes greater in the outer region than in the inner region of the wake (due to the increased blade loading on the outer portion of the rotor disk). No experimental data exists to verify the magnitude of the computed swirl directly, but the shape of the computed wing upper surface pressure distributions, affected significantly by the swirl component in the rotor flowfield, matches fairly closely with that observed experimentally. Considering the simplifications involved in the rotor model, the figure of merit agrees very well with experimental measurements over a range of thrust coefficients. The contraction of the wake below the rotor is computed but the diameter of the streamtube is greater than expected. This and the computed non-distinct edge of the wake explain, in large part, the observed discrepancies with experiment. Both less-than-optimum grid point distributions (using a Cartesian grid for the rotor flowfield) and numerical diffusion due to large grid spacings contribute to inaccuracies in the solution.

The numerical computation of wing/rotor interaction allows the prediction of many of the complex tilt rotor flow features described in Chapter 1. The transition

from primarily chordwise flow to primarily spanwise flow further inboard on the wing upper surface is computed. The recirculation pattern referred to as the fountain flow is also predicted. The spanwise-moving flow is seen to be re-directed vertically upwards at the plane of symmetry and partially re-ingested into the rotor disk. The vertical extent of the fountain appears to be somewhat less than previous, limited, experimental flow visualization would indicate. The computation predicts the existence of a standing vortex beneath the wing tip, formed because of flow separation at the tip. The computed wing wake is characterized by vorticity shed from the leading edge and the trailing edge. A pair of counter-rotating vortices occur below the wing. There is very little computed unsteadiness in the solutions. The peak-to-peak variation of wing download, although cyclic with a fairly constant non-dimensional period (period normalized by c/a_∞) of about 24, is less than 2% of the mean value. The wing surface pressures compare reasonably well with the experimental results for a similar, but not identical, configuration. The agreement is good in the mid-span region but becomes worse in the wing tip and the wing root regions. The spanwise flow outboard over the tip and the diffusion of the edge of the wake, computed in the numerical solution, account for the discrepancies. The spanwise variation of wing download, however, follows the same general behavior as measured experimentally. The computation resolves the local increase in download in the region of the fountain. For the case where the rotor thrust coefficient is 0.0164 and the rotor tip Mach number is 0.72, the computed time-averaged download/thrust is 0.113. This is 20% – 30% higher than measured experimentally on configurations similar, but not identical to, the numerical model.

The numerical computation of the tilt rotor flowfield permits the study of the effect of rotor-induced swirl. The wing pressure distributions clearly show that swirl causes the location of maximum pressure on the upper surface to occur further forward, closer to the leading edge. Swirl also promotes flow separation on the flap in the region of chordwise flow on the wing. Although this tends to increase the local download, the total download is reduced due to the presence of swirl. The effective angle of attack that the wing sees is increased. For the uniform rotor disk with no swirl, at a rotor thrust coefficient of 0.0164, the computed time-averaged download/thrust is 0.129.

The computed DL/T with non-uniform rotor disk loading and swirl, then, is 12% less than with uniform rotor loading without swirl.

The numerical method is also capable of predicting the effect of the wing on the flow through the rotor. The blockage effect of the wing causes a reduction in induced velocities in that portion of the rotor disk that lies immediately above the wing. The local effective angle of attack on the rotor blades increases, which in turn, produces an increase in local rotor loading (pressure rise) of about 6% for the case computed where $C_T = 0.0164$.

Leading edge tangential blowing is seen, from the computational results, to delay separation to a location a small distance further aft on the wing lower surface, thereby reducing the width of the wing wake. The resulting base pressure, however, is increased only very slightly. Flow entrainment by the jet causes an acceleration of the flow on the wing upper surface near the leading edge, with a subsequent reduction in static pressure. This is the primary contribution to download reduction. There exists an optimum constant blowing pressure for minimum download. Blowing above this amount causes the lower surface pressure reduction to exceed that of the upper surface, thereby increasing the download. The optimum blowing pressure for the case where the rotor is uniformly-loaded with no swirl and $C_T = 0.0164$ is computed to be 1.04 (corresponding to $C_\mu \approx 0.043$). The corresponding download reduction is computed to be 7%. The computation shows that the local effect on download reduction varies with position along the wing due to the spanwise-changing flowfield.

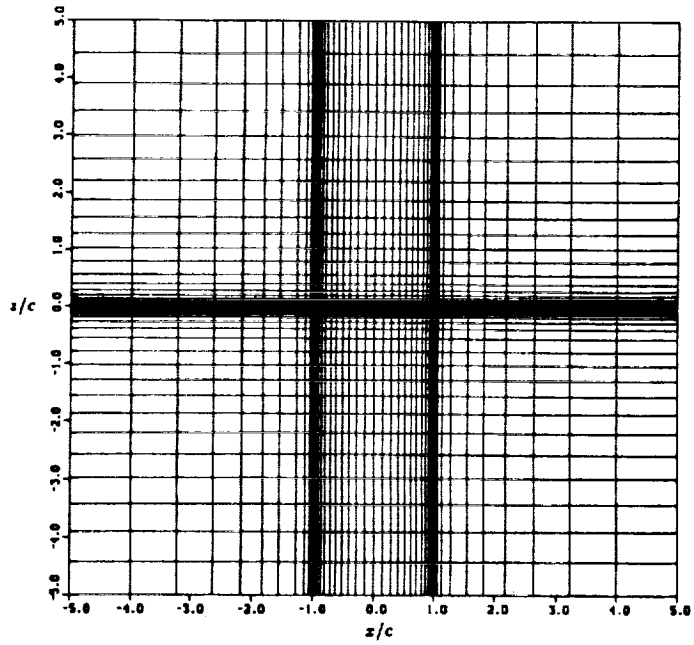

(a) Vertical cut through the center of the Cartesian grid.

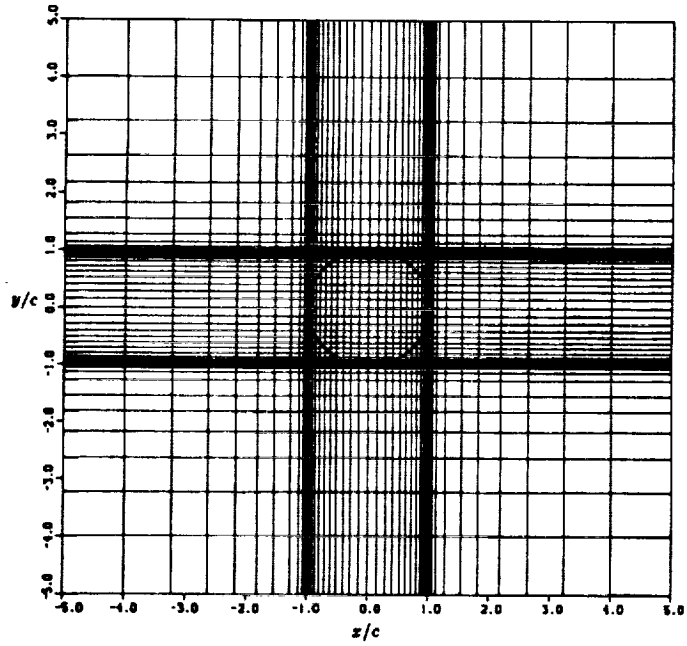

(b) Horizontal cut through the center of the Cartesian grid.

Figure 13: Two views of the Cartesian grid used for the rotor alone computations.

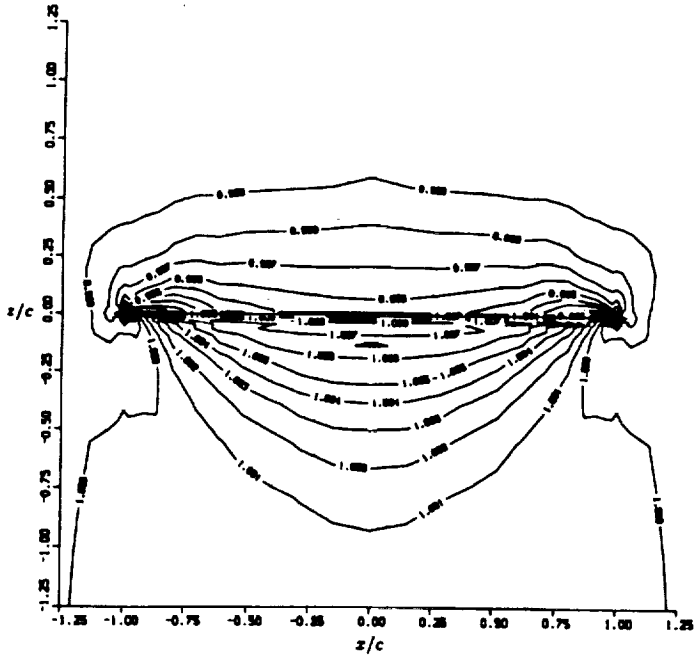

Figure 14: Contours of pressure in a vertical plane through the rotor for a uniformly-loaded rotor with $C_T = 0.0164$.

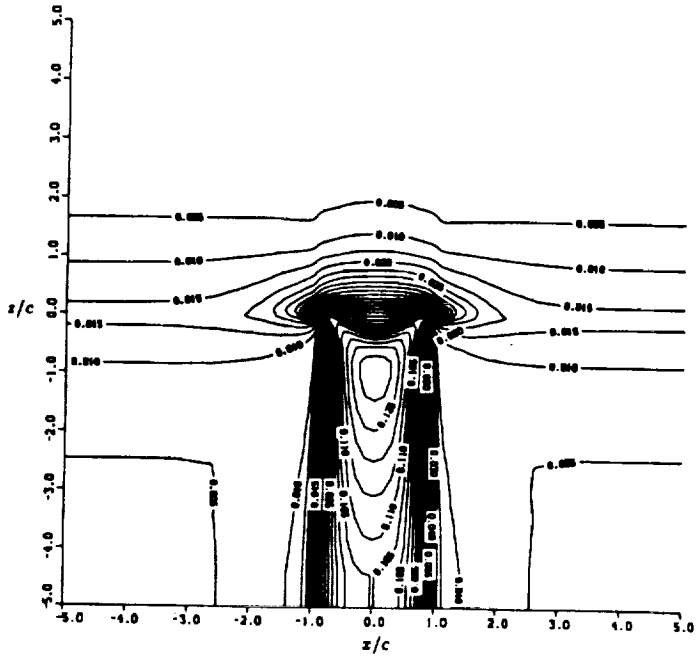

Figure 15: Contours of velocity magnitude in a vertical plane through the rotor for a uniformly-loaded rotor with $C_T = 0.0164$.

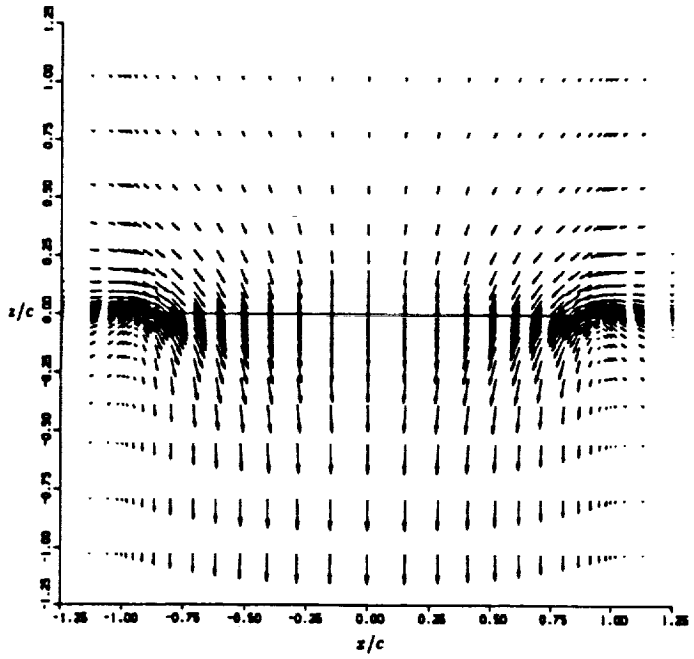

Figure 16: Velocity vectors in a vertical plane through the rotor for a uniformly-loaded rotor with $C_T = 0.0164$.

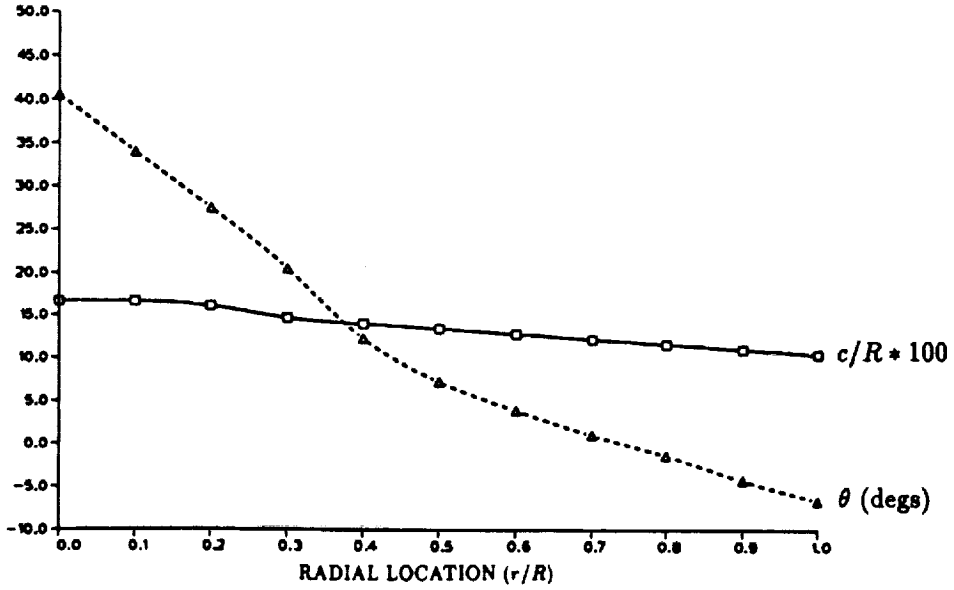

Figure 17: The blade chord and twist distributions used for the non-uniformly-loaded rotor model.

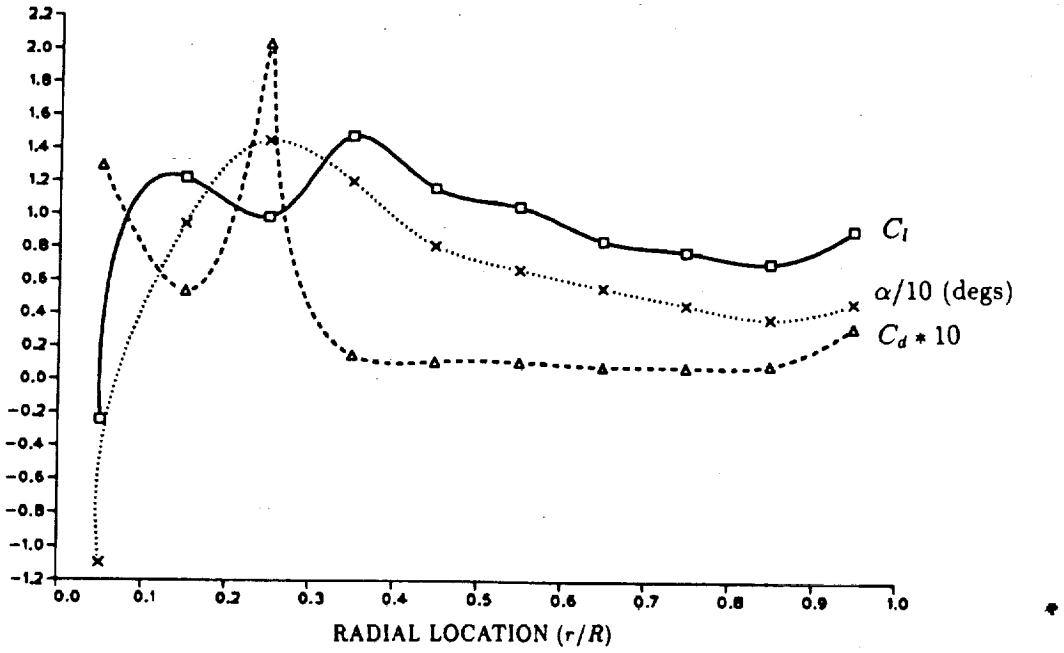

Figure 18: Radial distributions of blade loading and angle of attack for a non-uniformly-loaded rotor with $C_T = 0.0164$.

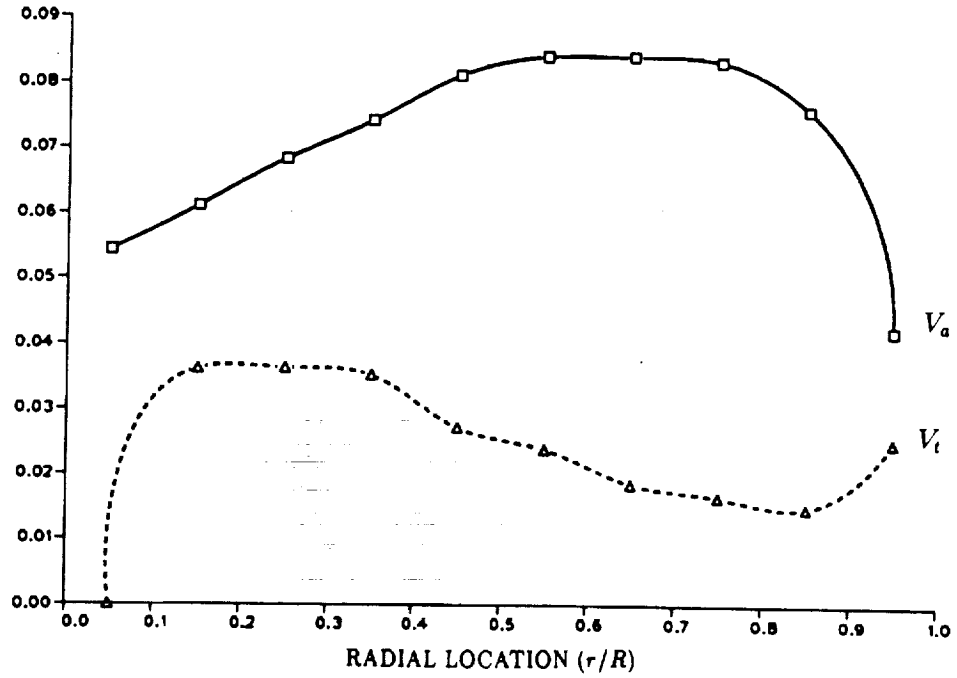

Figure 19: Radial distributions of axial velocity V_a and swirl velocity V_t at the rotor disk for a non-uniformly-loaded rotor with $C_T = 0.0164$.

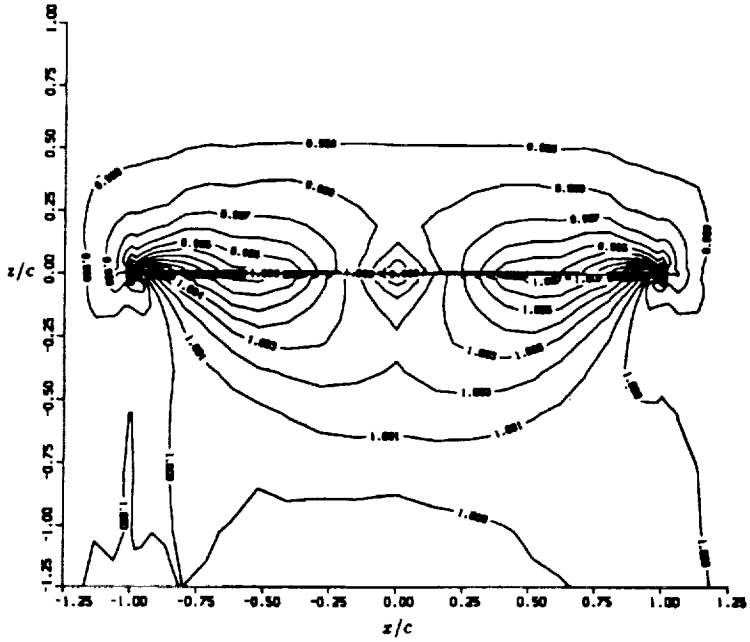

Figure 20: Contours of pressure in a vertical plane through the rotor for a non-uniformly-loaded rotor with $C_T = 0.0164$.

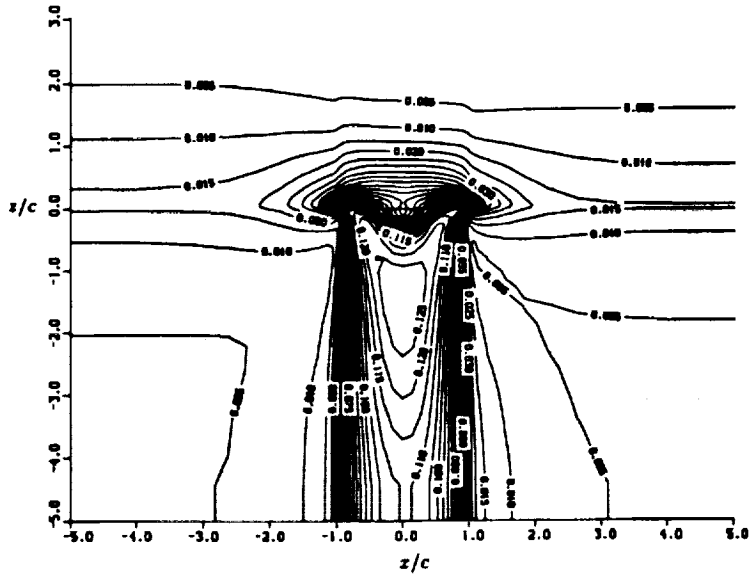

Figure 21: Contours of velocity magnitude in a vertical plane through the rotor for a non-uniformly-loaded rotor with $C_T = 0.0164$.

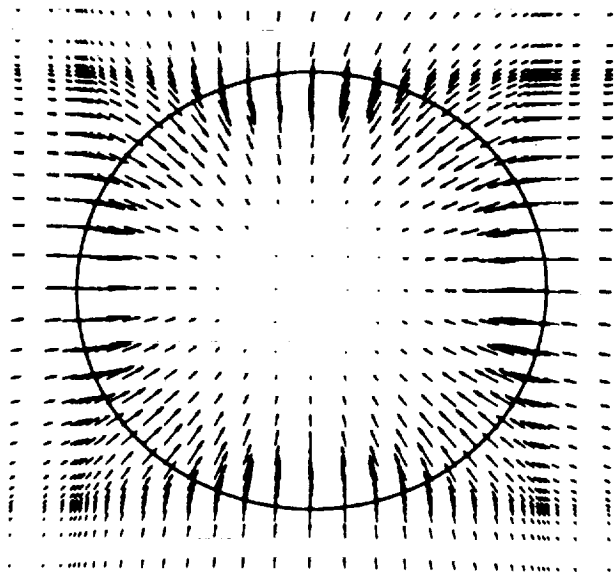

(a) Immediately above rotor.

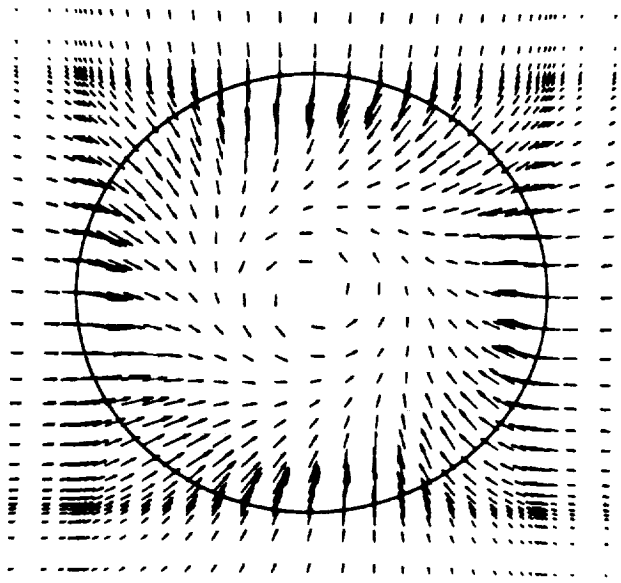

(b) Immediately below rotor.

Figure 22: Top view of the velocity vectors projected onto horizontal planes immediately above and below the rotor for a non-uniformly-loaded rotor computation.

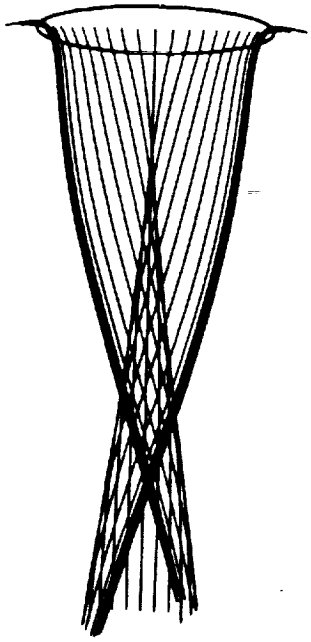

(a) Side view.

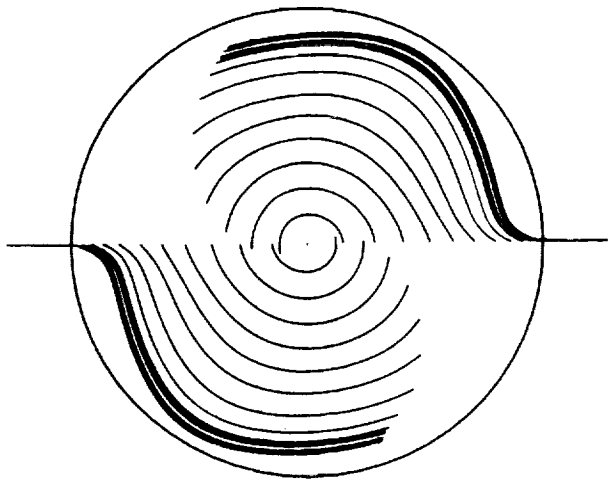

(b) Top view.

Figure 23: Two views of the particle traces in the flowfield below a non-uniformly-loaded rotor.

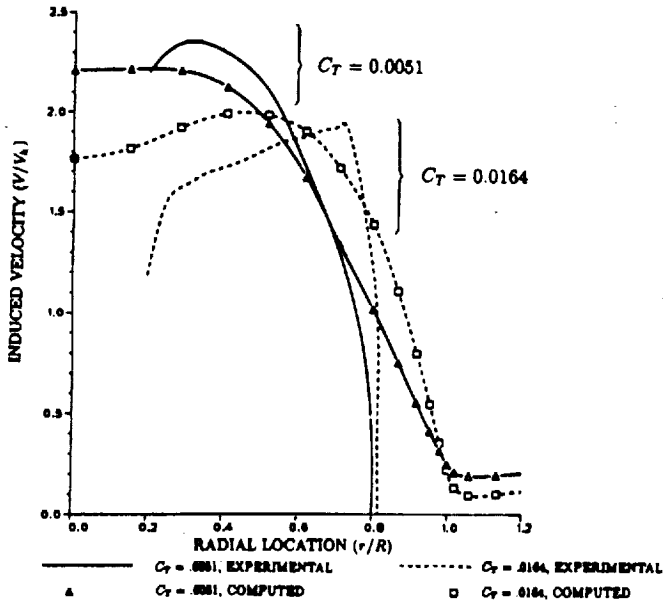

Figure 24: Comparison of calculated and measured induced velocities about one wing chord below the rotor disk.

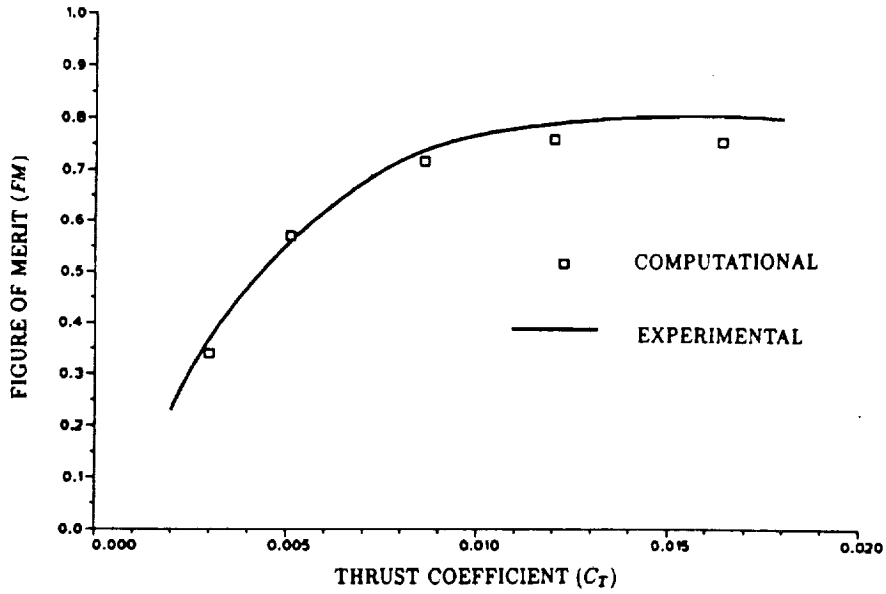

Figure 25: Comparison of calculated and measured values of figure of merit for a range of thrust coefficients, for a rotor alone.

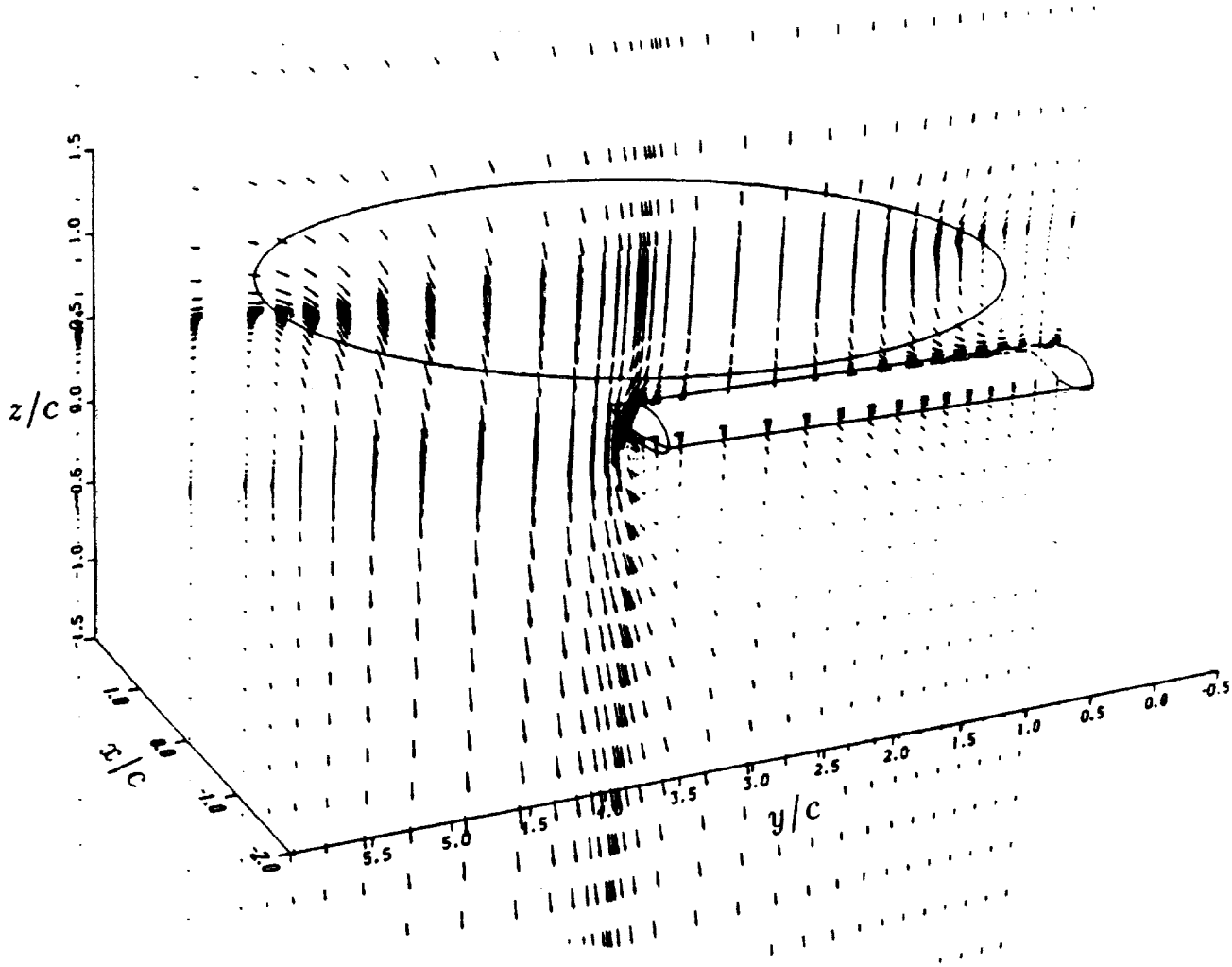

Figure 26: Perspective view of the velocity vectors for wing/rotor interaction with uniform rotor disk loading — in a near-vertical plane running spanwise through the wing mid-chord.

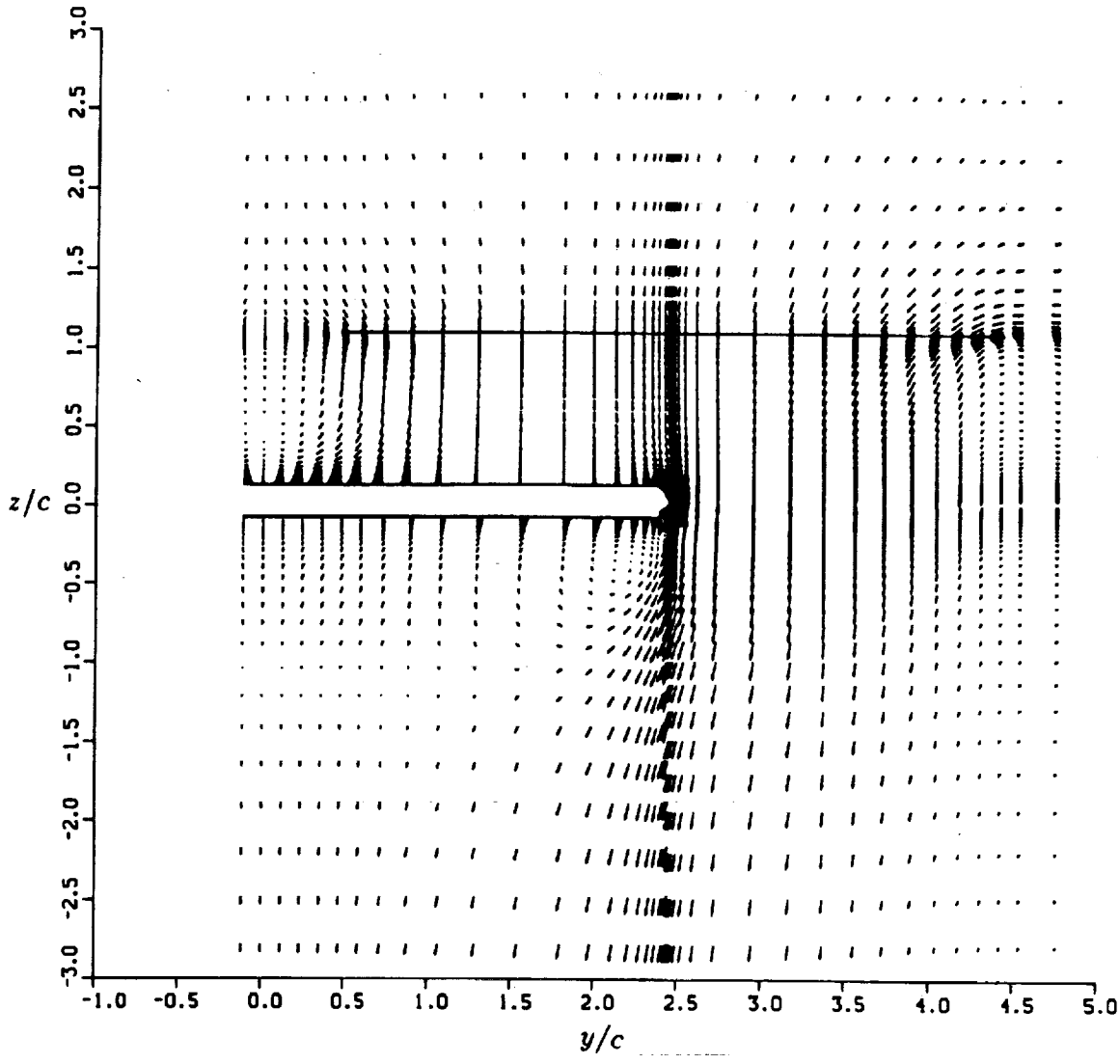

Figure 27: Velocity vectors in a vertical plane running spanwise through the wing mid-chord, for uniform rotor disk loading.

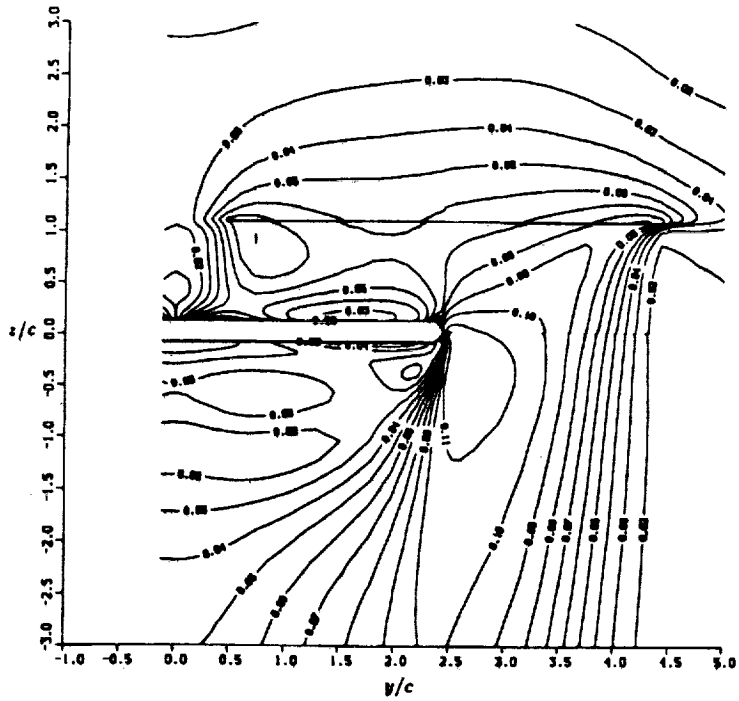

Figure 28: Contours of velocity magnitude in a vertical plane running spanwise through the wing mid-chord, for uniform rotor disk loading.

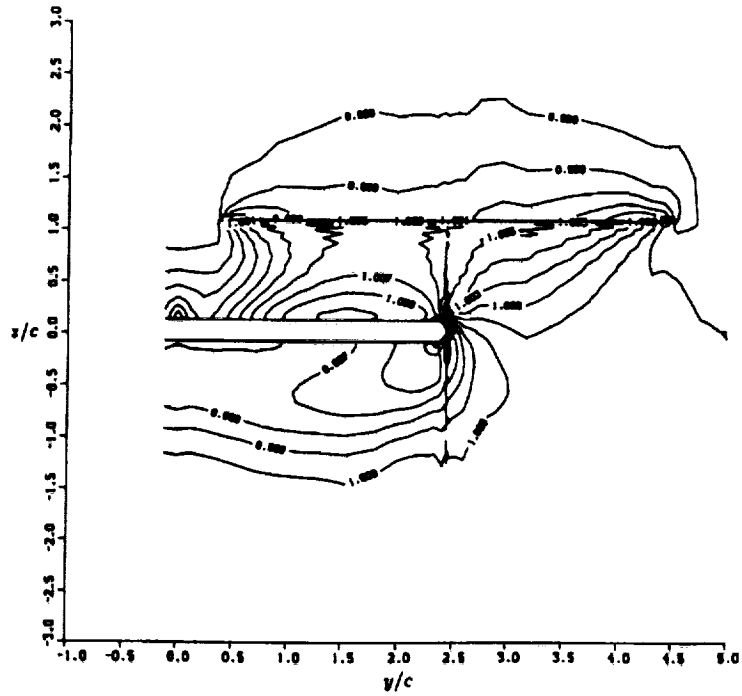

Figure 29: Contours of pressure in a vertical plane running spanwise through the wing mid-chord, for uniform rotor disk loading.

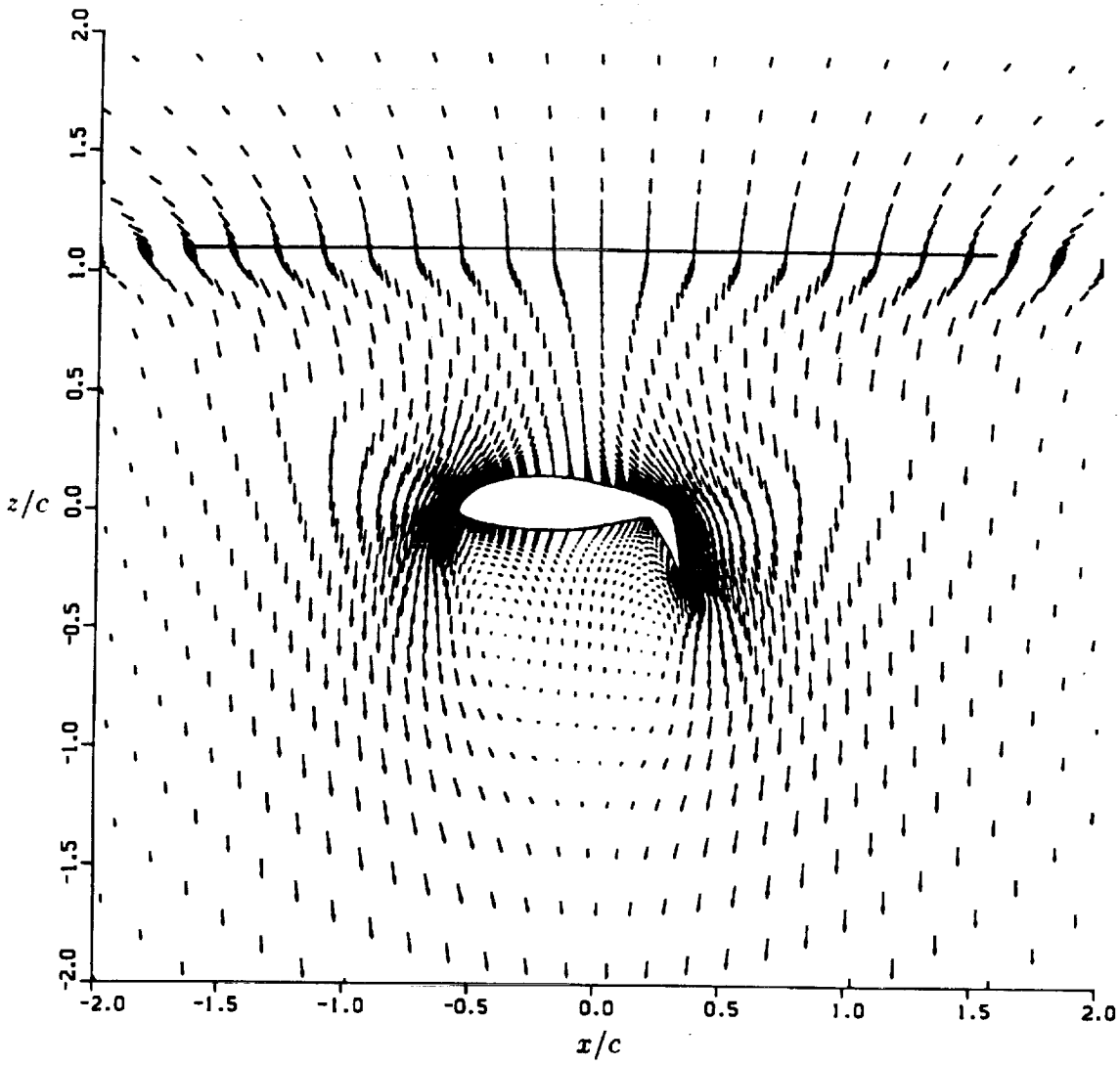

Figure 30: Velocity vectors in a vertical plane running chordwise through $2y/b = 0.7$, for uniform rotor disk loading.

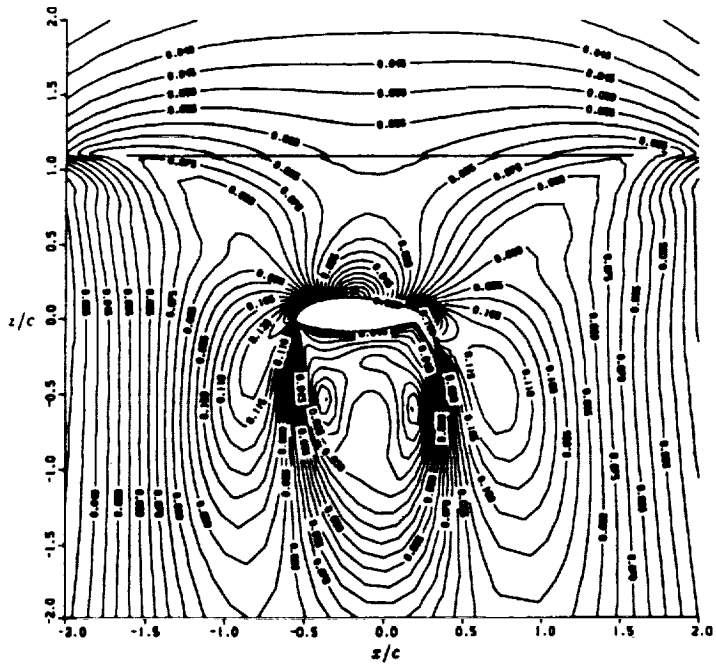

Figure 31: Contours of velocity magnitude in a vertical plane running chordwise through $2y/b = 0.7$, for uniform rotor disk loading.

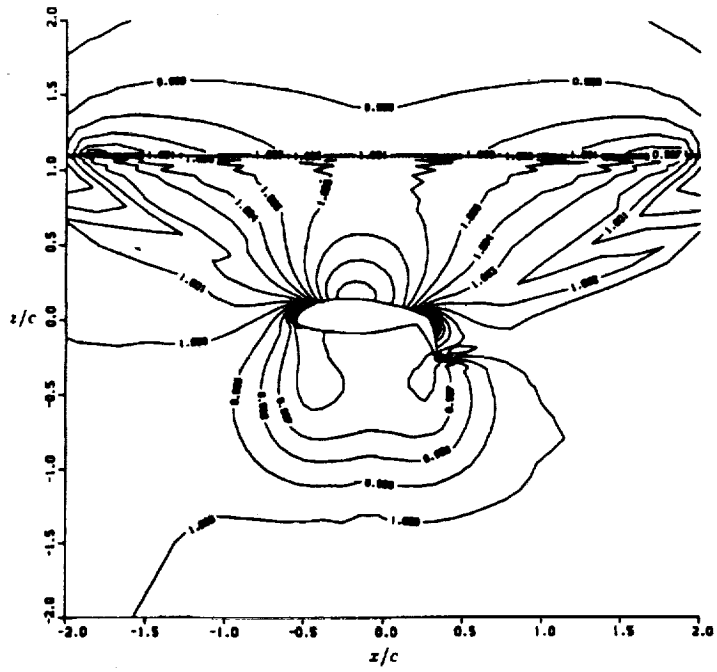

Figure 32: Contours of pressure in a vertical plane running chordwise through $2y/b = 0.7$, for uniform rotor disk loading.

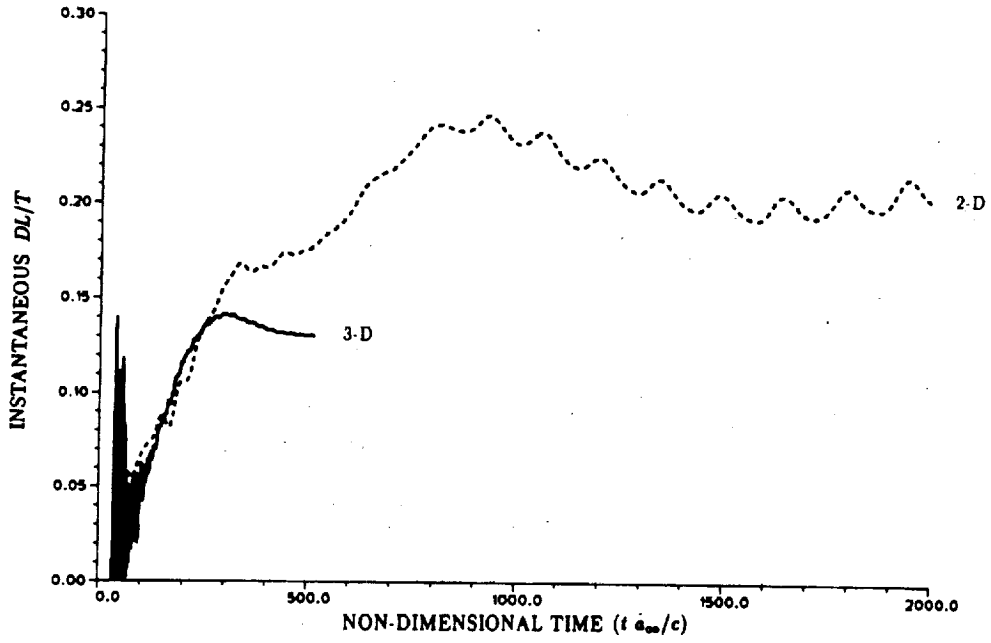

Figure 33: Comparison of the time history of the ratio download/thrust between two- and three-dimensional computations.

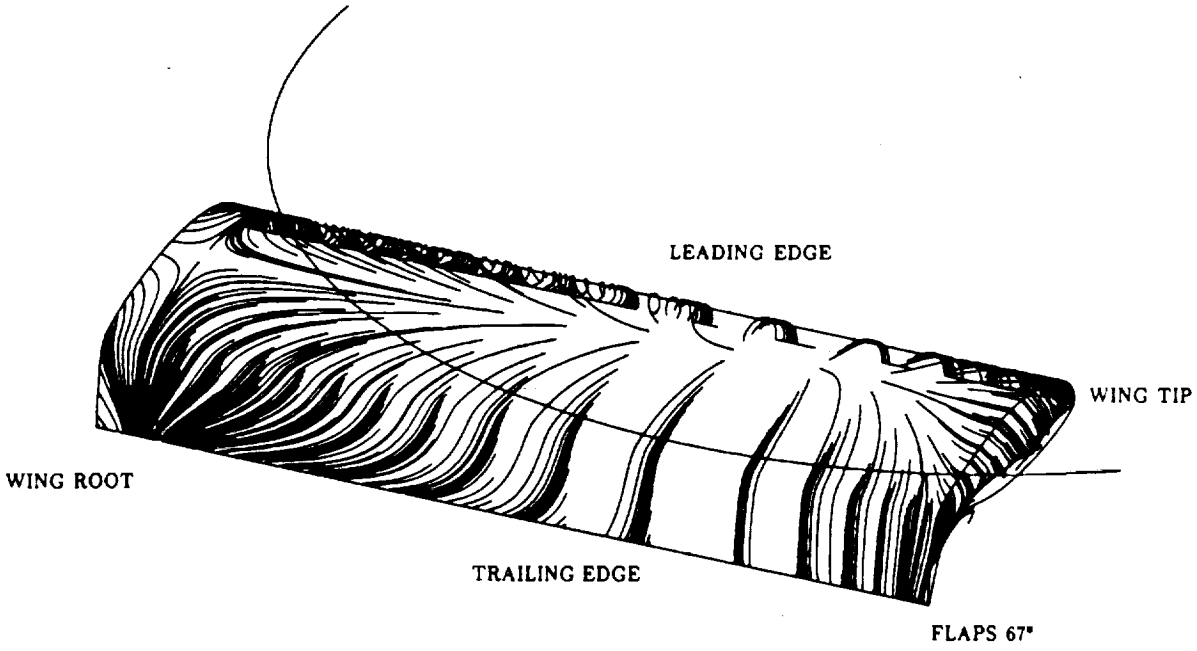

Figure 34: The computed oil flow pattern on the wing upper surface, for uniform rotor disk loading.

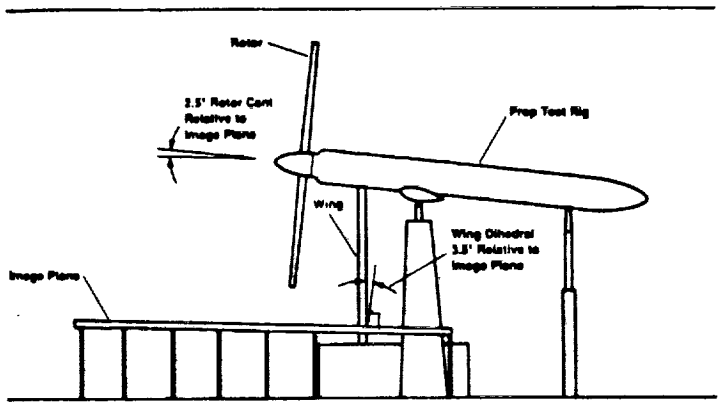

(a) Side view.

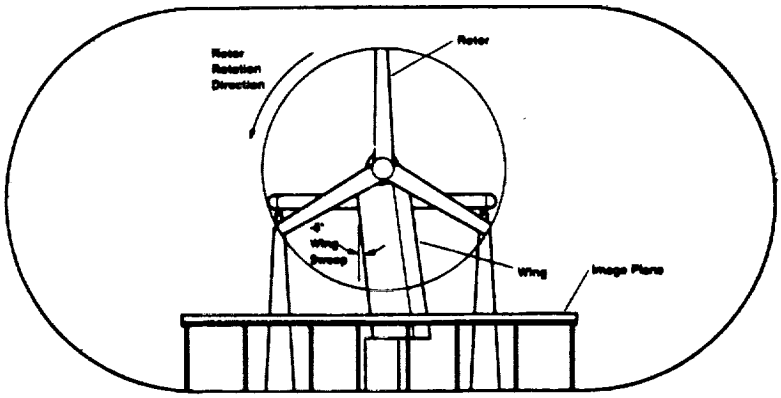

(b) Front view.

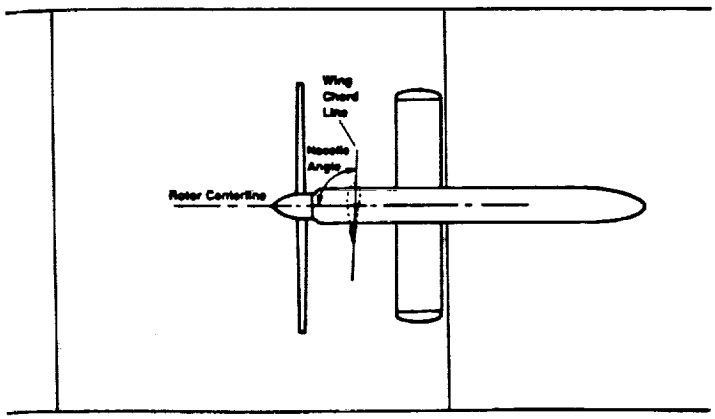

(c) Top view.

Figure 35: Schematic of installation of the 0.658-scale V-22 wing and rotor in the NASA Ames 40- by 80-Foot Wind Tunnel (taken from [10]).

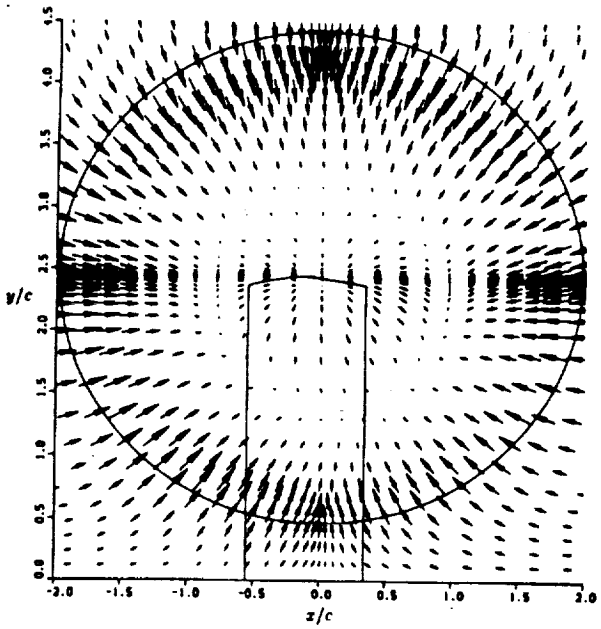

(a) Immediately above rotor.

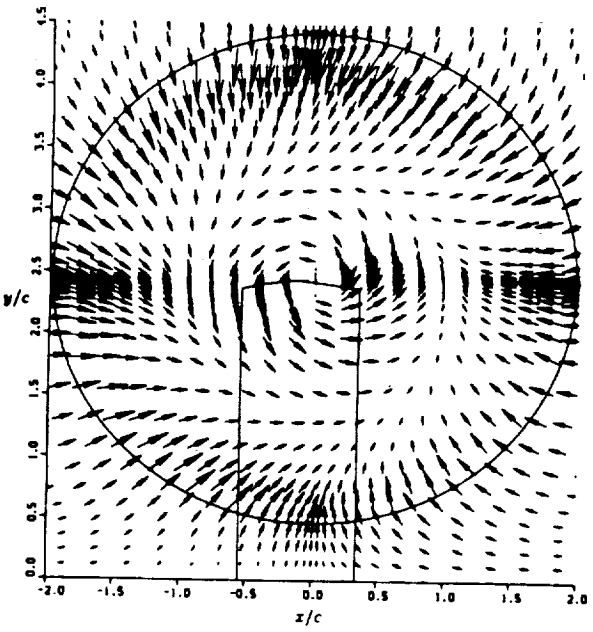

(b) Immediately below rotor.

Figure 36: Top view of the velocity vectors projected onto horizontal planes immediately above and below the rotor for a wing and non-uniformly-loaded rotor computation.

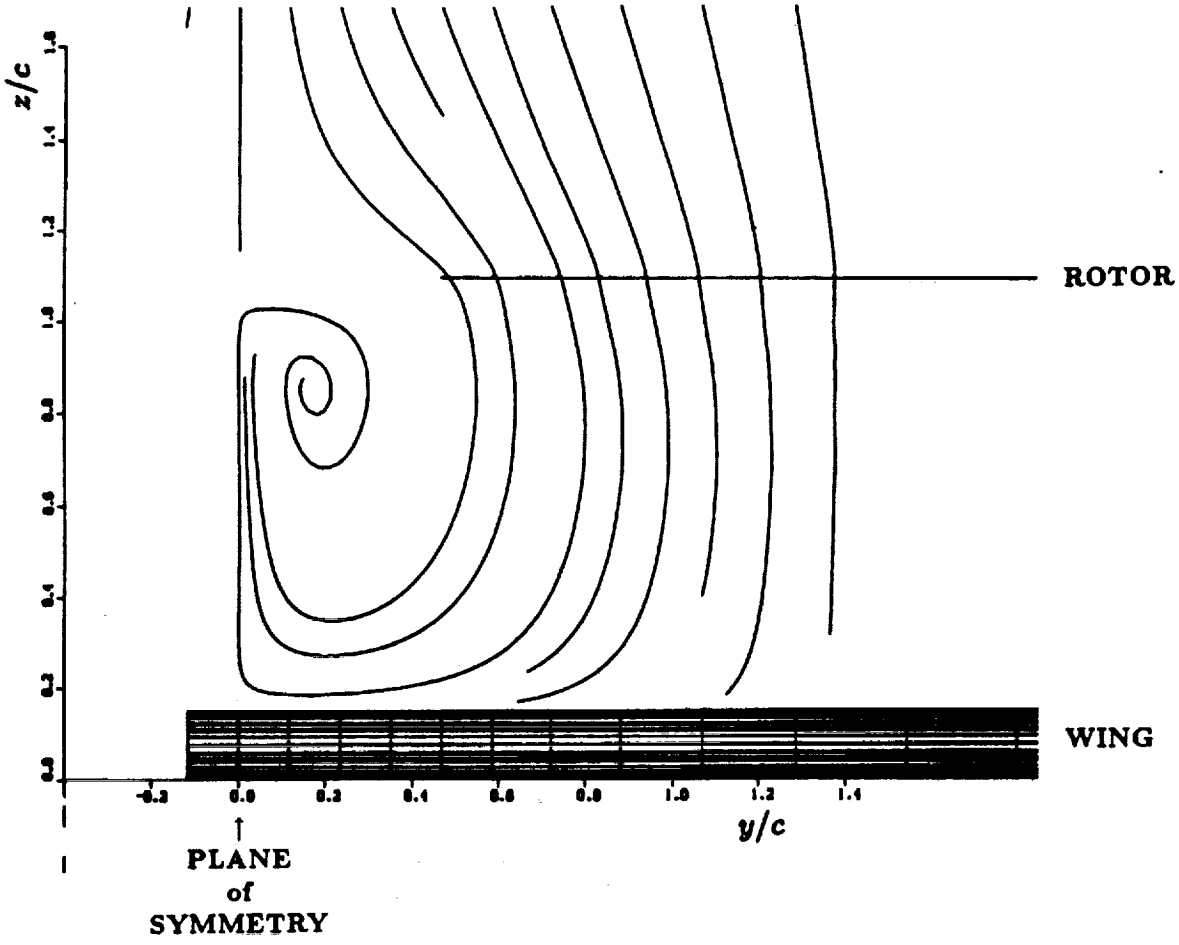

Figure 37: The instantaneous particle traces in a near-vertical plane in the wing root region showing the fountain flow, for non-uniform rotor disk loading.

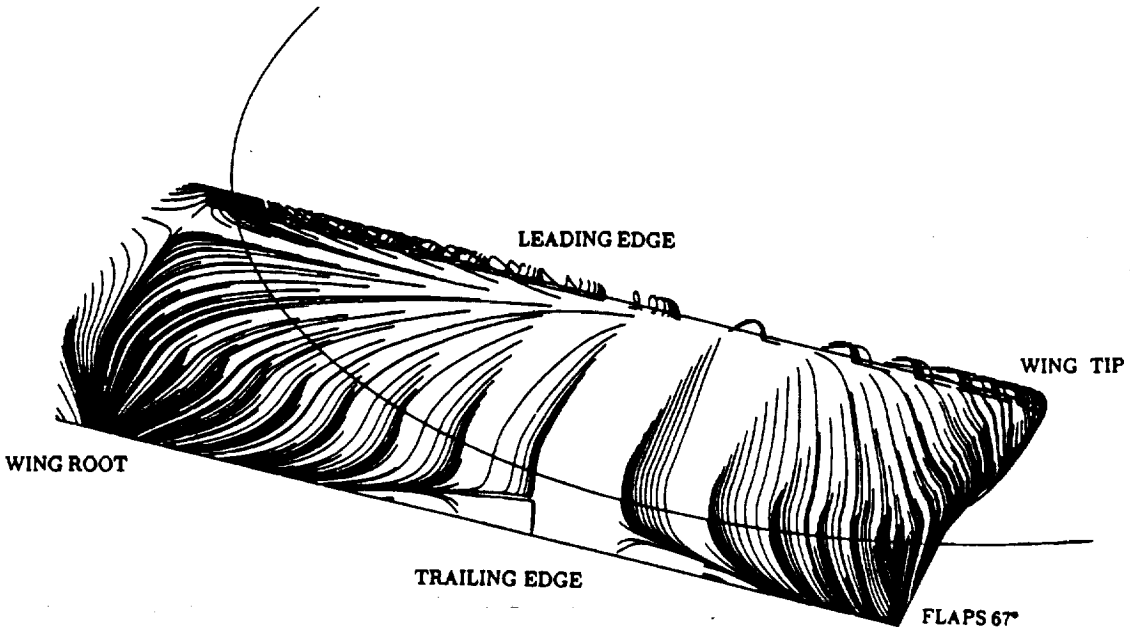

Figure 38: The computed oil flow pattern on the wing upper surface, for non-uniform rotor disk loading.

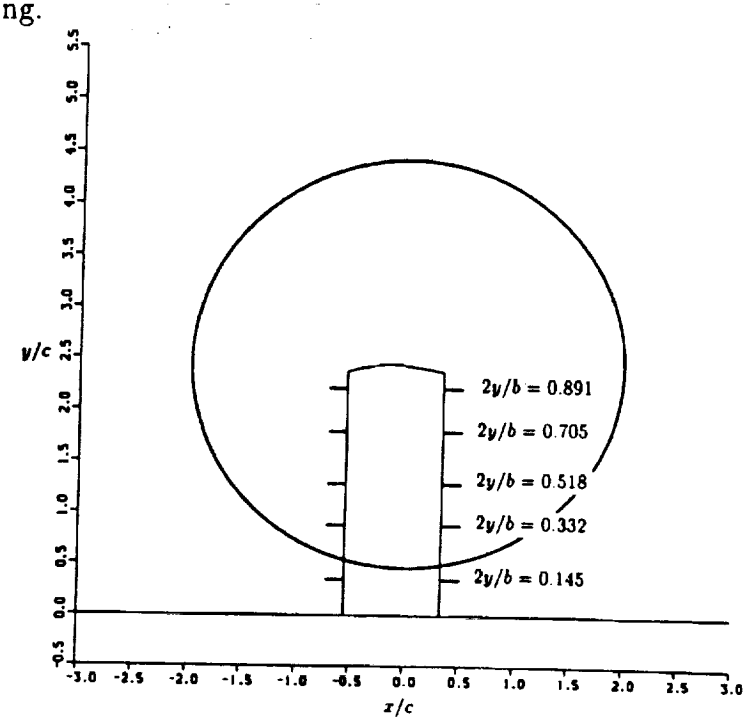

Figure 39: Sketch of the wing and rotor as seen from above, showing various spanwise locations referred to in the discussion.

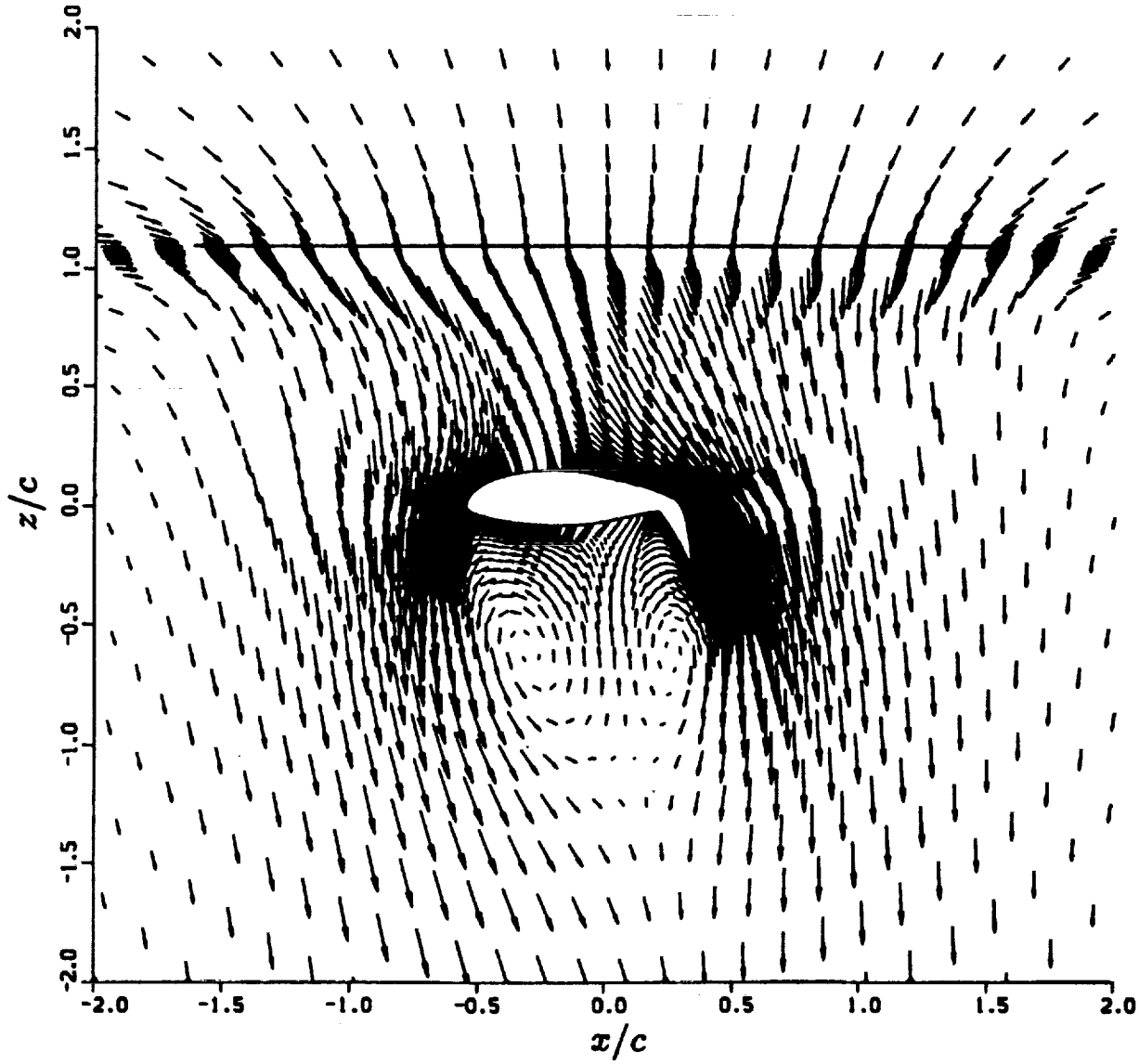

Figure 40: Velocity vectors in a vertical plane running chordwise through $2y/b = 0.7$, for non-uniform rotor disk loading.

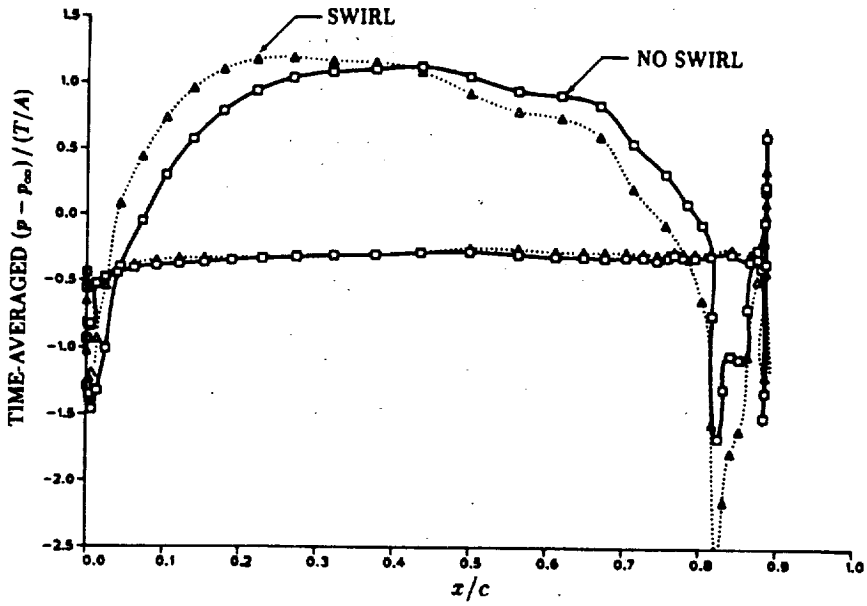

Figure 41: Comparison of wing surface pressures at $2y/b = 0.7$ showing the effect of swirl.

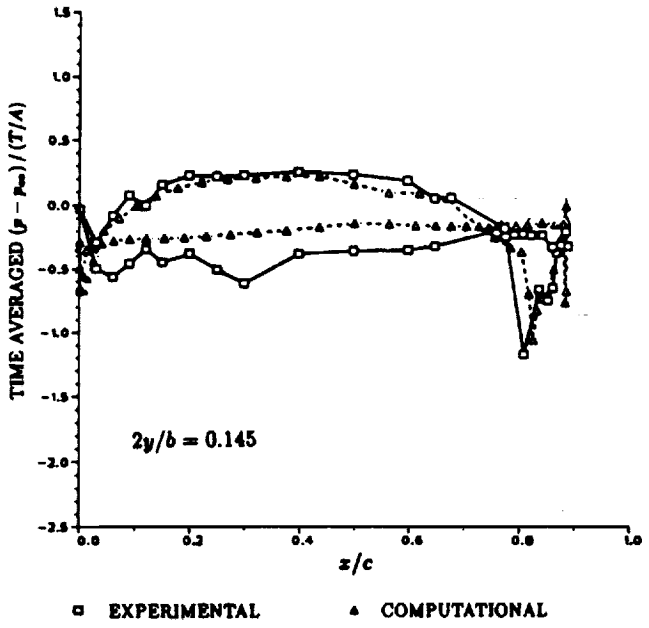

(a) $2y/b = 0.145$

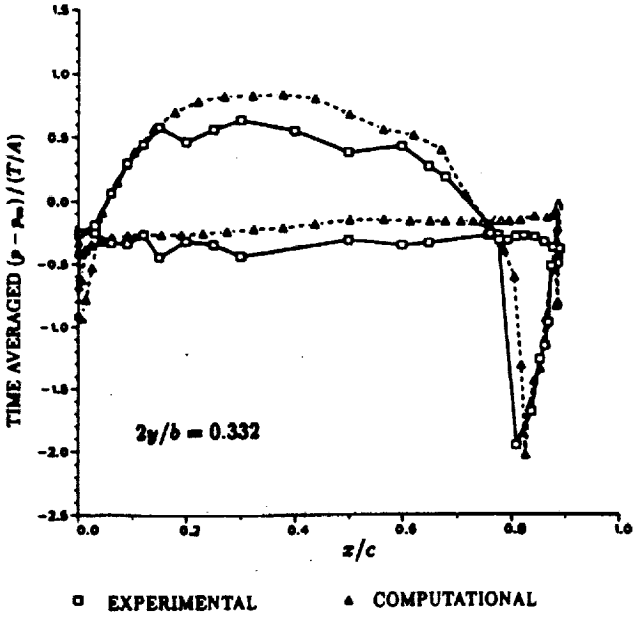

(b) $2y/b = 0.332$

Figure 42: Computed wing surface pressures compared with experimental results, for non-uniform rotor disk loading.

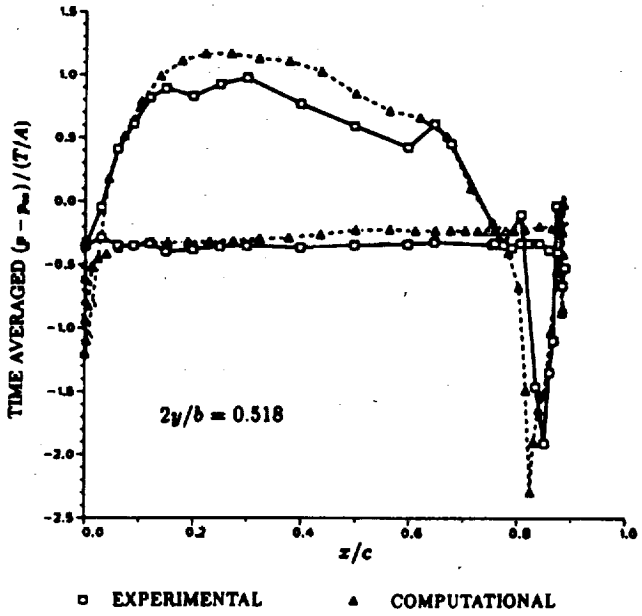

(c) $2y/b = 0.518$

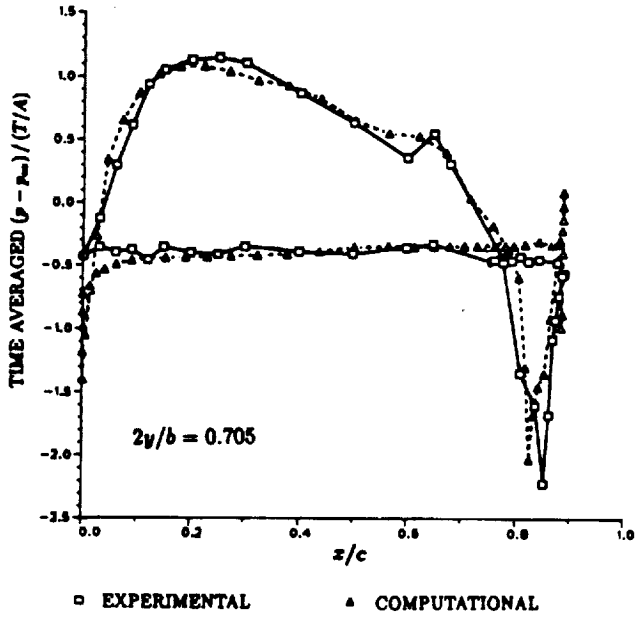

(d) $2y/b = 0.705$

Figure 42: Continued.

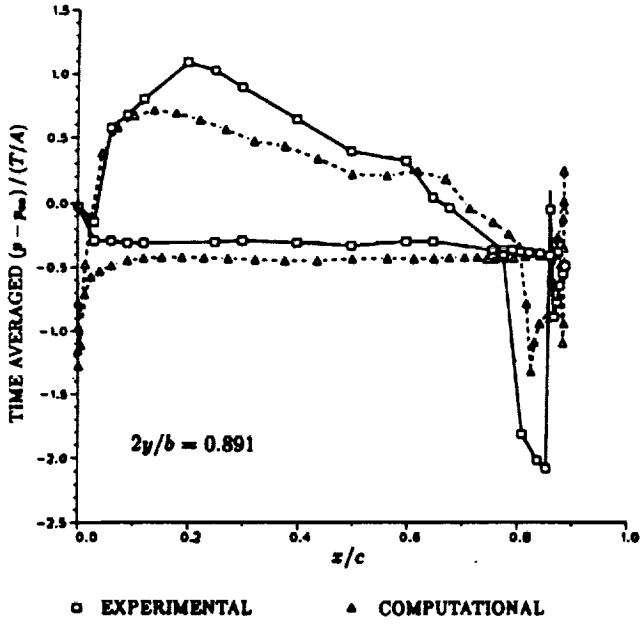

(e) $2y/b = 0.891$

Figure 42: Concluded.

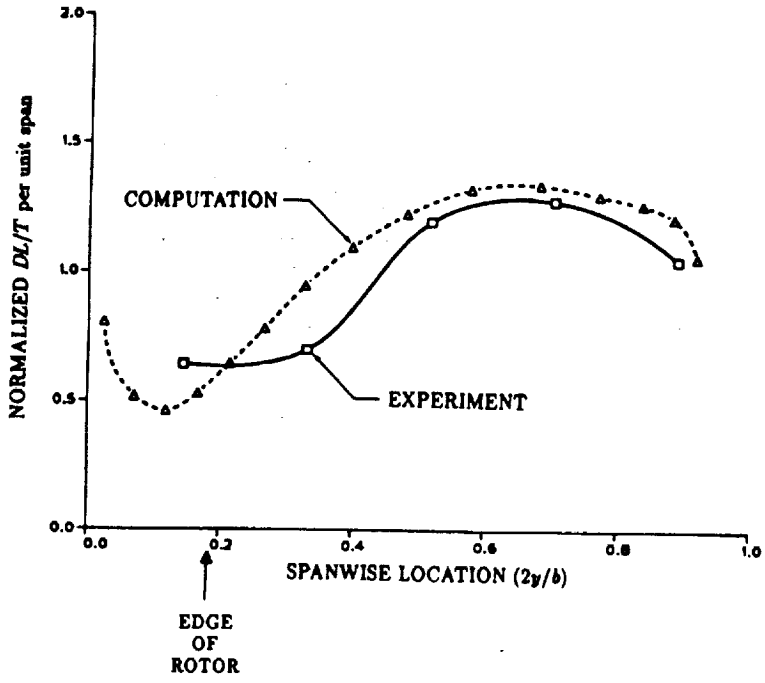

Figure 43: Comparison between computed and measured values of the normalized, time-averaged download/thrust per unit span.

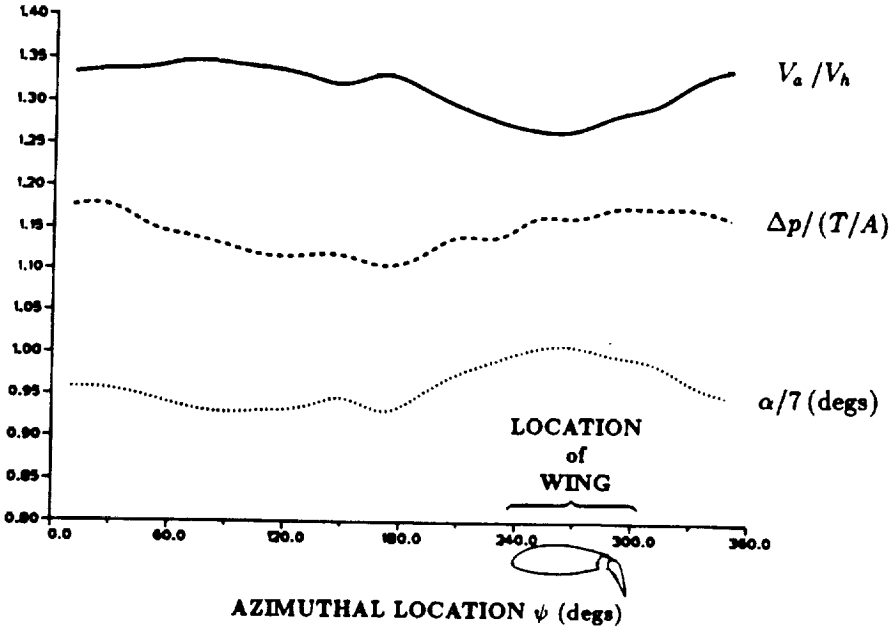

Figure 44: The azimuthal variation of several parameters shows the influence of the wing on the flow at the rotor disk at $r/R = 0.60$.

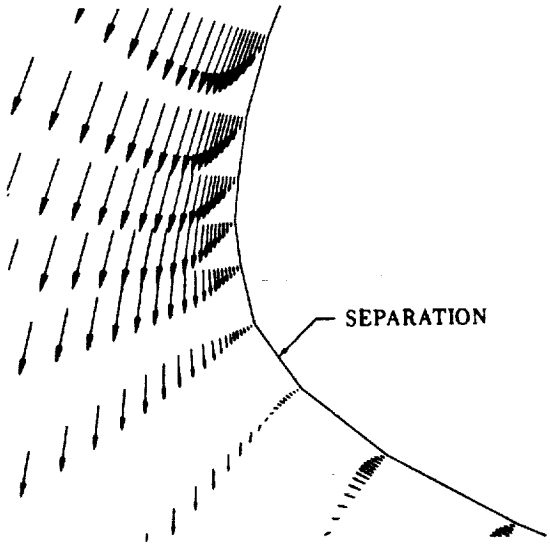

(a) With no blowing.

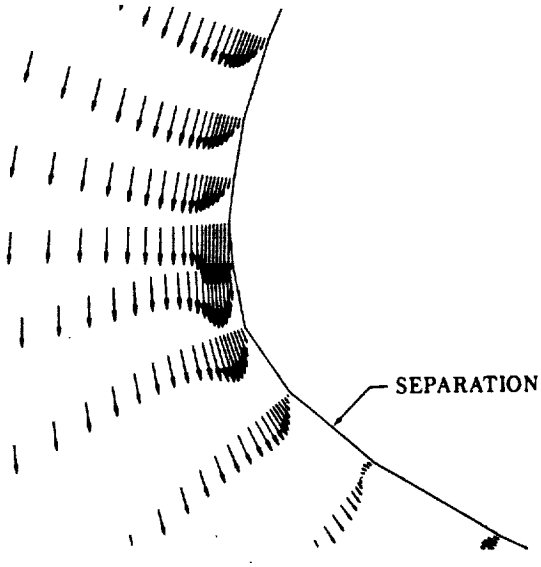

(b) With blowing, $p_p/p_\infty = 1.04$.

Figure 45: Close-up of velocity vectors near leading edge at $2y/b = 0.7$ with and without blowing

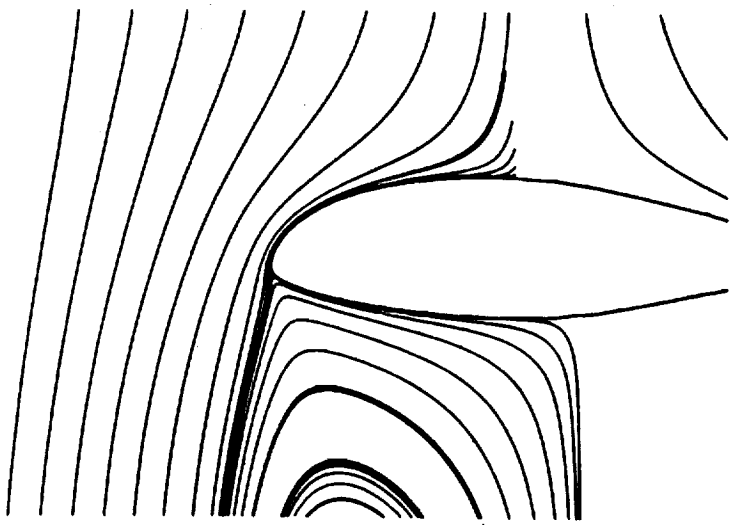

(a) With no blowing

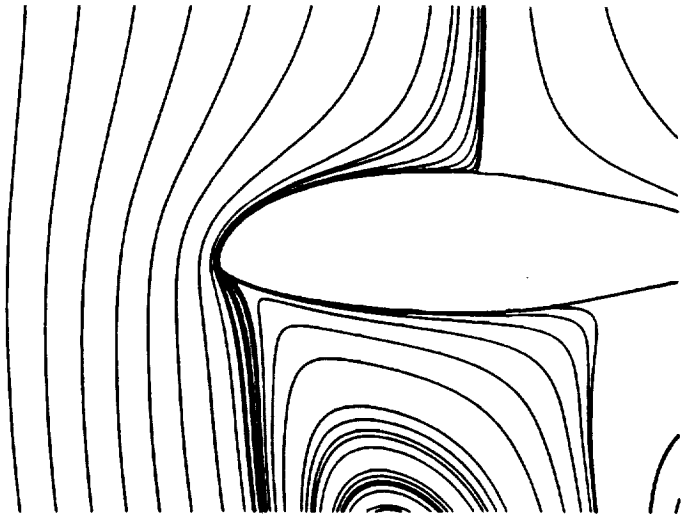

(b) With blowing, $p_p/p_\infty = 1.04$

Figure 46: Particle traces showing the wing wake at $2y/b = 0.7$, with and without blowing.

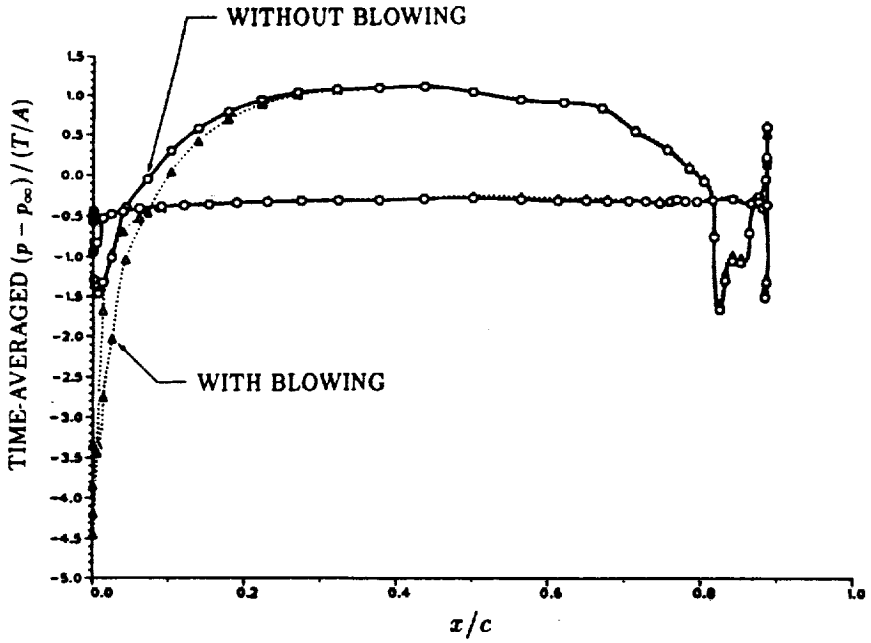

Figure 47: The computed wing surface pressures at $2y/b = 0.7$ with and without blowing.

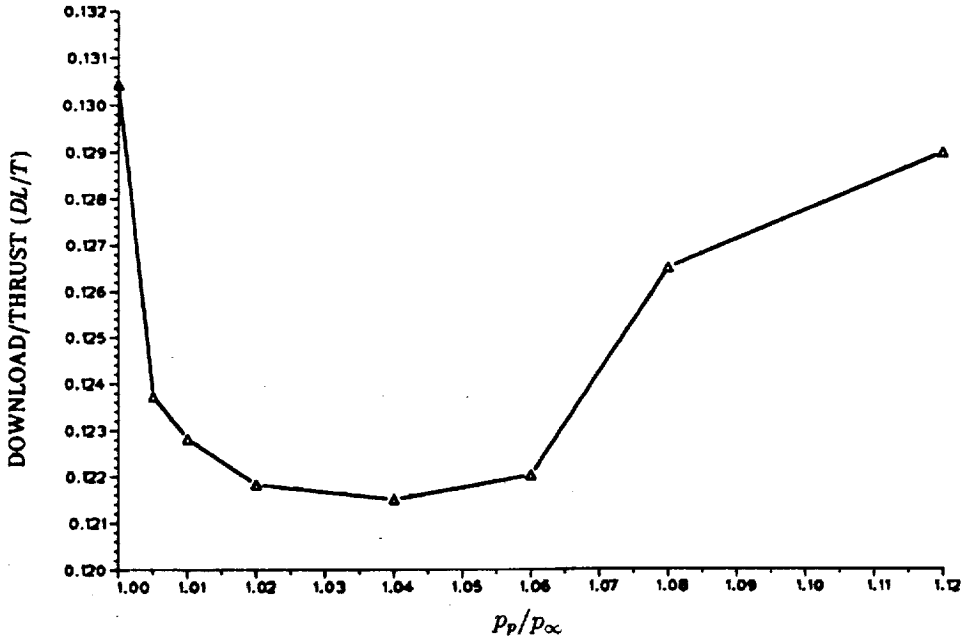

Figure 48: The variation of download/thrust with plenum blowing pressure.

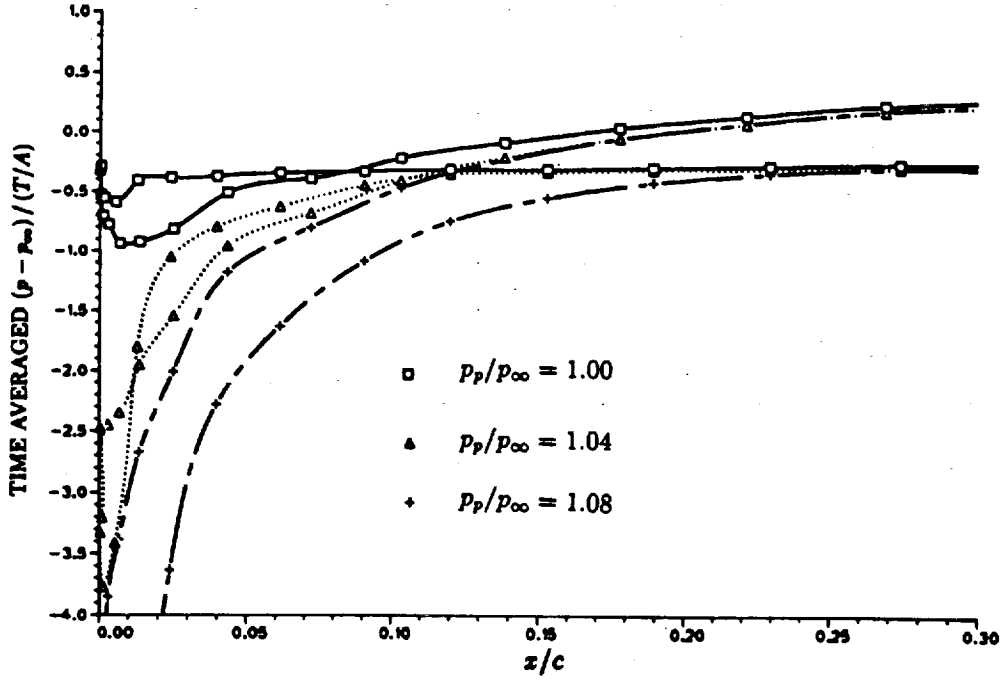

Figure 49: The wing surface pressures in the region of the leading edge of the wing at a spanwise location $2y/b = 0.15$ for different blowing pressures.

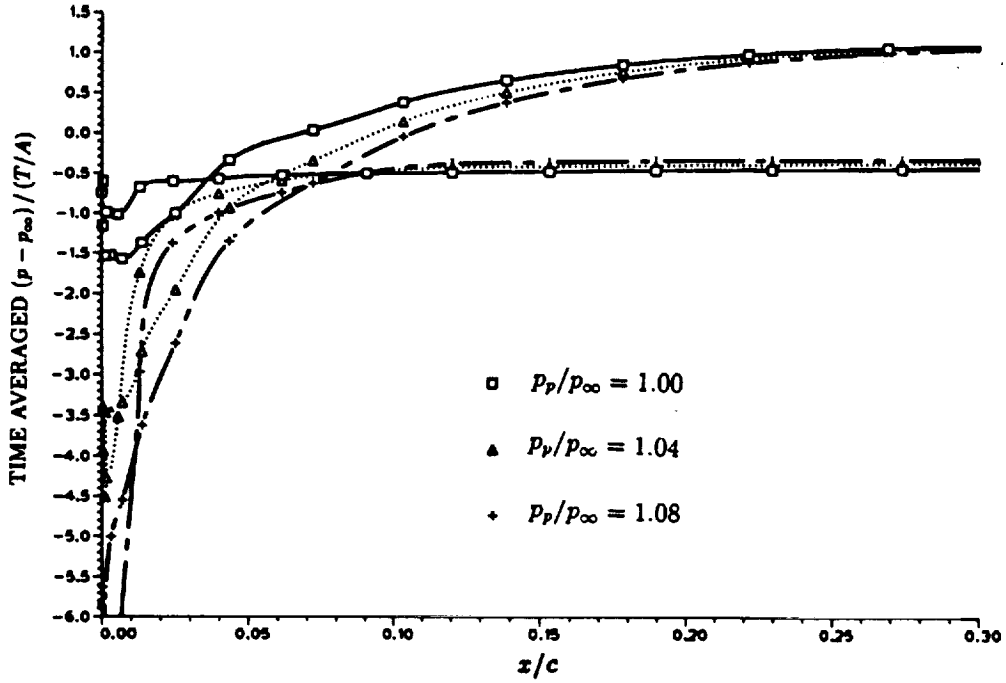

Figure 50: The wing surface pressures near the leading edge at a spanwise location of $2y/b = 0.7$ for different blowing pressures.

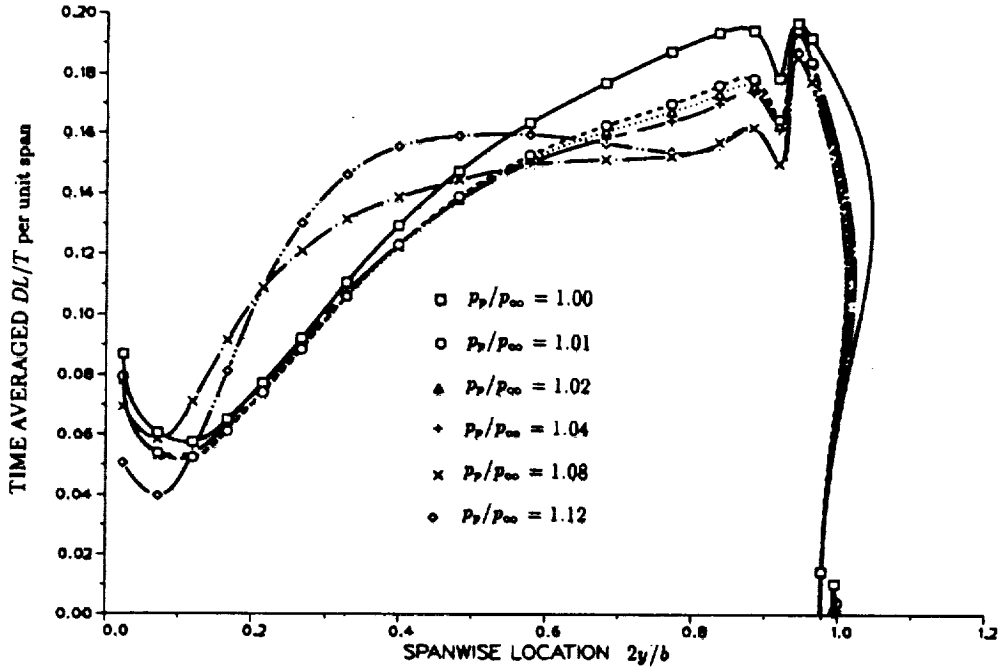

Figure 51: Local download per unit span for a range of blowing pressures.

Chapter 6

Conclusions and Recommendations

6.1 Conclusions

Computations of wing/rotor interaction about a tilt rotor configuration in hover have been successfully performed. The three-dimensional, unsteady, thin-layer Navier-Stokes equations are solved using a time-accurate, implicit, finite difference solution algorithm. Previous attempts at computing the complex tilt rotor flowfield involved solving either, in three-dimensions, a simpler set of equations that did not include viscous effects, or, in two-dimensions, the Navier-Stokes equations for an airfoil at right angles to the freestream. The flowfield about the tilt rotor configuration, however, being very complex, and involving highly three-dimensional flow over the tilt rotor wing with both leading and trailing edge flow separations, requires an approach such as that developed in this work for an accurate computation of all the flow features.

The method developed here is unique in that it not only computes the time-averaged rotor flowfield including the mean axial and swirl velocity components in the rotor slipstream, but does so in the presence of a bluff body, i.e. the wing. The rotor flow and the flow about the wing are closely-coupled, the rotor disk being only about one wing chord above the wing. Both the effect of the rotor flowfield on the wing and the effect of the wing on the rotor flow are computed with the current

numerical model. This is accomplished by modeling the rotor as an actuator disk and incorporating momentum theory/blade element analysis into the Navier-Stokes solution method. Solution blanking at interior points of the mesh has been shown here to be an effective technique in introducing the effects of the rotor and tangential leading edge jet. In this way, only a single-zone grid is required to represent the wing, rotor disk, and tangential wall jet.

The computational method developed in this work is useful in gaining a more detailed understanding of the complex tilt rotor flowfield in hover. The principal observations from the numerical results are outlined below:

- The three-dimensionality of the flow around the wing is highlighted by the transitioning of primarily chordwise flow on the wing upper surface to primarily spanwise flow further inboard.

- The vertical extent of the fountain flow at the plane of symmetry is less than observed in flow visualization during experimental tests, indicating that, within the limitations of the present analysis, the effect of the fountain is less important than previously thought.

- The spanwise variation in the flowfield is also clearly evidenced in the computed variation of download along the wing. The download is greater on that portion of the wing immersed in the rotor flowfield, as expected, but also it is increased locally in the region of the recirculation fountain.

- The flow separates from the wing leading and trailing edges, creating a large region of separated flow beneath the wing. The computation indicates that the resulting flow unsteadiness is very small. This observation is supported by experimental results which indicate that the measured unsteadiness is due primarily to the unsteady rotor wake caused by rotor blade passage, which is not modeled in the current numerical approach.

- Flow separation forward of the trailing edge on the flap upper surface is predicted for that region of the wing where the flow is generally chordwise. This

emphasizes the need to optimize flap angle and flap surface profile in order to minimize early flow separation which increases the wing download.

- The computation predicts the formation of a standing vortex beneath the wing tip. This has not as yet been observed experimentally.

- The azimuthal variation of flow properties in the rotor disk, due to the blockage effect of the wing, is of sufficient magnitude that it should be accounted for in stability and control and vibration analyses of the tilt rotor.

- The benefits of a numerical model are highlighted in the study of the effects of rotor-induced swirl. By being able to turn it off and on, computationally, which can not be done experimentally, swirl is seen to be beneficial, by reducing download.

- Leading edge tangential blowing is effective in reducing the download. Assuming that the payload is 25% of the total rotor thrust, the 7% computed reduction in download due to blowing would yield a not insignificant increase in payload carrying capability of about 3 - 4%, depending on the actual magnitude of download/thrust. Optimum blowing would involve a spanwise variation of plenum pressure, with more blowing required on that portion of the wing immersed in the rotor flowfield, and also in the fountain region. Greater reductions in download could probably be obtained by tailoring the shape of the wing leading edge to be a better Coanda surface. An optimization of the location of the jet would also be a useful exercise.

Comparisons have been made between computational results and experimental measurements, but with some caution. The numerical model of the tilt rotor differs somewhat from the experimental models. For example, the nacelle, rotor hub, and model support structures are not represented in the computation. Wing sweep and dihedral, which probably tend to reduce the download, are also not taken into account. The predicted wing download is 20%–30% higher than the measured values at a rotor thrust coefficient of 0.0164. In summary, the discrepancies with experiment are mainly due to the following:

- Differences between the numerical and experimental model configurations.
- Insufficient grid point density and less-than-optimum grid point distributions that contribute to numerical dissipation and local inaccuracies in resolution of the flow.
- Limitations inherent in the thin-layer Navier-Stokes equations.
- Limitations of the turbulence models.

Despite the limitations listed above, the numerical model developed in this work has proven to be a useful tool in studying the tilt rotor flowfield and download reduction due to leading edge tangential blowing. It can also be used to examine such things as the effect of flap deflection, direction of rotor rotation, and rotor thrust coefficient on download.

6.2 Recommendations

When the experimental results become available, from on-going tests at NASA Ames of a tilt rotor configuration which is near-identical to the computational model, comparison with the current numerical results would be very useful. This would provide a more accurate basis of comparison by eliminating discrepancies due to geometric differences.

Further improvements in the accuracy of the computation could be obtained by increasing the grid point density in the regions of the rotor and rotor wake, particularly, near the edge of the rotor slipstream. The grid density could also be increased around and beneath the wing to better resolve the complex flow in the wing wake. Further grid sensitivity studies are required to determine more completely the effect of the grid on the solution.

Because the local download distribution along the wing is sensitive to the local induced velocity distribution beneath the rotor, to improve the accuracy of the total download prediction, the rotor induced velocity must be more accurately computed. The current grid is Cartesian-like in and below the rotor plane and, therefore, it is

not capable of accurately resolving the edge of the rotor slipstream for all azimuthal locations. It is suggested that this be achieved by exploiting the current method's "blanking" capability and expanding it to a full "chimera" implementation. This would permit the embedding of a cylindrical grid into a global grid around the wing. The cylindrical grid would provide a more appropriate distribution of points for the resolution of the cylindrically-shaped rotor slipstream. The solutions of each mesh would be performed consecutively and boundary conditions updated by interpolation between grids.

The rotor's effect on the flowfield is unsteady and caused by the passage of each blade. In the case of the 3-bladed V-22 rotor, for example, any given point on the rotor disk sees a 3-per-rev forcing frequency. In the current study, the unsteady effects of the rotor blades are time-averaged onto elemental areas of the rotor disk. Given sufficient number of grid points in the rotor plane, however, the effective position of the blades could be resolved and the local, time-dependent contribution of the blades could be modeled. In this way the effects on wing download, of unsteadiness imparted by the rotor into the slipstream, could be studied.

An experimental test of a model wing at right angles to a freestream flow would help gain a better understanding of the complicated flow region beneath the wing, in the absence of the cyclic pulsing imparted to the flowfield by the rotor. This would allow measurement of the unsteadiness in the wing wake and its consequent effect on the magnitude and frequency of download oscillations. In order to either validate the current computation or provide guidance for further improvements to the numerical model, it would be useful to know whether the actual wing wake is comprised of a vortex street or a pair of counter-rotating vortices (as computed), or whether it is more random and chaotic (and, therefore, much more difficult to model numerically).

A greater degree of accuracy in the modeling of the separated flow region would be attained if the full Navier-Stokes equations are solved. Also, an improved turbulence model developed specifically for bluff body flows would improve the results even further. A computation which is second-order accurate in time might also be attempted to better resolve the unsteadiness in the wake.

Eventually, at some point in the future when computational resources become

available, it would be desirable to perform a time-accurate Navier-Stokes calculation about each of the rotating blades of the rotor and to couple that with the solution of the rest of the tilt rotor flowfield. Modeling the rotor hub, engine pylon, the fuselage and tail are obvious improvements that would help yield a more accurate representation of the actual tilt rotor aircraft. This, of course, would entail complex grid generation.

Implementation of all the above recommendations is a challenging task, but one that would be of great value in the pursuit of the complete understanding of the complicated tilt rotor flowfield.

Bibliography

[1] Rosenstein, H. and Clark, R., "Aerodynamic Development of the V-22 Tilt Rotor", AIAA Paper 86-2678, AIAA/AHS/ASEE Aircraft Systems, Design & Technology Meeting, Dayton, Ohio, 1986.

[2] Felker, F. F. and Light, J., "Rotor/Wing Aerodynamic Interactions in Hover", NASA TM 88255, 1986.

[3] McVeigh, M. A., "The V-22 Tilt-Rotor Large-Scale Rotor Performance/Wing Download Test and Comparison with Theory", Vertica, Vol. 10, No. 3/4, 1986.

[4] Maisel, M. and Harris, D., "Hover Tests of the XV-15 Tilt Rotor Research Aircraft", AIAA Paper 81-2501, AIAA/SETP/SFTE/SAE/ITEA/IEEE 1st Flight Test Conf., Las Vegas, 1981.

[5] McCroskey, W., Spalart, P., Laub, G., Maisel, M., and Maskew, B., "Airloads on Bluff Bodies, with Application to the Rotor-Induced Downloads on Tilt-Rotor Aircraft", Vertica, Vol.9, No.1, 1985.

[6] Felker, F. F., "A Review of Tilt/Rotor Download Research", Paper No. 14, 14th European Rotorcraft Forum, Milano, Italy, 1988.

[7] Maisel, M., Laub, G., and McCroskey, W., "Aerodynamic Characteristics of Two-Dimensional Wing Configurations at Angles of Attack Near $-90°$", NASA TM 88373, 1986.

[8] McVeigh, M., Grauer, W., and Paisley, D., "Rotor/Airframe Interactions on Tiltrotor Aircraft", Proceedings of the 44th Annual Forum of the American Helicopter Society, Washington, D.C., June 1988.

[9] Felker, F., Signor, D., Young, L., and Betzina, M., "Performance and Loads Data From a Hover Test of a 0.658-Scale V-22 Rotor and Wing", NASA TM 89419, April 1987.

[10] Felker, F., Shinoda, P., Heffernan, R., and Sheehy, H., "Wing Force and Surface Pressure Data from a Hover Test of a 0.658-Scale V-22 Rotor and Wing", NASA TM 102244, Feb. 1990.

[11] Felker, F., "Results from a Test of a 2/3-Scale V-22 Rotor and Wing in the 40- by 80-Foot Wind Tunnel", presented at the 47th Annual Forum of the American Helicopter Society, Phoenix, Arizona, May 1991.

[12] Clark, D. and McVeigh, M., "Analysis of the Wake Dynamics of a Typical Tilt-Rotor Configuration in Transition Flight", Paper No. 28, 11th European Rotorcraft Forum, London, England, 1985.

[13] Clark, D., "Analysis of the Wing/Rotor and Rotor/Rotor Interactions Present in Tilt-Rotor Aircraft", Vertica, Vol.11, No.4, 1987.

[14] Lee, C. S., "Panel Method Calculation of Tilt Rotor Download", Paper 39-1, presented at the International Specialists' Meeting on Rotorcraft Basic Research, Atlanta, Georgia, March 1991.

[15] Lee, C. S., "A Two Dimensional Study of Rotor/Airfoil Interaction in Hover", JIAA TR-88, Stanford University, 1988.

[16] Raghavan, V., McCroskey, W. J., Van Dalsam, W. R., and Baeder, J. D., "Calculations of the Flow Past Bluff Bodies, Including Tilt-Rotor Wing Sections at $\alpha = -90°$", AIAA Paper 90-0032, AIAA 28th Aerospace Sciences Meeting, Reno, 1990.

[17] Stremel, P. M., "Calculation of Flow about Two-Dimensional Bodies by Means of the Velocity-Vorticity Formulation on a Staggered Grid", AIAA Paper 91-0600, AIAA 29th Aerospace Sciences Meeting, Reno, 1991.

[18] Johnson, W., Helicopter Theory, Princeton University Press, Princeton, New Jersey, 1980.

[19] Stremel, P. M., "A Method for Modeling Finite Core Vortices in Wake Flow Calculations", AIAA Paper 84-0417, AIAA 22nd Aerospace Sciences Meeting, Reno, 1984.

[20] Stremel, P. M., "The Calculation of Rotor/Fuselage Interaction for Two-Dimensional Bodies", 16th European Rotorcraft Forum, Paper II.11.3, Glasgow, Sept. 18-21, 1990.

[21] Srinivasan, G. and McCroskey, W., "Numerical Simulations of Unsteady Airfoil-Vortex Interactions", Vertica, Vol.11, No.1/2, 1987.

[22] Agarwal, R. K. and Deese, J. E., "Euler Calculations for Flowfield of a Helicopter Rotor in Hover", J. Aircraft, Vol. 24, No. 4, April 1987.

[23] Roberts, T. W., "Euler Equation Computations for the Flow Over a Hovering Helicopter Rotor", NASA CR 177493, 1988.

[24] Srinivasan, G. and McCroskey, W., "Navier-Stokes Calculations of Hovering Rotor Flowfields", AIAA Paper 87-2629-CP, AIAA Atmospheric Flight Mechanics Conf., Monterey, California, 1987.

[25] Srinivasan, G. R., Baeder, J. D., Obayashi, S., McCroskey, W. J., "Flowfield of a Lifting Hovering Rotor — A Navier-Stokes Simulation", Paper No. I.3.5, 16th European Rotorcraft Forum, Glasgow, Scotland, Sept. 1990.

[26] Rajagopalan, R. G. and Mathur, S. R., "Three Dimensional Analysis of a Rotor in Forward Flight", AIAA Paper 89-1815, AIAA 20th Fluid Dynamics, Plasma Dynamics and Lasers Conf., Buffalo, 1989.

[27] McCroskey, W. and Baeder, J., "Some Recent Advances in Computational Aerodynamics for Helicopter Applications", NASA TM 86777, 1985.

[28] Obayashi, S. and Kuwahara, K., "An Approximate LU Factorization Method for the Compressible Navier-Stokes Equations", Journal of Computational Physics, Vol.63, 1986.

[29] Fujii, K. and Obayashi, S., "Practical Applications of New LU-ADI Scheme for the Three-Dimensional Navier-Stokes Computation of Transonic Viscous Flows", AIAA Paper 86-0513, AIAA 24th Aerospace Sciences Meeting, Reno, 1986.

[30] Fujii, K. and Obayashi, S., "Navier-Stokes Simulation of Transonic Flow over Wing-Fuselage Combinations", AIAA Paper 86-1831, AIAA 4th Applied Aerodynamics Conf., San Diego, 1986.

[31] Yeh, D., Tavella, D., Roberts, L., and Fujii, K., "Navier-Stokes Computation of the Flow Field over Delta Wings with Spanwise Leading Edge Blowing", AIAA Paper 88-2558-CP, AIAA 6th Applied Aerodynamics Conference, Williamsburg, Virginia, June 1988.

[32] Yeh, D., Tavella, D., Roberts, L., and Fujii, K., "Numerical Study of the Effects of Tangential Leading Edge Blowing on Delta Wing Vortical Flow", AIAA Paper 89-0341, AIAA 25th Aerospace Sciences Meeting, Reno, 1989.

[33] Yeh, D., "Numerical Study of Delta Wing Leading Edge Blowing", JIAA TR-86, Stanford University, 1988.

[34] Benek, J. A., Buning, P. G., and Steger, J. L., "A 3-D Chimera Grid Embedding Technique", AIAA Paper 85-1523, 1985.

[35] Liepmann, H. W. and Roshko, A., Elements of Gasdynamics, John Wiley & Sons, Inc., New York, 1957.

[36] Viviand, H., "Formes Conservatives des Équations de la Dynamique des Gaz", LaRecherche Aérospatiale, No.1, 1974.

[37] Vinokur, M., "Conservation Equations of Gasdynamics in Curvilinear Coordinate Systems", Journal of Computational Physics, No.14, 1974.

[38] Anderson, D. A., Tannehill, J. C., and Pletcher, R. H., Computational Fluid Mechanics and Heat Transfer, Hemisphere Publishing Corp., New York, 1984.

[39] Baldwin, B. and Lomax, H., "Thin Layer Approximation and Algebraic Model for Separated Turbulent Flows", AIAA Paper 78-257, AIAA 16th Aerospace Sciences Meeting, Huntsville, Alabama, 1978.

[40] Roberts, L., "A Theory for Turbulent Curved Wall Jets", AIAA Paper 87-0004, AIAA 25th Aerospace Sciences Meeting, Reno, 1987.

[41] Shrewsbury, G., "Numerical Evaluation of Circulation Control Airfoil Performance Using Navier-Stokes Methods", AIAA Paper 86-0286, AIAA 24th Aerospace Sciences Meeting, Reno, 1986.

[42] Beam, R. M. and Warming, R. F., "An Implicit Finite-Difference Algorithm for Hyperbolic Systems in Conservation-Law Form", Journal of Computational Physics, Vol.22, 1976.

[43] Pulliam, T. and Steger, J., "Implicit Finite-Difference Simulations of Three-Dimensional Compressible Flow", AIAA Journal, Vol.18, No.2, 1980.

[44] Meakin, R. and Suhs, N., "Unsteady Aerodynamic Simulation of Multiple Bodies in Relative Motion", AIAA Paper 89-1996-CP, AIAA 9th CFD Conf., Buffalo, June 1989.

[45] Kuan, J.-H. and Dougherty, F. C., "Time Accurate Study for Multiple Moving Grids", AIAA Paper 89-1997-CP, AIAA 9th CFD Conf., Buffalo, June 1989.

[46] Pulliam, T. and Chaussee, D., "A Diagonal Form of an Implicit Approximate-Factorization Algorithm", Journal of Computational Physics, Vol.39, 1981.

[47] Pulliam, T., "Euler and Thin Layer Navier-Stokes Codes: ARC2D, ARC3D", Notes for Computational Fluid Dynamics User's Workshop, The University of Tennessee Space Institute, Tullahoma, Tennessee, March 12-16, 1984.

[48] Guruswamy, G. P., "Time-Accurate Unsteady Aerodynamic and Aeroelastic Calculations of Wings Using Euler Equations", AIAA Paper 88-2281, AIAA/ASME/ASCE/AHS 29th Structures, Structural Dynamics and Materials Conf., Williamsburg, Virginia, 1988.

[49] Guruswamy, G. P., "Numerical Simulation of Vortical Flows on Flexible Wings", AIAA Paper 89-0537, AIAA 27th Aerospace Sciences Meeting, Reno, 1989.

[50] Steger, J. and Warming, R., "Flux Vector Splitting of the Inviscid Gasdynamic Equations with Application to Finite-Difference Methods", Journal of Computational Physics, Vol.40, 1981.

[51] Lombard, C., Bardina, J., Venkatapathy, E., and Oliger, J., "Multi-Dimensional Formulation of CSCM - An Upwind Flux Difference Eigenvector Split Method for the Compressible Navier-Stokes Equations", AIAA Paper 83-1895, AIAA 6th CFD Conf., Danvers, Massachusetts, 1983.

[52] Pulliam, T. and Steger, J., "Recent Improvements in Efficiency, Accuracy, and Convergence for Implicit Approximate Factorization Algorithms", AIAA Paper 85-0360, AIAA 23rd Aerospace Sciences Meeting, Reno, 1985.

[53] Obayashi, S. and Guruswamy, G. P., "Unsteady Shock-Vortex Interaction on a Flexible Delta Wing", Paper AIAA 91-1109, 32nd AIAA/ASME/ASCE/AHS/-ASC Structures, Structural Dynamics and Materials Conf., Baltimore, April 1991.

[54] Obayashi, S., Fujii, K., and Gavali, S., "Navier-Stokes Simulation of Wind-Tunnel Flow Using LU-ADI Factorization Algorithm", NASA TM 100042, Feb. 1988.

[55] Obayashi, S., "Numerical Simulation of Underexpanded Plumes Using Upwind Algorithms", AIAA Paper 88-4360-CP, AIAA Atmospheric Flight Mechanics Conf., Minneapolis, 1988.

[56] Steger, J., "Implicit Finite Difference Simulation of Flow About Arbitrary Geometries with Application to Airfoils", AIAA Paper 77-665, AIAA 10th Fluid & Plasmadynamics Conf., Albuquerque, New Mexico, 1977.

[57] Sorenson, R. and Steger, J., "Numerical Generation of Two-Dimensional Grids by the Use of Poisson Equations with Grid Control at the Boundaries", Proc. of the Numerical Grid Generation Techniques Workshop, Langley Research Center, NASA, Hampton, Va., NASA CP-2166, 1980.

[58] Thompson, J., Thames, F., and Mastin, C., "Automatic Numerical Generation of Body-Fitted Curvilinear Coordinate System for Field Containing Any Number of Arbitrary Two-Dimensional Bodies", Journal of Computational Physics, Vol.15, 1974.

[59] Thompson, J., Thames, F., Mastin, C., and Shanks, S., "Use of Numerically Generated Body-Fitted Coordinate Systems for Solutions of the Navier-Stokes Equations", AIAA 2nd CFD Conf., Connecticut, 1975.

[60] Holst, T. L., "Numerical Computation of Transonic Flow Governed by the Full-Potential Equation", NASA TM 84310, 1983.

[61] Sorenson, R., "A Computer Program to Generate Two-Dimensional Grids About Airfoils and Other Shapes by the Use of Poisson's Equation", NASA TM 81198, May 1980.

[62] Chaussee, D., Kutler, P., and Pulliam, T. , "Three Dimensional Viscous Flow Field Program. Part 1. Viscous Blunt Body Program (Interim Report)", AFWAL-TM-81-63-FIMG, Flight Dynamics Laboratory, Air Force Wright Aeronautical Laboratories, Wright-Patterson Air Force Base, Ohio, 1981.

[63] Glauert, H., The Elements of Airfoil and Airscrew Theory, Cambridge University Press, London, 1930.

[64] McCormick, B. W., Aerodynamics of V/STOL Flight, Academic Press, New York, 1967.

[65] Prouty, R. W., Helicopter Performance, Stability, and Control, PWS Publishers, Boston, 1986.

[66] Yu, N. J., Samant, S. S., and Rubbert, P. E., "Flow Prediction for Propfan Configurations Using Euler Equations", AIAA Paper 84-1645, AIAA 17th Fluid Dynamics, Plasma Dynamics and Lasers Conf., Colorado, 1984.

[67] Oates, G. C., Aerothermodynamics of Gas Turbine and Rocket Propulsion, American Institute of Aeronautics and Astronautics, Inc., New York, 1984.

[68] Stepniewski, W. Z., "Rotary-Wing Aerodynamics. Volume 1 — Basic Theories of Rotor Aerodynamics (With Application to Helicopters)", NASA CR-3082, January 1979.

[69] Press, W., Flannery, B., Teukolsky, S., and Vetterling, W., Numerical Recipes The Art of Scientific Computing, Cambridge University Press, New York, 1987.

[70] Tavella, D., Schiff, L., and Cummings, R., "Pneumatic Vortical Flow Control at High Angles of Attack", AIAA Paper 90-0098, 28th Aerospace Sciences Meeting, Reno, 1990.

[71] Buning, P. and Steger, J., "Graphics and Flow Visualization in Computational Fluid Dynamics", AIAA Paper 85- 1507, AIAA 7th CFD Conf., Cincinnati, 1985.

[72] Walatka, P. and Buning, P., "PLOT3D User's Manual", NASA TM 101067, 1989.

[73] Fejtek, I. and Roberts, L., "A CFD Study of Tilt Rotor Flowfields", JIAA TR-96, Stanford University, 1989.

REPORT DOCUMENTATION PAGE

Form Approved
OMB No. 0704-0188

1. AGENCY USE ONLY *(Leave blank)*	2. REPORT DATE	3. REPORT TYPE AND DATES COVERED
	July 1993	Contractor Report

4. TITLE AND SUBTITLE

Navier–Stokes Flowfield Computation of Wing/Rotor Interaction for a Tilt Rotor Aircraft in Hover

5. FUNDING NUMBERS

NCC2-55

6. AUTHOR(S)

Ian G. Fejtek

7. PERFORMING ORGANIZATION NAME(S) AND ADDRESS(ES)

Stanford University
Department of Aeronautics and Astronautics
Stanford, CA 94305

8. PERFORMING ORGANIZATION REPORT NUMBER

A-93096

9. SPONSORING/MONITORING AGENCY NAME(S) AND ADDRESS(ES)

National Aeronautics and Space Administration
Washington, DC 20546-0001

10. SPONSORING/MONITORING AGENCY REPORT NUMBER

NASA CR-4532

11. SUPPLEMENTARY NOTES

Point of Contact: Jeffrey Light, Ames Research Center, MSTO42, Moffett Field, CA 94035-1000; (415) 604-4881

12a. DISTRIBUTION/AVAILABILITY STATEMENT

Unclassified – Unlimited
Subject Category 02

12b. DISTRIBUTION CODE

13. ABSTRACT ***(Maximum 200 words)***

The download on the wing produced by the rotor-induced downwash of a tilt rotor aircraft in hover is of major concern because of its severe impact on payload-carrying capability. A method has been developed to help gain a better understanding of the fundamental fluid dynamics that causes this download, and to help find ways to reduce it. In particular, the method is employed in this work to analyze the effect of a tangential leading edge circulation-control jet on download reduction. Because of the complexities associated with modeling the complete configuration, this work focuses specifically on the wing/rotor interaction of a tilt rotor aircraft in hover. The three-dimensional, unsteady, thin-layer compressible Navier–Stokes equations are solved using a time-accurate, implicit, finite difference scheme that employs LU-ADI factorization. The rotor is modeled as an actuator disk which imparts both a radical and an azimuthal distribution of pressure rise and swirl to the flowfield. A momentum theory/blade element analysis of the rotor is incorporated into the Navier–Stokes solution method. Solution blanking at interior points of the mesh has been shown here to be an effective technique in introducing the effects of the rotor and tangential leading edge jet. Results are presented both for a rotor alone and for wing/rotor interaction. The overall mean characteristics of the rotor flowfield are computed including the flow acceleration through the rotor disk, the axial and swirl velocities in the rotor downwash, and the slipstream contraction. Many of the complex tilt rotor flow features are captured including the highly three-dimensional flow over the wing, the recirculation fountain at the plane of symmetry, wing leading and trailing edge separation, and the large region of separated flow beneath the wing. Mean wing surface pressures compare fairly well with available experimental data, but the time-averaged download/thrust ratio is 20–30% higher than the measured value. The discrepancy is due to a combination of factors that are discussed. Leading edge tangential blowing, of constant strength along the wing span, is shown to be effective in reducing download. The jet serves primarily to reduce the pressure on the wing upper surface. The computation clearly shows that, because of the three-dimensionality of the flowfield, optimum blowing would involve a spanwise variation in blowing strength.

14. SUBJECT TERMS	15. NUMBER OF PAGES
Tilt rotor download, Computational fluid dynamics, Rotor/Wi2m interaction	156
	16. PRICE CODE A08

17. SECURITY CLASSIFICATION OF REPORT	18. SECURITY CLASSIFICATION OF THIS PAGE	19. SECURITY CLASSIFICATION OF ABSTRACT	20. LIMITATION OF ABSTRACT
Unclassified	Unclassified		

National Aeronautics and
Space Administration

Ames Research Center
Moffett Field, California 94035-1000